Université de Liège
Applied Sciences Faculty

Thermal design of OUFTI-1

Thesis submitted in partial fulfilment of the requirements
for the degree of Master in Aerospace Engineering by:

Lamberto Dell'Elce

Advisor: Prof. Pierre Rochus

Academic Year 2010/2011

Acknowledgments

I am grateful to all the people that helped and supported me during the realisation of this work.

At first, I thank Professor Pierre Rochus for its precious advice, and for always having some time to spend for me, whenever I asked him.

I wish to thank Professor Gaetan Kerschen that, together with Professor Rochus, gave me the opportunity to participate to this project.

I am also extremely indebted with my predecessors, Lionel Jacques and Jean-Philippe Nöel, and with Lucas Salvador, for their invaluable advices and and technical support throughout the whole year.

I have to express my gratitude to the OUFTI-1 team, with which I liked to work. Especially, I am grateful to Amandine Denis and Jerome Wertz for their supervision and for creating a strong team spirit.

I thank the Politecnico di Milano for giving me the opportunity to partecipate to the TIME project, and the Université de Liège, which welcomed me, and made me know talented Belgian engineers and students.

A special thanks goes to my family, especially my mother and my brother Luca, for their moral and economical support throughout these two years abroad.

Last, but not least, I thank you, Jessica, for being always close to me, despite the distance.

Contents

List of Figures

List of Tables

Abbreviations and acronyms

ADCS	Attitude Determination and Control System
BAT	Battery Subsystem
BOL	Begin of Life
COM	Telecommunication System
COTS	Commercial Off The Self
CVCM	Collected Volatile Condensable Material
CSL	Centre Spatial de Liège
DAR	Deviation Wavier Approval Request
ECSS	European Cooperation for Space Standardization
EOL	End of Life
EPS	Electrical Power System
FE	Finite Elements
FM	Flight Model
GL	Linear Conductance
GUI	Graphical User Interface
GR	Radiative Conductor
GMM	Geometrical Mathematical Model
LV	Launch Vehicle
LiPo	Lithium Polymer
MLI	Multi Layer Insulation

OBC	On-Board Computer
PCB	Printed Circuit Board
PCM	Phase Change Materials
PSA	Pressure-sensitive adhesive
QI	Internal Source of Power
QM	Qualification Model
QS	Solar power
QA	Albedo Power
TCS	Thermal Control System
TES	Thermal Energy Storage
TML	Total Mass Loss
TMM	Thermal Mathematical Model
xEPS	Experimental Electrical Power System

Chapter 1

Introduction

CubeSats are nanosatellites with a volume of $10 \times 10 \times 10 cm^3$ (cubic shape) and a maximum weight of $1kg$. The main target of the Cubesats is to provide a low-cost and reliable way to send payloads in orbit, in order to perform technical demonstration and to provide access to space for universities and private companies. Furthermore, the educational benefits are huge, since students have the opportunity to gain hands-on experience in real space applications.

OUFTI-1 is a CubeSat developed at the Université de Liège, and the first Belgian nanosatellite. The project began in 2007, in the context of the *LEODIUM* program (i.e., *Lancement En Orbite de Démonstations Innovantes d'une Université Multidisciplinaire*), which involves both the Université de Liège and Liège Espace, a consortium of space industries and research centers in the region of Liège.

OUFTI-1 is provided with three payloads:

D-STAR: the primary objective of the mission is to test the D-STAR in space. D-STAR is a fully digital-amateur radio protocol, which allows simultaneous data and voice transmission, and provides a network connexion method. The fully-digital implementation allows to improve the quality of the communications, and is the main innovation of the protocol.

Experimental Electrical Power System (xEPS): developed in cooperation with *Thales Alenia Space*. It is is a digitally-controlled flyback converter and based on a PIC microcontroller[1].

New generation high efficiency (30%) solar cells: developed by *AZUR Space*. OUFTI-1 has to provide their formal in-orbit validation. 10 of these cells are placed on five external faces of OUFTI-1 (the sixth one being devoted to the antenna deployment panel).

This work is devoted to the thermal analysis, design and testing of OUFTI-1.

[1] To avoid that the electrical management is based upon an experimental payload, another conventional Electrical Power System (EPS) is included in OUFTi-1. When the voltage of the batteries is high enough, xEPS is supplied and connected to the $3.3V$ power bus

Component	$T_{min}[^oC]$	$T_{max}[^oC]$	Notes
Main Structure	-40	85	
Solar Cells	-100	100	
Electronics	-40	85	
Batteries	0	40	Charge
	-20	60	Discharge

Table 1.1: Thermal requirements for OUFTI-1, according to [1].

1.1 Requirements

The Thermal Control System (TCS) of a spacecraft aims at keeping the temperature of all its components into their acceptable range, and at avoiding too important temperature gradients and transients. The small mass and volume of a Cubesat cause its thermal inertia to be necessarily low, this resulting in the most important thermal challenge for the TCS of a CubeSat, since both hot and cold extreme temperatures are expected during the mission. For this reason, numerical simulations have to provide data about the most critical scenarios the satellite will have to withstand during its lifetime. So, a hot and a cold case are defined to this purpose. In the case of OUFTI-1, the hot case is characterised by the absence of eclipse and the maximum power consumption of the components, while, on the contrary, the cold case considers the orbit with the maximum eclipse duration and minimum power consumption (see Chapter 4 for their definition).

Numerical simulations and appropriate development test have to be performed to ensure that the TCS is able to satisfy all the thermal requirements in these situations.

The specific requirements of OUFTI-1 are summarized in Table 1.1.

1.2 Time history and actual state of the thermal control system of OUFTI-1

The OUFTI-1 project began in 2007. Since then, three students were in charge of its TCS:

Stefania Galli (2007-2008) performed the mission analysis of the CubeSat. In her work [3], she forecast the employment of a fully-passive TCS, based upon an accurate choice of the coatings of the spacecraft. However, she emphasized the potential criticality of the batteries, because of their restrained operational range (Table 1.1).

Lionel Jacques (2008-2009) succeeded her, and he developed a preliminary, but detailed, thermal analysis of the CubeSat. In his work, he identified three main issues for the spacecraft [1]:

- too low temperature of the batteries, in the cold case,

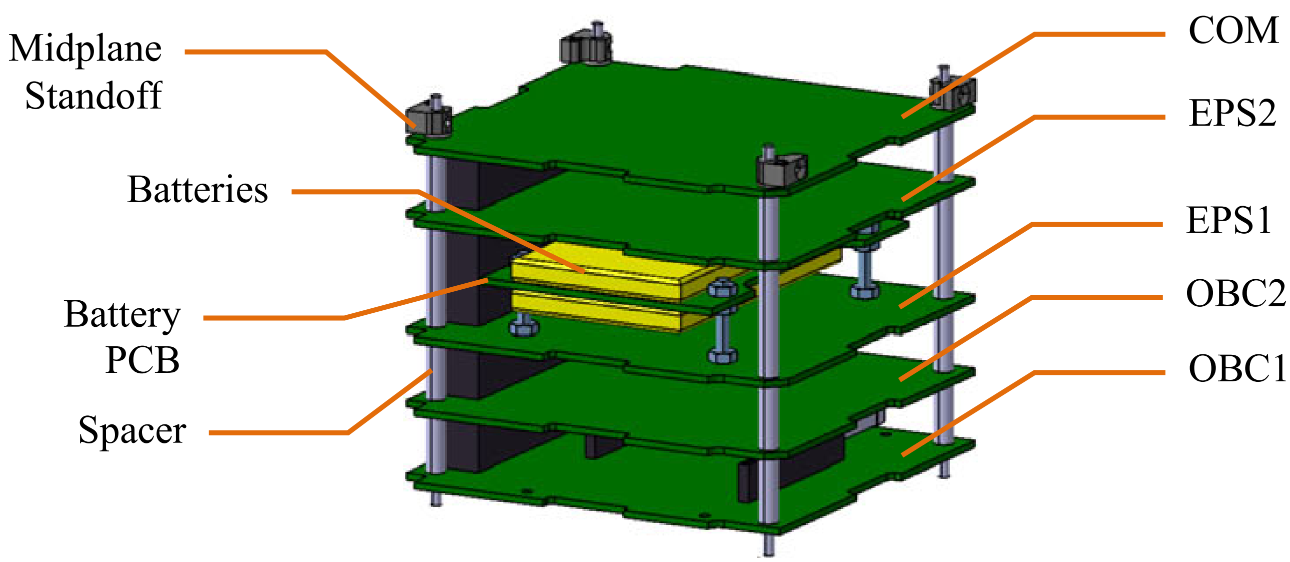

(a) Old design [1]

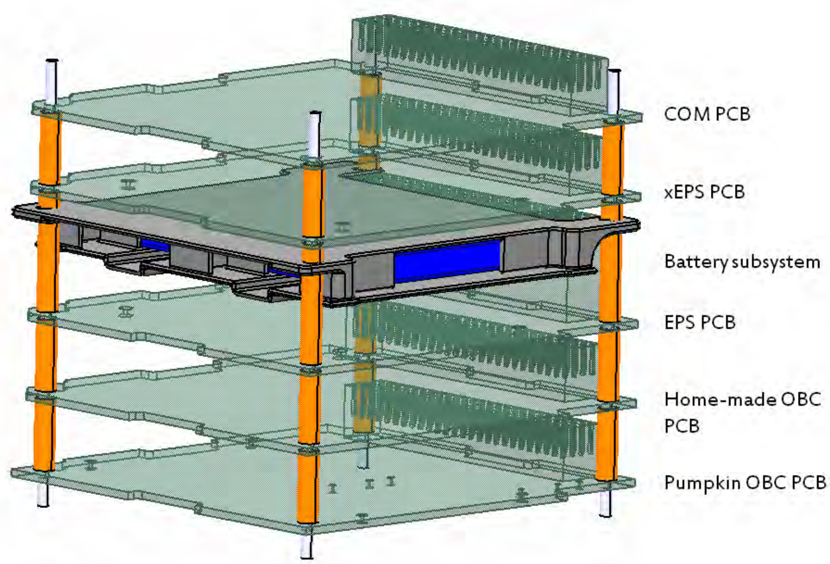

(b) New design [2]

Figure 1.1: Old and new design configuration of the BAT subsystem. In this Figure, all the main subsystems of the satellite are shown, too.

- too high temperature expected by the EPS transistor, in the hot case,
- hotspot of the Telecommunication System (COM) amplifier, in the hot case.

To solve them, he proposed the following solutions:

- the exploitation of an active TCS to heat batteries, consisting of one heater (per battery) and mechanical thermostats to control them,
- the realisation of a thermal strap to drain heat from the transistor to the antenna panel, and the shunt of part of the excessive power toward two patch resistors glued on the antenna panel as well,
- any solution was proposed for the COM amplifier because of lack of data about this component and its location. However, a parametric analysis revealed that its hotspot was minimised if the amplifier was placed on a corner of the COM Printed Circuit Board (PCB).

Jean-Philippe Nöel (2009-2010) devoted its work [2] to the batteries issue, considered the most delicate and problematic. He designed the TCS of the Battery Subsystem (BAT) and performed a vacuum-condition development test to validate the performance estimated with a numerical model. Furthermore, during this year, the support of the batteries was drastically modified. A new aluminium support was designed in order to improve the mechanical behaviour of the system, and to prevent batteries from undergoing under-vacuum deformations. In this way, batteries are no more integrated on a PCB on the EPS board (Figure 1.1(a)), but they are housed in this support, which is integrated in the satellite as all the other PCBs (Figure 1.1(b)).

1.3 Outline of the dissertation

The starting point of this work is the analysis of the results of the BAT test performed in 2010. So, in Chapter 2, after an adequate introduction about the actual state of the BAT subsystem, these results are discussed. It will emerge that the design is not able to fulfil the thermal requirements of the batteries, so that the BAT issue is still the most important thermal issue of the spacecraft. For this reason, alternative design solutions and a new test procedure are proposed.

The Chapter 3 is devoted to the transistor issue. The thermal strap is designed and its performance are estimated by means of Finite Elements (FE) simulations.

Then, in Chapter 4, the new global numerical model of the satellite is described, and its simulations are exploited to check for the in-orbit performance of the new design solutions proposed in Chapters 2 and 3, and to verify that the introduction of the new BAT support is not responsible of new thermal issues.

Finally, Chapter 5 is devoted to the description of the protoflight test procedure, necessary to the flight qualification of the CubeSat.

Chapter 2

Battery subsystem

This Chapter is devoted to the problem of the batteries, which represents the main thermal issue of OUFTI-1.

The spacecraft is provided with two Lithium Polymer (LiPo) batteries (*Kokam SLB603870H*), whose operating temperature range is [4]:

- $0 \sim 40^oC$ during charge
- $-20 \sim 60^oC$ during discharge

The numerical simulations performed in 2008-2009 [1] revealed that batteries experienced about -15^oC as minimum temperature during cold case[1]. The batteries are directly charged by the solar cells, so that, when the satellite comes out from the eclipse, the requirement about the temperature range during charge is not respected.

The effect of the charging of LiPo batteries below their freezing temperature is described in [5]:

> *"Below 5^oC, the charge current should be reduced, and no charging is permitted at freezing temperatures. [...]Many battery users are unaware that consumer-grade lithium-ion batteries cannot be charged below 0^oC (32^oF). Although the pack appears to be charging normally, plating of metallic lithium can occur on the anode during a subfreezing charge. The plating is permanent and cannot be removed with cycling. Batteries with lithium plating are known to be more vulnerable to failure if exposed to vibration or other stressful conditions."*

For this reason, this scenario has to be absolutely avoided.

The low thermal inertia causes nanosatellites to experience very large temperature range, so that the freezing of the batteries is a typical issue for them, and their thermal design has often to face up with this problem. Most of the CubeSats chose to heat the batteries by means of patch heaters (e.g, compass one [6] and SwissCube [7]), while, on the contrary, other CubeSats, like Delfi-C3 [8], avoided the employment of the batteries themselves. OUFTI-1 belongs to the former category.

[1]See Table 4.3 for the definition of the hot and cold cases.

The outline of this Chapter follows the logical path pursued during the study of the behaviour of the system: at first, the BAT subsystem of OUFTI-1 and its numerical model implemented in [2] are detailed. Then, the results of the vacuum test performed at the Centre Spatial de Liège (CSL) in 2010 are analysed and correlated with the numerical simulations. Finally, a new thermal design and test procedure of the subsystem are proposed, in order to fix the problems emerged during the test analysis. Furthermore, at the end of the Chapter, a Section is devoted to a feasibility study of an innovative TCS performed by means of Phase Change Materials (PCM).

2.1 Overview of the battery subsystem

As a consequence of the thermal issue presented in the introduction of this Chapter, L. Jacques [1] proposed in 2008-2009 the exploitation of a patch heater glued on each battery in order to heat them.

Then, the design of the TCS was performed by J.P. Nöel [2] in 2009-2010, and it consists of:

Heaters: the numerical simulations in [1] proved that a minimum total power of $0.5W$ (i.e., $P_h = 0.25W$ per heater) was enough to keep batteries in their operational range. The heaters are directly supplied by the unregulated bus (i.e., the voltage is equal to the actual one of the batteries), so that the power provided is not constant in function of time, and it depends on the discharge of the batteries. For this reason, the sizing was performed by considering a minimum voltage of $V_{min} = 2.5V$, which is below the cut-off voltage of the batteries (i.e., $V_{co} = 2.7V$ [4]). So, the maximum resistance of each heater $R_h^{(max)}$ was computed to be:

$$P_h = \frac{V_{min}^2}{R_h^{(max)}} \Rightarrow R_h^{(max)} = \frac{V_{min}^2}{P_h} = 0.25W \tag{2.1}$$

The selected heaters are two *MINCO XHK5377R26.3L12B* [9], whose characteristics are:

X: low outgassing ink (X),

HK: the material is the polyimide (HK),

5377: the shape of the patch is rectangular and the sizes are $35.6 \times 59.4mm^2$ (the sizes of the front section of the batteries being $37.5 \times 69.5mm^2$ [4]),

R26.3: the nominal resistance is $R_h = 26.6\Omega$,

L12: the length of the cable is $12in$,

B: they are provided with acrylic Pressure-sensitive adhesive (PSA) #16.

	Mechanical	**Electronic**
Autonomy	+	-
Reliability	+	-
Easy to implement	+	-
Freedom in the control	-	+
Possibility of telecommanding from ground	-	+
Final Choice	+	-

Table 2.1: Choice of the kind of control for the heaters.

Though the nominal resistance R_h is grater than the maximum forecast value R_h^{max}, these heaters are able to provide the required power even if they are supplied by the cut-off voltage:

$$\frac{V_{co}^2}{R_h} \simeq 0.27W > P_h \tag{2.2}$$

so that the resistance excess is not critical[2].

Thermostats: mechanical thermostats are exploited to control the heaters. Electronic control by means of the On-Board Computer (OBC) was also envisaged as solution, since it allows to have more freedom in the management of the power (e.g., the choice to reheat might be taken in function of the charge level of the batteries), and it allows ground commanding. However, this solution was dismissed in favour of the former, since mechanical control is based upon an autonomous loop, completely independent by the OBC and by any of its hypothetical failure. Furthermore, as already stated in the introduction of this Chapter, the freezing of a battery is extremely penalising both for the battery and for the mission, so that heaters have to be supplied also when batteries are almost discharged. The pros and cons of these two kind of control are summarized in Table 2.1.

Under the electrical point of view, mechanical thermostats are a switch ruled by the temperature of the thermostat itself. Below the *set point* temperature, thermostats behave as an open circuit, while above the *operating temperature* they become a short circuit. Generally, the set point and the operating temperature do not match, so that the system is characterized by hysteresis, and the circuit is not repetitively opened and closed when the temperature is close to the set point.

Concerning the electrical arrangement of the thermostats, the three solutions shown in Figure 2.1 were envisaged, in order to provide redundancy to the system. The solution of Figure 2.1(c) is the only one able to grant a *single-fault tolerance* (i.e., the system works properly if one thermostat fails to open or close), but it is also the most expensive (4 thermostats per battery are needed), and thus it was dismissed. On the other hand, the parallel arrangement (Figure 2.1(b)) is only able to survive to a *fail*

[2]The voltage of the unregulated bus should not drop below V_{co} during the mission, because of the protection circuit (described later in this Section).

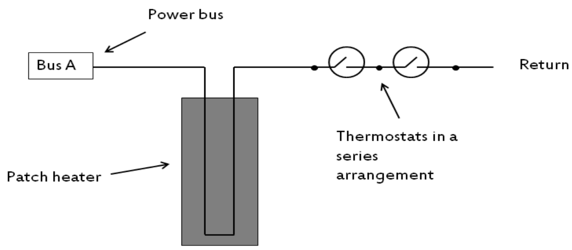

(a) Series

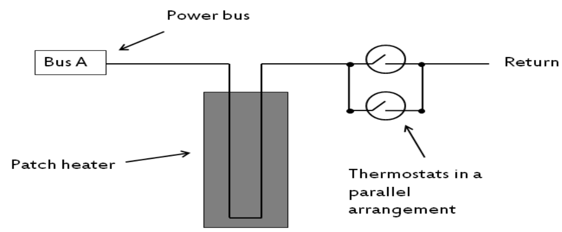

(b) Parallel

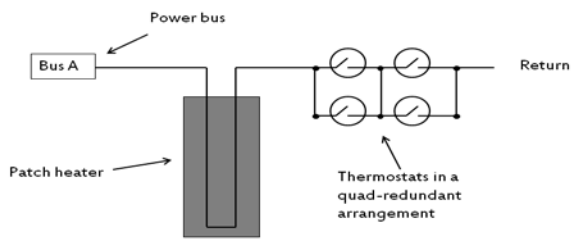

(c) Quad

Figure 2.1: Possible arrangements of the thermostats [2].

open event (i.e., one of the thermostats fails to close the circuit), but a *fail closed* event would result in a detrimental energy waste and in a continuous discharge of the batteries[3]. For these reasons, the final choice consists in the connection in series of two thermostats per heater (Figure 2.1(a)); in this way the system is able to survive to a closed fail event, but it is not able to face up an open fail; nonetheless, the power of a single heater was designed to be enough to heat both the batteries [1], and, however, the scenario of a battery frozen was supposed to be less critical than the continuous discharging of the batteries [2].

The thermostats chosen are the *Klixon 4-BT2*, which are represented in Figure 2.2(a). Their technical features are (Figure 2.2(b)):

- the set point is $7.2^oC \pm 4.4^oC$,
- the operating temperature is $19.9^oC \pm 4.0^oC$,
- mass $0.2g$,
- NASA qualified for space applications.

Insulator: an insulating foil is placed between the aluminium support and the batteries in order to isolate them. The *Sheldahl Polyester Netting* is exploited to this purpose. The thickness of the sheet is $0.007in \simeq 0.18mm$. However, data provided by its Product Bulletin [10] are not completely exhaustive, since the value of its thermal

[3]It is to emphasize that batteries are connected in parallel on the unregulated bus, so that the discharging would concern the two batteries (and not only the one associated to the failure).

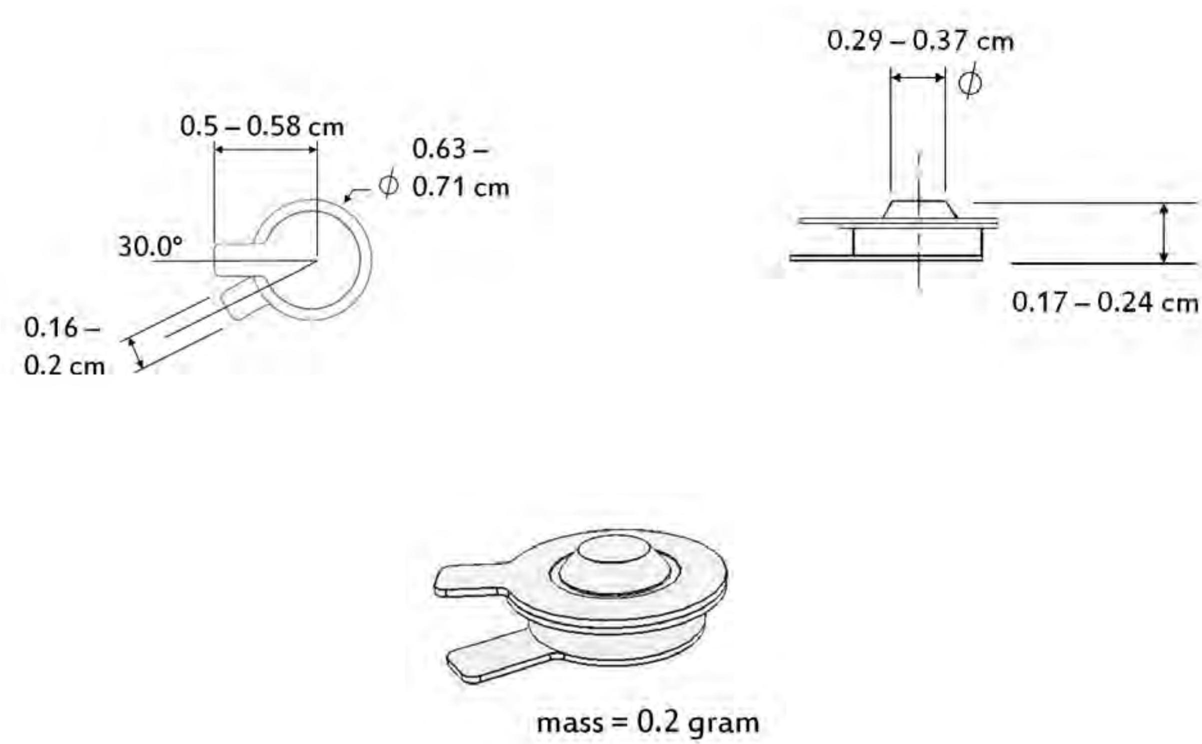

(a) Thermostat *Klixon 4-BT2*.

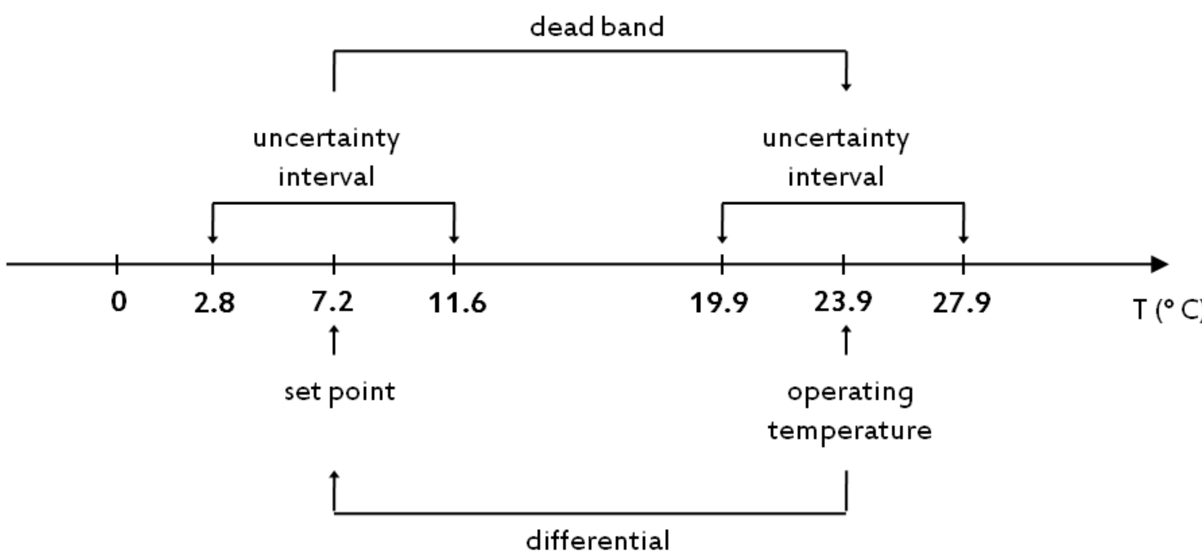

(b) Set point and operating temperature (with incertitude interval).

Figure 2.2: Characteristics of the thermostats exploited for OUFTI-1 [2].

conductivity is not clarified. They are glued on the batteries surface by means of the conductive glue *Stycast 2850FT*.

Furthermore, the BAT subsystem is also composed by:

Batteries: as already anticipated, two LiPo batteries *Kokam SLB603870H* are exploited. Their technical data are summarized in Appendix A.

Support: the vacuum test on the batteries performed in 2008-2009 [1] revealed that the batteries undergo deformations when submitted to extreme thermo-vacuum conditions. For this reason, a mechanical support (Figure 2.3) was designed to prevent this phenomenon. The batteries are housed side by side in this support, and it is integrated in the satellite as the other PCBs (see Figure 1.1(b)). Its material is the aluminium alloy *Al 7075-T6*.

Protection circuit: it is an electronic circuit to prevent batteries from over-charging, over-discharging and over-currents. In nominal conditions, the circuit monitors the voltage of the battery, but [11]:

- when the voltage of the batteries drops below the cut-off voltage, the Protection Circuit Module stops the discharging, and the current consumed is reduced to $2\mu A$,
- if during charging under normal condition, the battery voltage exceeds the over-charge detection voltage for longer than the delay time ($1.0s$), the charging is stopped,
- if the discharge current becomes equal or exceeds $3A$ for a time longer than the over current detection delay time, the circuit stops the discharge.

The integration of the BAT subsystem is shown in Figure 2.3.

2.2 Numerical modelling

In this Section, the numerical modelling of the BAT subsystem is illustrated. At first a description of the *ESATAN* model implemented by J.P. Nöel [2] in 2009-2010 is provided. Then, a simpler *Simulink* model is presented. This one is aimed at validating the results of the former during the design update of the BAT subsystem, described in Section 2.6.

2.2.1 ESATAN model implemented in [2]

A numerical model of the BAT subsystem was developed with *ESATAN-TMS* in [2]. More details about the realisation of a numerical model with this software, as well as the explication of the notions of Geometrical Mathematical Model (GMM) and Thermal Mathematical Model (TMM) exploited in this Section, are provided in Chapter 4, where the global model of OUFTI-1 is developed.

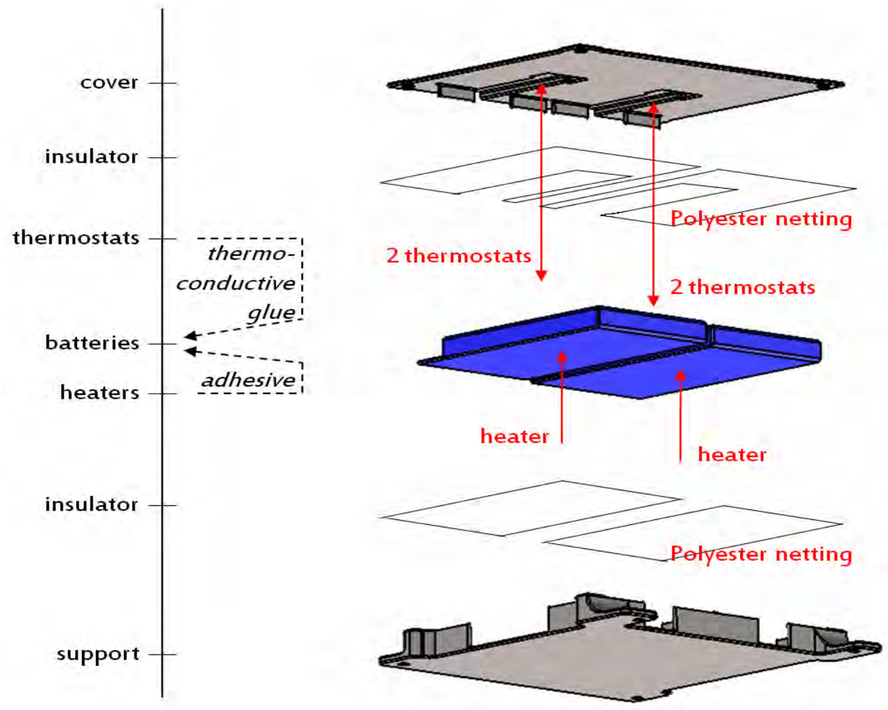

(a) Scheme

(b) Heater and battery

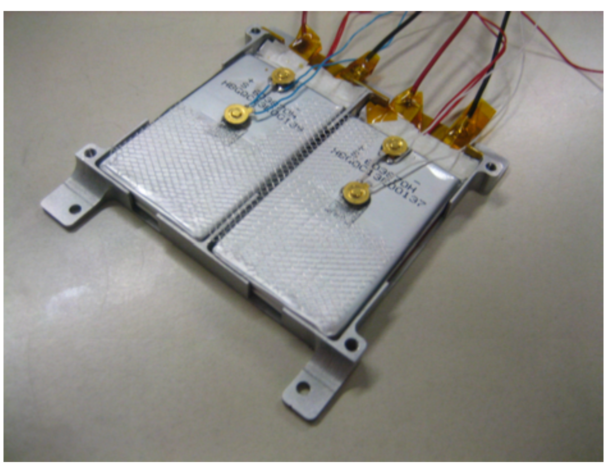

(c) Thermostats and insulator

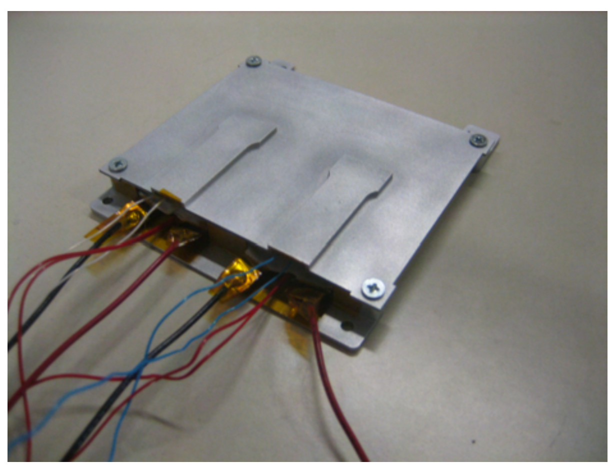

(d) Final integration

Figure 2.3: Integration of the BAT subsystem, according to [2].

Coating or material	**Emittance** [%]
Aluminium	3
Batteries	85
Copper	2
Insulator	65

Table 2.2: Optical properties of the surfaces of the BAT model, from [12].

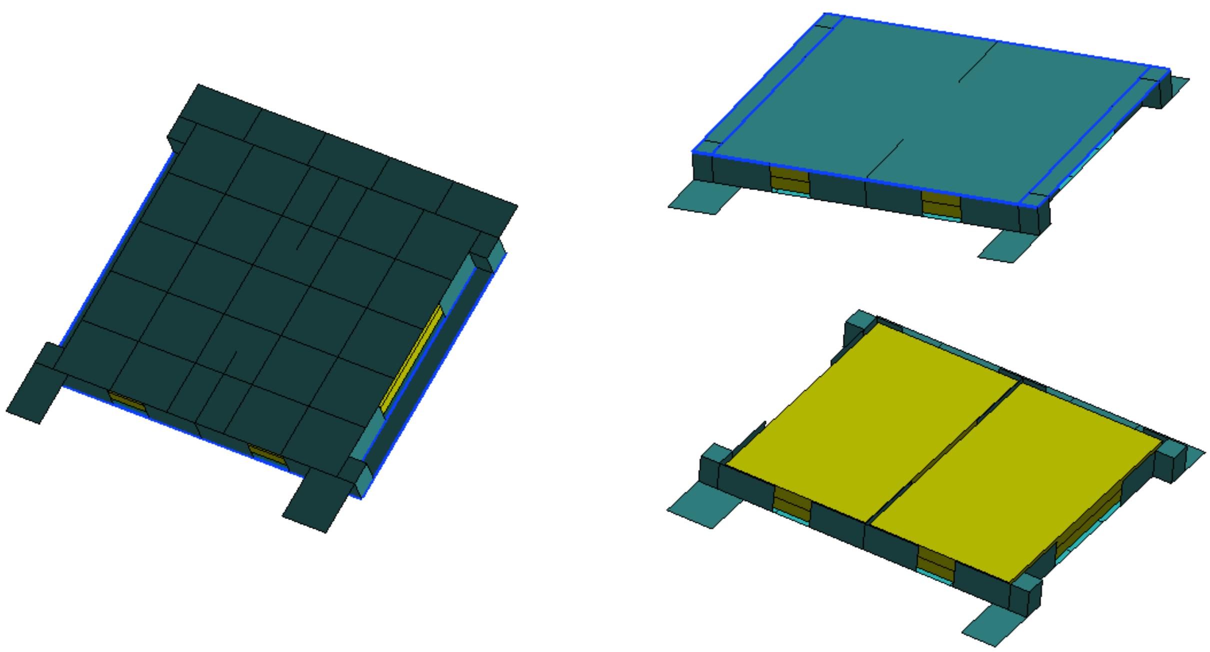

Figure 2.4: Geometry of the numerical model of the BAT subsystem implemented in [2] (*ESATAN* model).

The GMM of the model is shown in Figure 2.4; its optical coatings are listed in Table 2.2[4], and they are applied to the following surfaces:

Insulator: on the surfaces of the support in contact with the batteries,

Aluminium: on all the other surfaces of the support,

Batteries: on the surface of the batteries,

Copper: on the temperature-regulated panel (not represented in Figure 2.4), which is posed $20mm$ below the base of the support,

Inactive node: a Multi Layer Insulation (MLI) tent (not represented in Figure 2.4) wraps the whole system, so that radiative dissipation with the environment does not occur. A radiately inactive surface is equivalent to a surface with emittance equal to zero.

It is to emphasize that only the values of the infra-red emittance are listed in Table 2.2 (and not the values of the solar absorptance), since this model was exploited to simulate the behaviour of the system during the ground test (i.e., there is not solar flux).

Concerning the TMM, the properties of the bulk materials are listed in Table 2.3[5]. The nodal breakdown of the model consists of:

- 48 nodes for the base of the support. In particular 25 nodes are exploited to model the rectangular shell at the basis, so that its distribution of temperature is well detailed,
- 3 nodes for the cover of the support,
- 4 nodes for the batteries (i.e., 2 per battery),
- 1 node for the temperature-regulated panel,
- 1 node for the MLI tent.

The bulk properties of the copper and MLI tent are not reported, since the temperature-regulated panel is a boundary node (i.e., imposed temperature), and the MLI tent is an inactive node (i.e., no radiative or conductive exchange with the system).

Concerning the Linear Conductance (GL), they are computed as described in Section 4.1.2, but no conductance is considered between batteries and support (i.e, the insulator is supposed to be perfect).

The power of the heaters is directly injected as Internal Source of Power (QI) in one node of the batteries (the one on the side of the heater).

[4] The reference of this table is provided in the file of the model, but not directly in [2]

[5] The specific heat and the transversal thermal conductivity of the batteries were experimentally identified by L. Jacques [1].

Bulk material	C_s $\left[\frac{J}{kg\ K}\right]$	k $\left[\frac{W}{m\ K}\right]$	ρ $\left[\frac{kg}{m^3}\right]$	**Reference**
Aluminium	960	130	2810	[13]
Batteries	1350	1.11	1890	[1]

Table 2.3: Bulk properties of the materials of the *ESATAN* numerical model. C_s is the specific heat, k is the thermal conductivity, and ρ is the density.

Remarks on the numerical model

The following considerations concern the numerical model just described:

- A parametric analysis on the model was not performed, and, nonetheless, some of the input data are even optimistic. For instance, the emissivity of the aluminium is set to 3%, but other references like [14], or even the same [12] provide values up to the 10%.

- Neglecting the conductivity through the insulator is an hypothesis too hazardous. In fact, consider the simplified stationary model of Figure 2.5; this model represents an optimistic approximation of the numerical model described in Section 2.2 for two reasons:

  - radiative exchange is neglected,
  - in the *ESATAN* model (and during the test described in Section 2.3), the support is directly screwed on the temperature-regulated panel, so that conductive heat transfer between support and panel is enhanced. On the contrary, this simplified model considers that the $4mm$-length aluminium (Al6061-T6) spacers[6] are exploited to connect the support and the panel[7].

  However, the conduction through the insulator is taken into account. Since the thermal conductivity of the insulator is not referenced, the one of the teflon[8] is retained ($k_{ins} = 0.24 \frac{W}{m\ K}$ [15]).

  The thermal resistance between batteries and support, R_{ins}, and the resistance through the spacers, R_{sp} are, respectively:

$$R_{ins} = \frac{1}{A_{bat}\ FR}\left(\frac{t_{ins}}{k_{ins}} + \frac{2}{GL_{cont} + \frac{t_{bat}}{2\ k_{bat}}}\right) \tag{2.3}$$

$$R_{sp} = 4\ \frac{l_{sp}}{k_{sp}\ A_{sp}} \tag{2.4}$$

  where:

[6] The same spacers that separate the BAT support by the xEPS in the satellite.
[7] Spacers are exploited for this simplified model so that the joint is more representative of the real one.
[8] It will be considered as possible substitute of the actual insulator in Section 2.6.

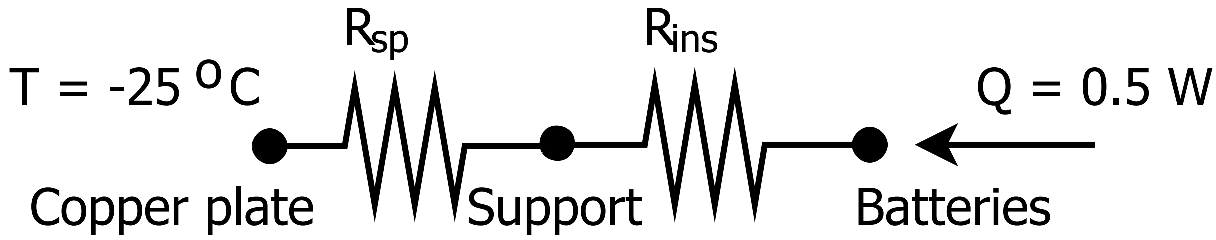

Figure 2.5: Simplified stationary model of BAT. The radiative exchange is neglected.

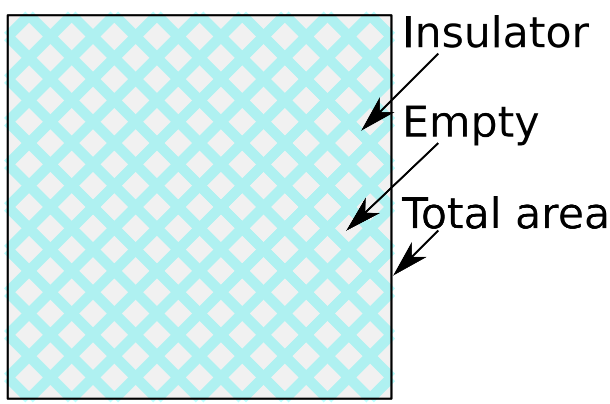

Figure 2.6: The fill ratio of a netting is defined as the ratio between the surface of the insulator (blue-light) and the total surface (black square).

- $A_{bat} \simeq 4 \cdot 37.5 \cdot 67.5 mm^2$ is the contact surface between support and batteries,
- FR is the fill ratio of the insulator (supposed equal to 50%), defined in Figure 2.6,
- $t_{ins} = 1.8mm$ is the thickness of the insulator,
- $GL_{cont} = 200\frac{W}{m^2\ K}$ is a optimistic estimation of the contact conductance (Figure 2.22). The factor 2 is due to the "double contact" (batteries-insulator and insulator-support)
- $\frac{t_{bat}}{2}$ and k_{bat} are half of the thickness and the thermal conductivity of the batteries (Tables A and 2.3),
- $l_{sp} = 4mm$, $A_{sp} = \pi\frac{d_{ext}^2 - d_{int^2}}{4} = \pi\frac{4.5^2-3.3^2}{4}$ and $k_{sp} = k_{Al6061-T6} = 160\frac{W}{m\ K}$ are the length, the cross section, and the thermal conductivity [16] of the four spacers.

With this data, the temperature of the support and of the batteries are, respectively:

$$T_{sup} = -24.6^oC \quad (2.5)$$
$$T_{bat} = -22.6^oC \quad (2.6)$$

This result is extremely pessimistic respect to the simulation of the *ESATAN* model discussed in Section 2.3 (and shown in Figure 2.9), and it proves that it is necessary to reconsider the hypothesis of the perfect conductive insulation of the batteries.

- The thermal exchanges of this model are not representative of the real behaviour of the system in the satellite. In fact, the emittance of the copper panel is extremely low (2%), while the one of the PCB is supposed to be 80% [1], and the GL from the support is enhanced by screwing it to the temperature-regulated panel, while conduction occurs through the spacers in the satellite.

2.2.2 Simulink model

This model is introduced at this point of the Chapter for sake of clarity. However, it is just going to be employed in Section 2.6, in order to provide a validation of the results of the *ESATAN* model.

The strength point of a *Simulink* model is the simplicity, which makes its results reliable (though approximated) and eases its debug. On the contrary, a *ESAtAN* model requires a more complex definition of the geometry (which however can be easily verified with the *ESATAN* Graphical User Interface (GUI)) and, most of all, a hand-computed list of the GL, which makes *ESATAN* models more susceptible to error.

The *Simulink* model implemented exploits the *SimScape* toolbox, which provides blocks to perform electrical, thermal, and mechanical simulations.

The high level scheme of the model is shown in Figure 2.7(a). It consists of three diffusion nodes (i.e., with thermal inertia), one for each battery and one for the support, and one boundary node, the temperature-regulated panel one (Figure 2.7(b)). The only thermal exchanges occurring are:

- conduction (through spacers) and radiation between temperature-regulated panel and support,
- conduction (through insulator) and radiation between each battery and the support.

Finally, the heaters (Figure 2.7(c)) are controlled by the temperature of the corresponding battery, and their power is injected on the battery node itself.

The parameters defining the diffusion nodes are listed in Table 2.4, while the parameters of the GL and Radiative Conductor (GR) will be defined in Section 2.6, according to different design that they will have to model.

2.3 Test performed in 2010

A development test of the BAT subsystem was performed at the CSL in 2010. This Section is devoted to the analysis of its results. However, a brief description of the test procedure is provided at first (more details in [2]).

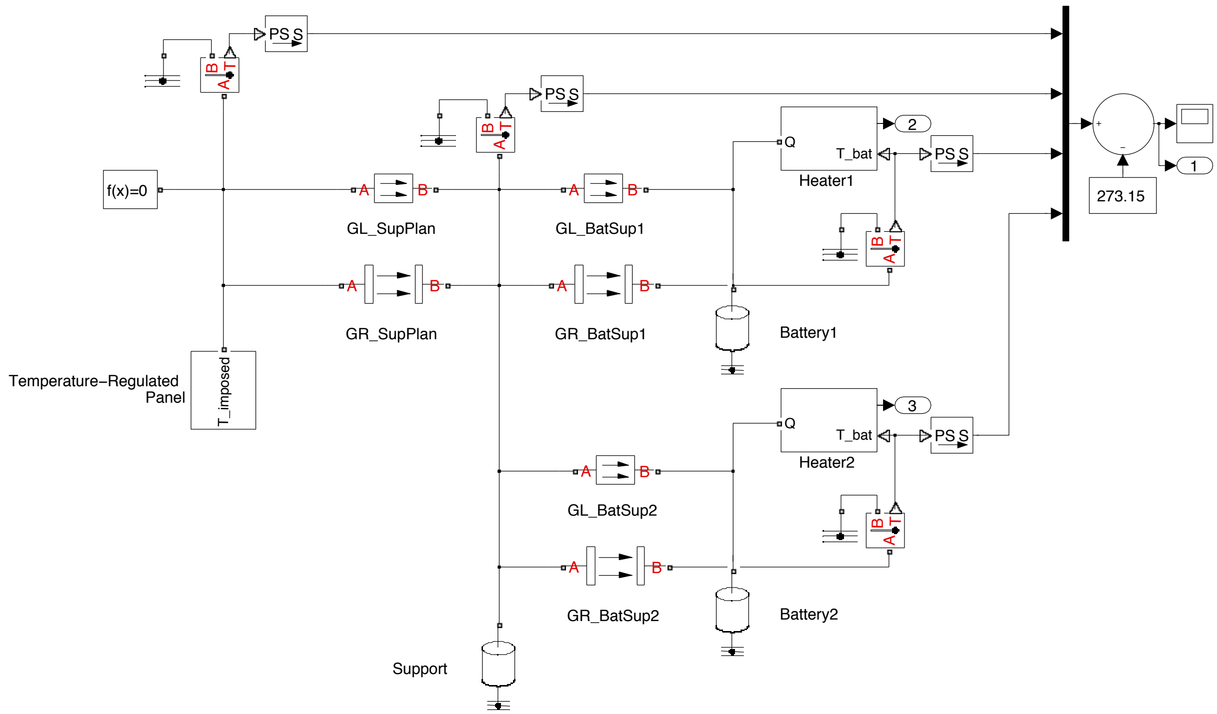

(a) High level scheme

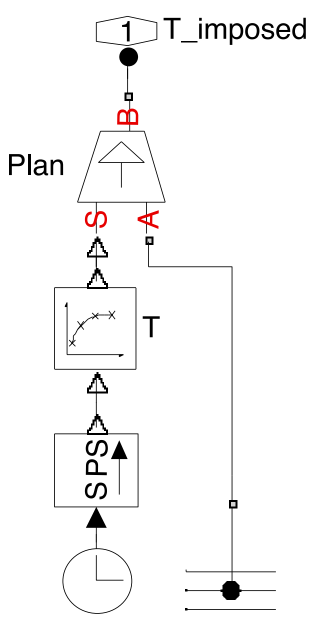

(b) Temperature-regulated panel

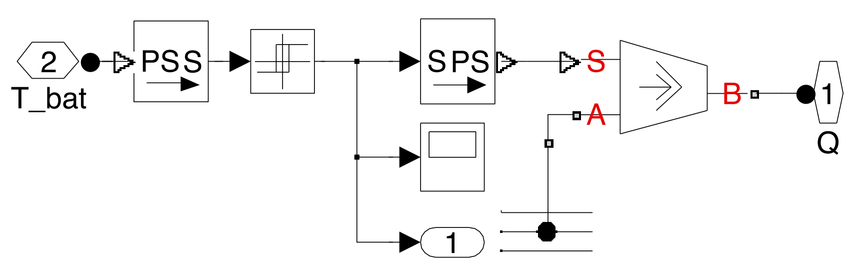

(c) Heater

Figure 2.7: Simulink model of BAT.

Node	M $[g]$	C_s $[\frac{J}{kg\ K}]$	**Reference**
Support	46	960	[17], [13]
Battery 1	32	1350	[4], [1]
Battery 2	32	1350	[4], [1]

Table 2.4: Parameters of the diffusion nodes of the *Simulink* model (mass and specific heat).

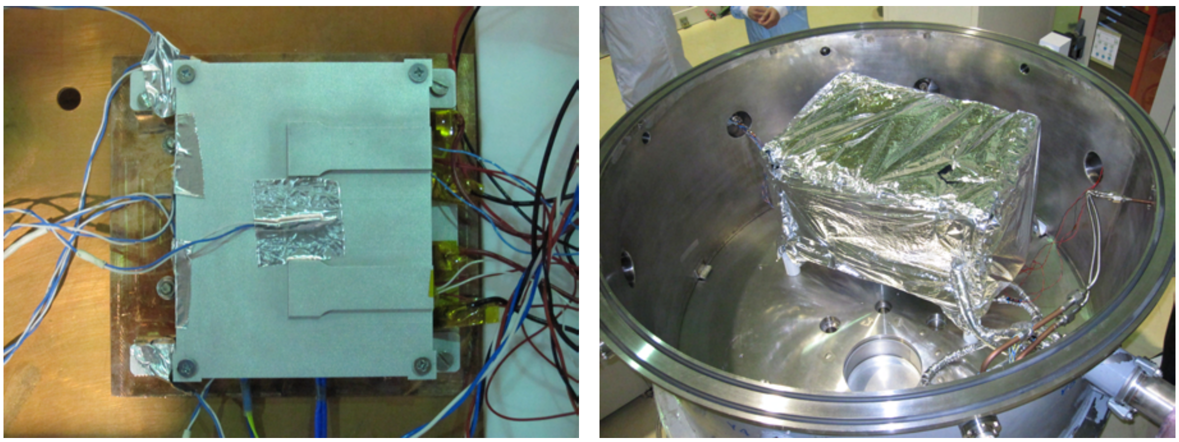

(a) Specimen and copper interface (b) MLI tent and *FOCAL1.5*

Figure 2.8: Pictures of the test of 2010 at the CSL.

2.3.1 Test procedure (foreseen by [2])

As already anticipated, the test is performed at the CSL in the *FOCAL1.5*, a vacuum chamber with diameter of $1.5m$. The specimen (i.e., BAT subsystem, Figure 2.8(a)) is screwed on the temperature-regulated panel, and the temperature profile that has to be imposed is shown in Figure 2.9. The temperature of the batteries and of the support forecast by the numerical model described in Section 2.2 are shown in Figure 2.9, too. The MLI tent, shown in Figure 2.8(b), was exploited to contain radiative losses with the environment.

Two cold and hot[9] cycles are foreseen. Their temperature levels are:

- -25^oC for the cold cases (i.e., 10^oC less than the coldest temperature experienced by the batteries in the simulations in [1])
- 50^oC for the cold cases (i.e., 10^oC more than the hottest temperature experienced by the batteries in the simulations in [1])

each cold case lasts in $40'$ and each hot case in $110'$. During the second cold cycle, a failure of one heater is simulated.

[9]However, just one hot cycle was actually performed.

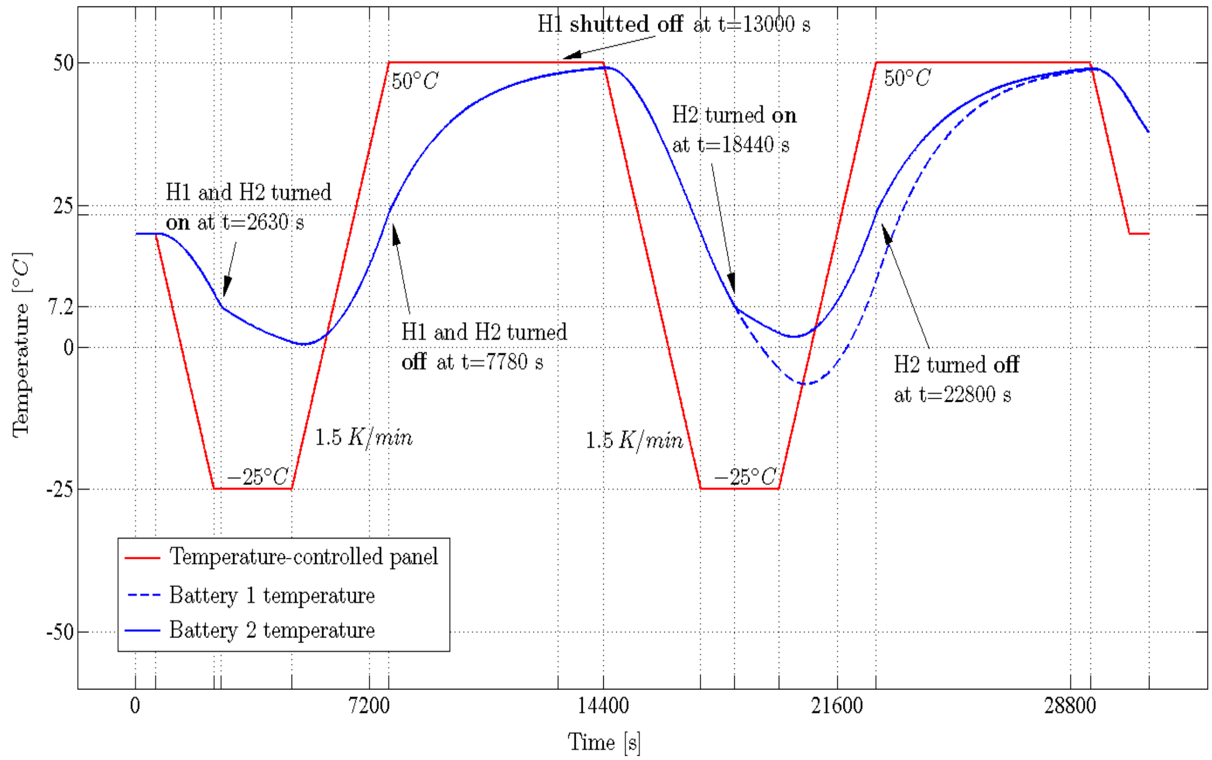

(a) Batteries

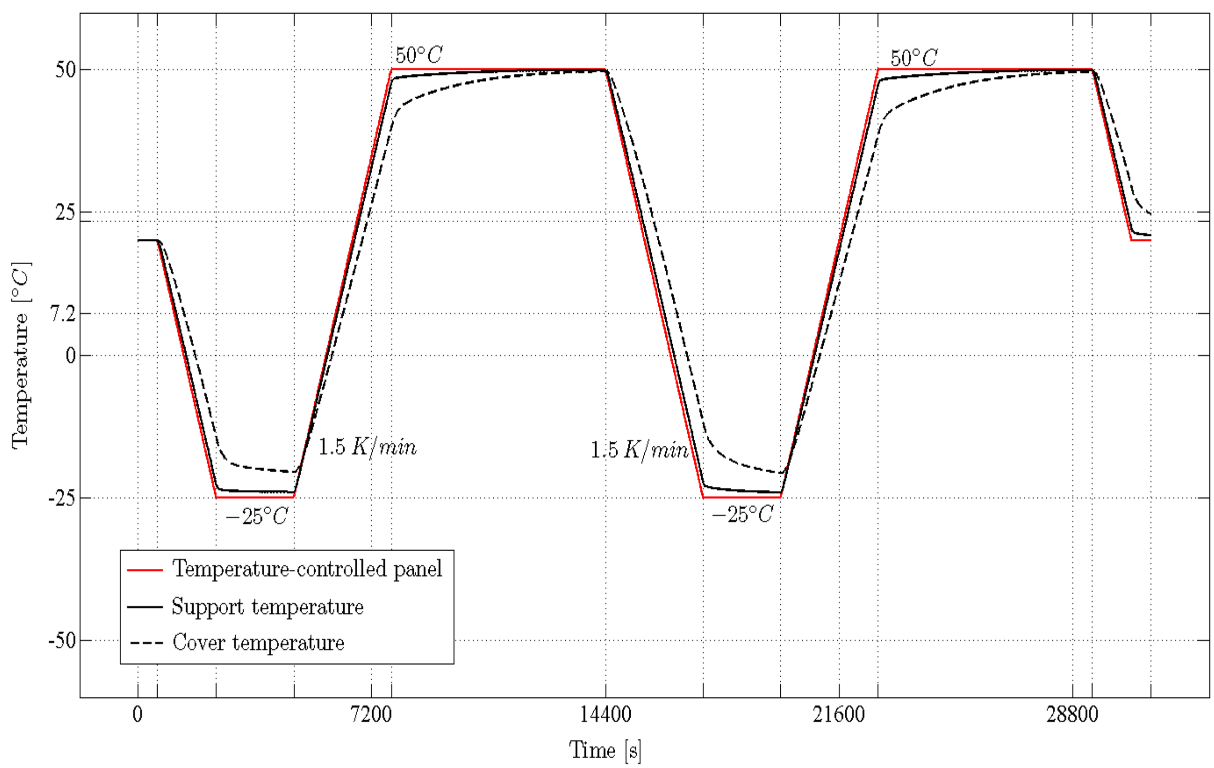

(b) Support and cover

Figure 2.9: Numerical simulation of the test of 2010, obtained with the *ESATAN* model described in Section 2.2 (from [2]).

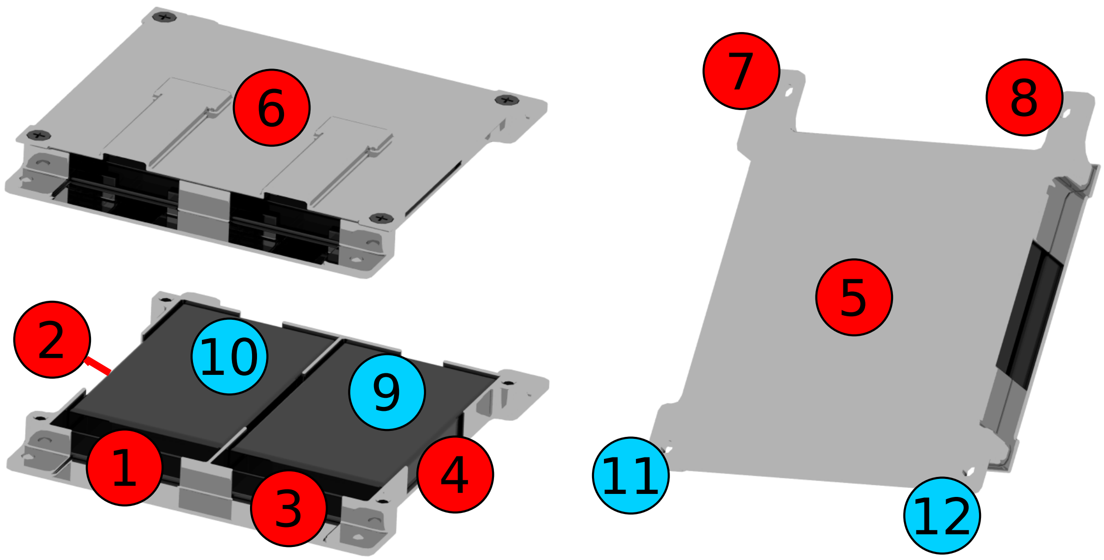

Figure 2.10: Location of the thermocouples during the test of 2010. The "thermocouples blue" where forecast by the procedure in [2], but they were not employed during the test.

The temperature transducers are located as follow (the enumeration is the one of Figure 2.10):

- two on each battery (1-4),
- one at the center of the base of the support (5),
- one at the center of the cover (6),
- two at the connection point between temperature-regulated panel and support.

Furthermore 4 thermocouples are also placed on the temperature-regulated panel, but their exact location was not registered. A thermocouple at the center of each battery was also forecast (blue circles of Figure 2.10) but, unlucky, it was not possible to place them because of technical troubles emerged during their integration.

The objectives of the test are:

Thermal objectives:

T1 verify the proper functioning of the thermostats,

T2 prove that the batteries do not exceed their operational range ($0 \sim 40^oC$),

T3 provide data for thermal correlation of the system,

T4 assess the impact of losing a heater on the system behaviour.

Electrical objectives:

E1 compute the energy dissipated by the batteries during the heating phase,

E2 verify that the batteries voltage never drops below the cut-off voltage.

Mechanical objective (**M1**) is to verify that the support prevents the under-vacuum deformations of the batteries.

2.3.2 Analysis of the results

The results of the test are shown in Figures 2.11 and 2.12[10], and the achievement of the different objectives, listed in Section 2.3.1, is discussed in Table 2.5.

The following remarks concern the results:

- Batteries experienced too low temperature (about -20^oC), largely below the threshold of the 0^oC foreseen by the numerical simulation (Figure 2.12). This represents the most important problem encountered during the test, since it proves that the main objective of the TCS is not fulfilled. Furthermore, numerical results differ from the experimental ones, so that a model updating procedure was performed (Section 2.5) to be able to simulate the real behaviour of the system more accurately. The results of the updated model show that the conduction through the insulator is mostly responsible for the heat loss, and thus it cannot be neglected, as already anticipated with the qualitative example in Section 2.2.

- At the beginning of the second cold case, the voltage of the batteries dropped to $0V$ till the end of the test, when it finally came back to its nominal value (Figure 2.11, third diagram). This issue is still unsolved, because of lack of data. The only possible explanation might be the failure of the voltage transducers, but it does not explain why the tension rised up at the end of the test, and why this phenomenon happened with both the batteries.

- During the first cycle, both the heaters switched on and off, but, while the second one did it at $(5.0 \pm 1)^oC$ and $(22.0 \pm 1)^oC$[11], the first one turned on at $(-0.7 \pm 1)^oC$ and off at $(20.0 \pm 1)^oC$, so that heating process starts too late and below the incertitude interval of the set point of the thermostats. Probably, this is due to the fact that the thermocouples are placed on the side of the battery, so that the temperature of its core might be different. However, an ambient-condition test was performed to asses the proper functioning of the thermostats (Section 2.7.1).

- Outgassing occurred during the first hot cycle (Figure 2.11, second diagram). The specifications of *Vega* about the outgassing are [18]:

"The spacecraft materials must satisfy the following outgassing criteria:

[10] In these Figures, the signal of the thermocouples 1 and 3 are confused with the one of the thermocouples 2 and 4, respectively, since the maximum difference between them in function of time is of the order of $10^{-3}\ ^oC$

[11] 1^oC being the accuracy of the thermocouples for absolute measurements.

Objective	Fulfilled? Yes	No	Partial	Remarks
T1			×	Both thermostats closed the circuit during the first cold cycle (Figure 2.11). However, the temperature of one battery was below the incertitude interval of the set point of the thermostats (Figure 2.2(b)), at this moment. No data are available for the second cold cycle.
T2		×		The temperature of the batteries largely dropped below the threshold of the 0^oC (Figure 2.12).
T3	×			Data for the correlation of the thermal numerical model are available.
T4		×		Voltage of batteries and heaters dropped to zero from the beginning of the second cold cycle till the end of the test (Figure 2.11).
E1			×	It is possible to compute the energy dissipated just during the first cold cycle (for the same reason of the previous point).
E2		×		The voltage of the batteries suddenly drop to zero during the second cold cycle.
M1	×			The support was able to contain the under vacuum deformations of the batteries.

Table 2.5: Fulfilment of the test objectives listed in Section 2.3.1.

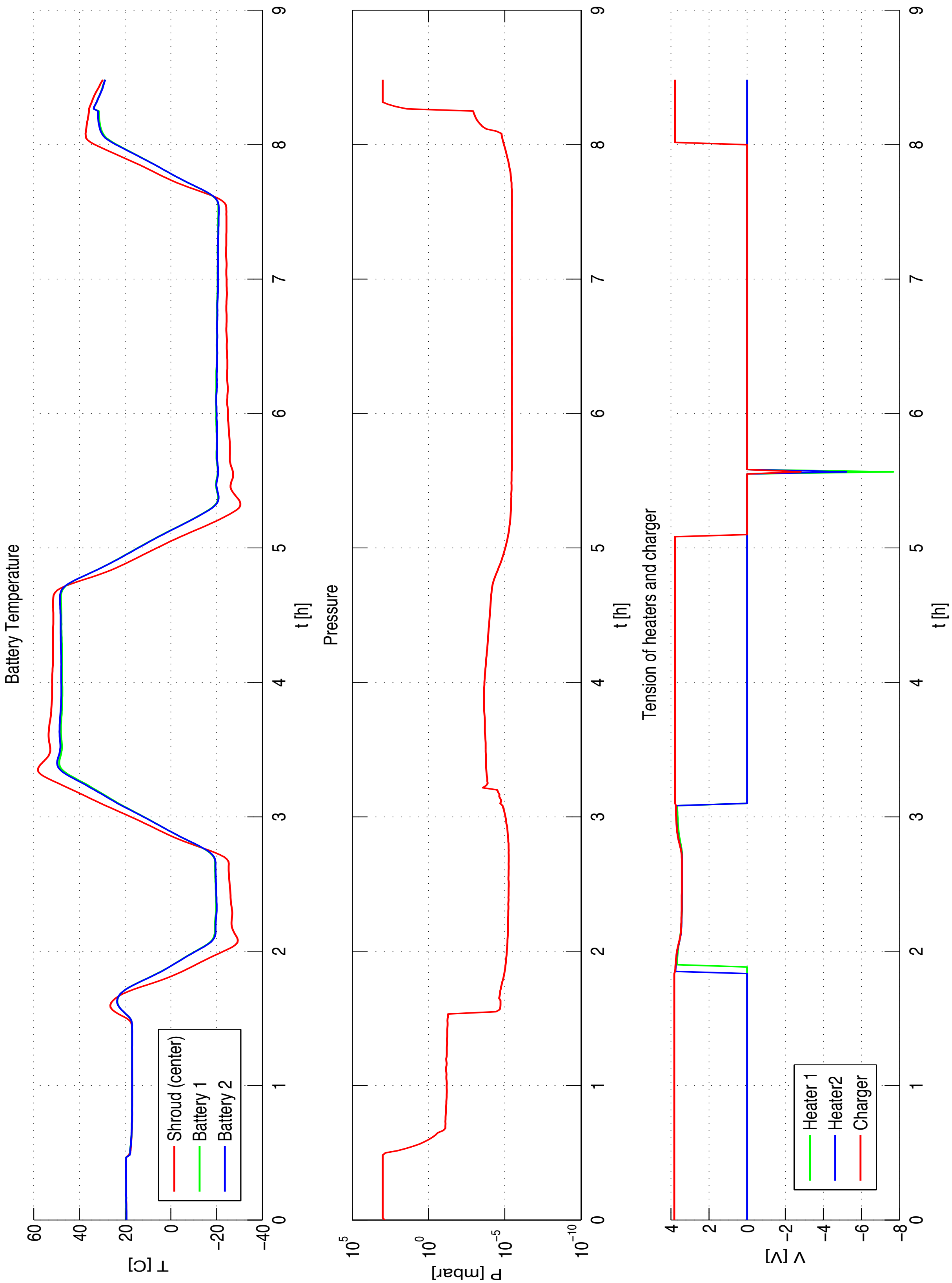

Figure 2.11: Results of the test performed in 2010. Temperature of the batteries, pressure in the vacuum vessel and voltage of the heaters.

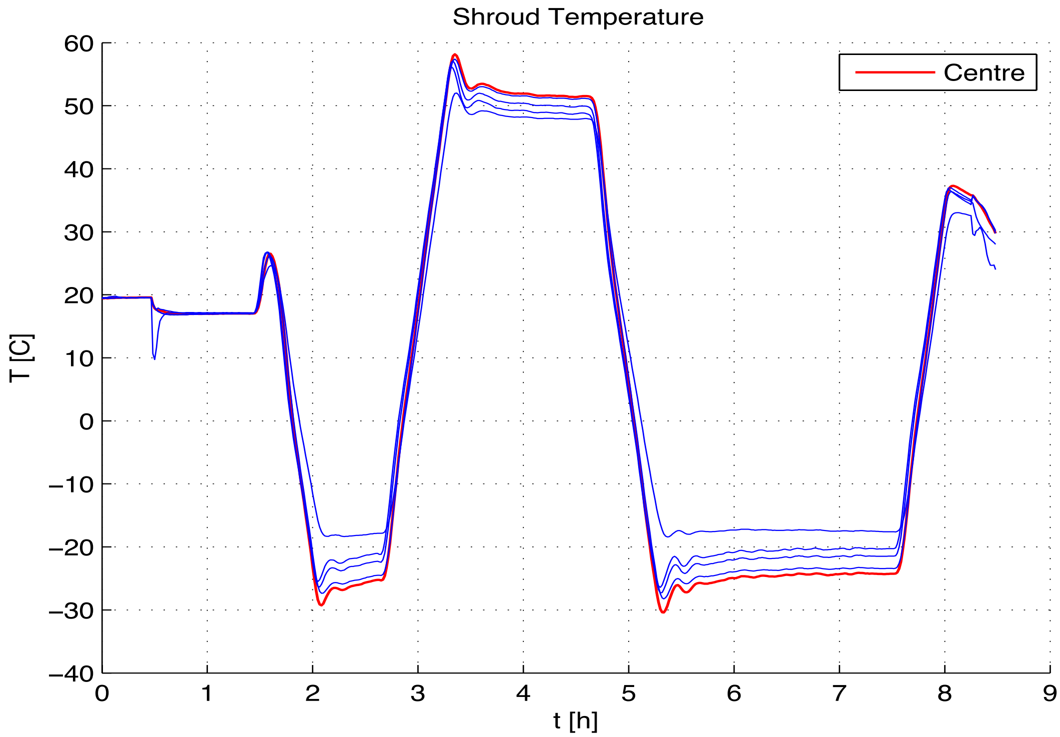

(a) Temperature-regulated panel

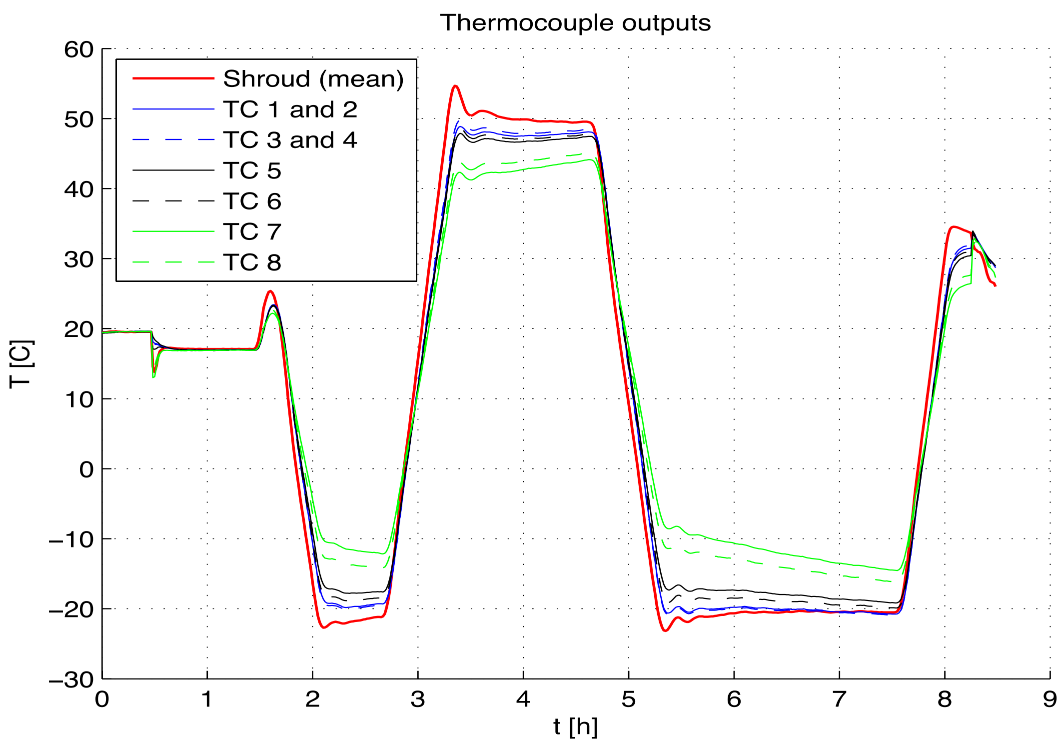

(b) Thermocouples on the specimen

Figure 2.12: Outputs of the thermocouples in the BAT test of 2010.

  - *Total Mass Loss (TML)* $\leq 1\%$*;*
  - *Collected Volatile Condensable Material (CVCM)* $\leq 0.1\%$*."*

Nonetheless, the data provided by the test are not detailed enough to verify this requirement. However, the list of the materials and components present in the vacuum chamber is provided in Table 2.6. All of them are space approved, but a question mark is posed on the heaters because of their PSA. In fact, [19] states:

> *"The #10 PSA release liner is more susceptible to moisture absorption problems than the #16 and #19 PSA release liners. Avoid moisture problems by keeping all three types of PSA in a dry environment or in the original sealed packaging until it is used."*

Another possible reason might be the entrapment of air between the heaters and the batteries. To this purpose, it is stated in [12]:

> *"Prior to the formal start of testing, steps are taken to preclude the unwarranted accumulation of moisture within the unsealed unit. This is accomplished by imposing a number of pretest cycles using dry air or nitrogen, [...] To further reduce the risk of condensation, the test begins and ends with hot cycles or half-cycles."*

Indeed, the test began with half-cycle, but pretest cycles were not performed. Furthermore, the hot-start is advised in [20], too. In my opinion, this is the most suitable explanation of the problem, although numerical data are too difficult to estimate. On the other hand, the air trapped might also be responsible of a loss of efficiency of the heaters, since an important contact resistance would be placed between them and the batteries.

- By focusing on the discharging phase (i.e., heaters on) of the voltage diagram (Figure 2.11, third diagram), it emerges that at first the voltage of the batteries drops, but then it starts to grow up (still during discharge). Nonetheless, such a phenomenon is qualitatively explained by considering the discharge curves of figure 2.13: as heaters switch on, voltage drops because of batteries discharge, but, since heaters are a simple electrical resistance (under the electrical point of view), their voltage is proportional to the current, and so the current itself has to drop down too, causing the shift on an upper characteristic curve, and so an increase of the voltage.

- Concerning the objective **E1** (Section 2.3.1), the energy dissipated by one heater, E_h, is computed as the integral of the power supplied, P_h, in function of time. For the first cold cycle it is equal to:

$$E_h = \int_{t_{on}}^{t_{off}} P_h \; dt = \int_{t_{on}}^{t_{off}} \frac{V_{bat}^2}{R_h} \; dt \tag{2.7}$$

	Material or component	Outgassing?
BAT components	Aluminium 7075-T6	no
	Batteries Kokam SLB603870H	no
	Heaters HK5950	?
	Thermostats Klixon 4BT-2	no
	Insulator Sheldahal polyester netting	no
	Aluminium screws	no
	Glue Stycast 2850FT	no
	Protection Circuit Module	no
Test instrumentation	Copper	no
	MLI	no
	Teflon insulation plane	no
	FR4 board	no
	Temperature sensors	no
	Electrical Cables (TEFLON insulated)	no
	Welding material (Sn-Pb)	no

Table 2.6: Outgassing issue: list of the materials and components in the vacuum chamber.

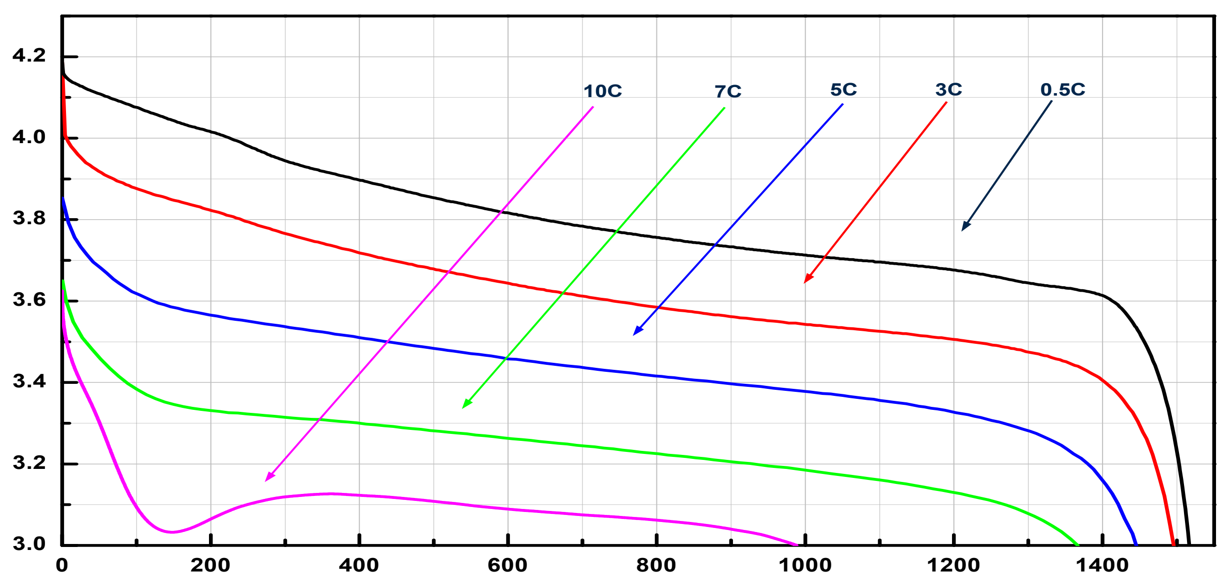

Figure 2.13: Discharge characteristics of the battery SLB 603870H at various currents: voltage $[V]$ in function of time $[s]$ (from [21]).

where t_{on} and t_{off} are the time when heaters switch on and off, respectively, V_{bat} is the voltage of the batteries, and R_h is the resistance of the heaters. The power dissipated by the two batteries is thus $E_b = E_h^{(1)} + E_h^{(2)} \simeq 4300J$

The capacity and the nominal voltage of the batteries are 1.5 Ah and 3.7 V, respectively. The maximum available energy per battery is their product: $5.55Wh = 19980J$ ($2 \times 19980J = 39960J$ is thus the total energy). So, the energy dissipated by the heaters during the first cold case is about the 11% of the total available energy.

- A temperature gap between batteries and temperature-regulated panel is also present during the hot case. This might be due to a radiative loss with the environment (the walls of the vacuum vessel are supposed to be at ambient temperature during the test).

  Such gap is about 5^oC, if just the temperature of the center of the panel is considered. However, since the emittance of the copper is small (about 2%), and the exchanges are dominated by conduction[12], there is no reason to considerate just the temperature of this transducer and, thus, the output of all the thermocouples on the temperature-regulated panel are averaged. In this way, the gap is about 2^oC.

- As shown in Figure 2.12, the temperature of the batteries and the support lies between the one of the temperature-regulated panel and the one of the screw points (thermocouples 7 and 8), while, on the contrary, the latter are supposed to have the temperature closest to the one of the copper plate (because of the high GL between them).

  As it will be discussed in Section 2.5, there is no way to correlate this occurrence with the numerical model, so that these signal are supposed to be unreliable. Probably, this is due to the fact that these thermocouples are not installed properly, because of the particular geometry of the joints.

2.4 Sensitivity analysis of the numerical model

Before proceeding with the correlation, a sensitivity analysis of the numerical model is performed. This analysis is aimed at assessing the relative importance of the parameters of the numerical model described in Section 2.2, and at identifying the most critical among them.

At the beginning of a sensitivity analysis, two questions have to be answered:

1. Which parameters have to be considered? They might be either physical properties (e.g., thermal conductivities, specific heat, optical properties) or local parameters (e.g., a GL between two nodes).

[12] i.e., the temperature close to the joints is more important than the one of the center of the copper panel.

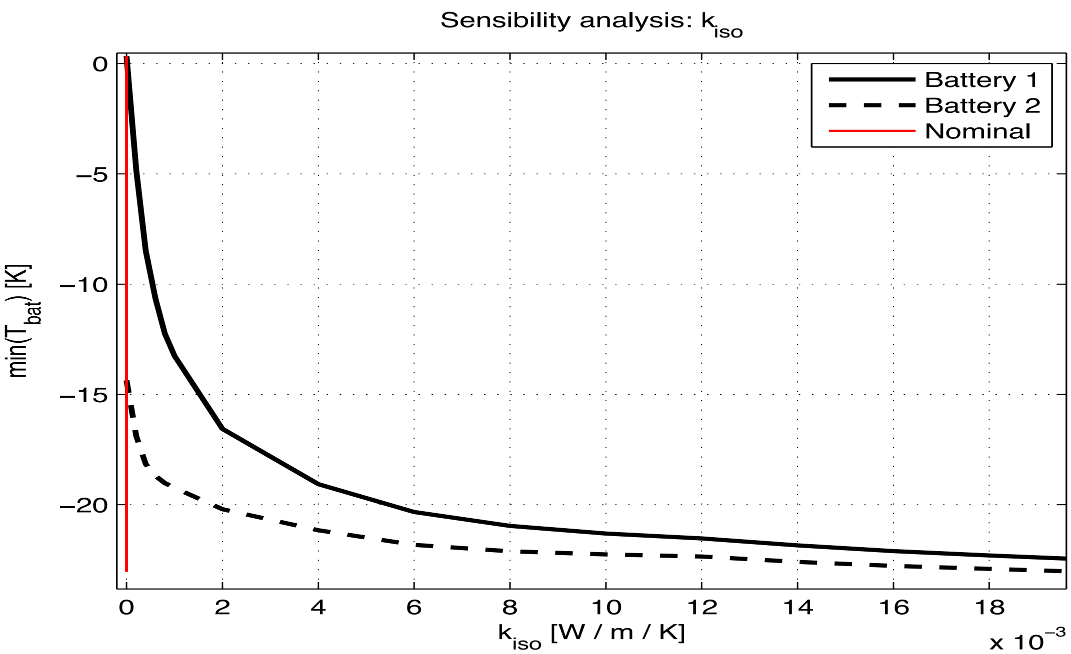

Figure 2.14: Sensitivity analysis: equivalent thermal conductivity of the insulator.

2. What is the figure of merit? I.e., respect to which function (of the output temperatures), the sensibilities of the various parameters have to be computed?

The sensitivity analysis is then performed by assessing the variation of the figure of merit in function of the independent variations of the selected parameters (i.e., one-by-one).

Concerning the first question, evidently, not all the parameters of the numerical model can be tailored, so that two criterion are exploited for their selection:

- the most unknown and uncertain parameters,
- the one supposed to be the most critical (i.e., whose sensibility is supposed to be high), since their identification has to be performed accurately.

For these reasons, all the optical properties are not considered in this sensitivity analysis. In fact, the radiative exchange between two surfaces is proportional to the fourth power of the difference between their temperatures, and, in the test of 2010, the temperature of all the components are always close one to the other, so that the heat transfer is dominated by the conduction (Figure 2.20).

So, the parameters considered for the sensitivity analysis are:

- the equivalent thermal conductivity of the insulator, $k_{ins}^{(eq)}$ (because of the reason explained in Section 2.2). $k_{ins}^{(eq)}$ is defined as the conductivity that provides a GL equivalent to the effective one, but through a insulator foil with fill ratio (Figure 2.6)

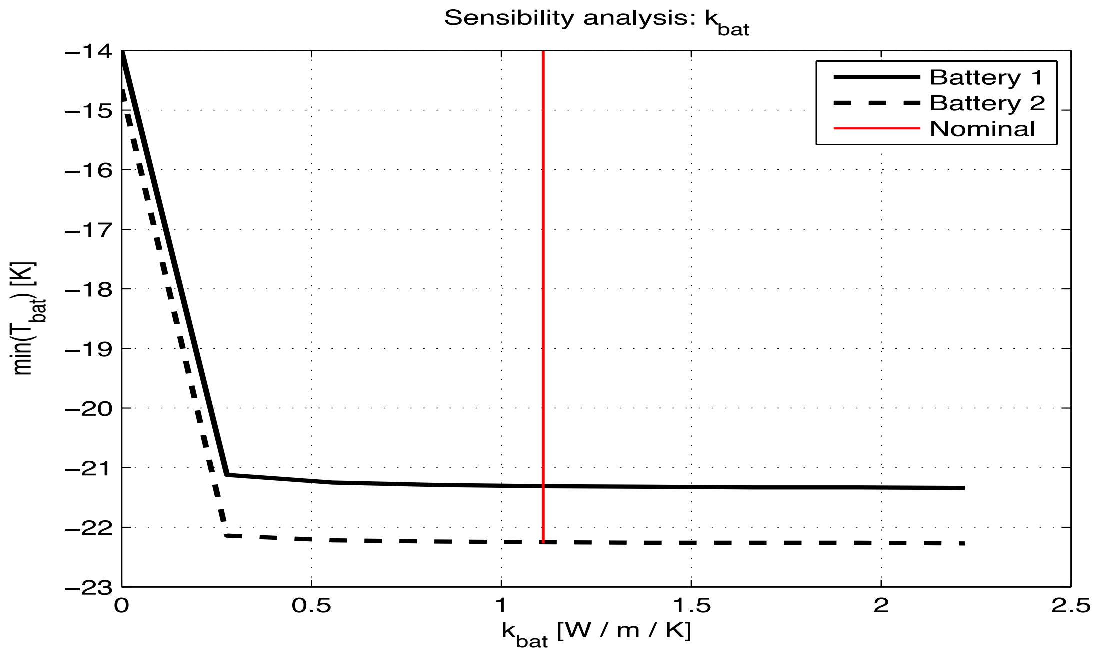

Figure 2.15: Sensitivity analysis: thermal conductivity of the battery.

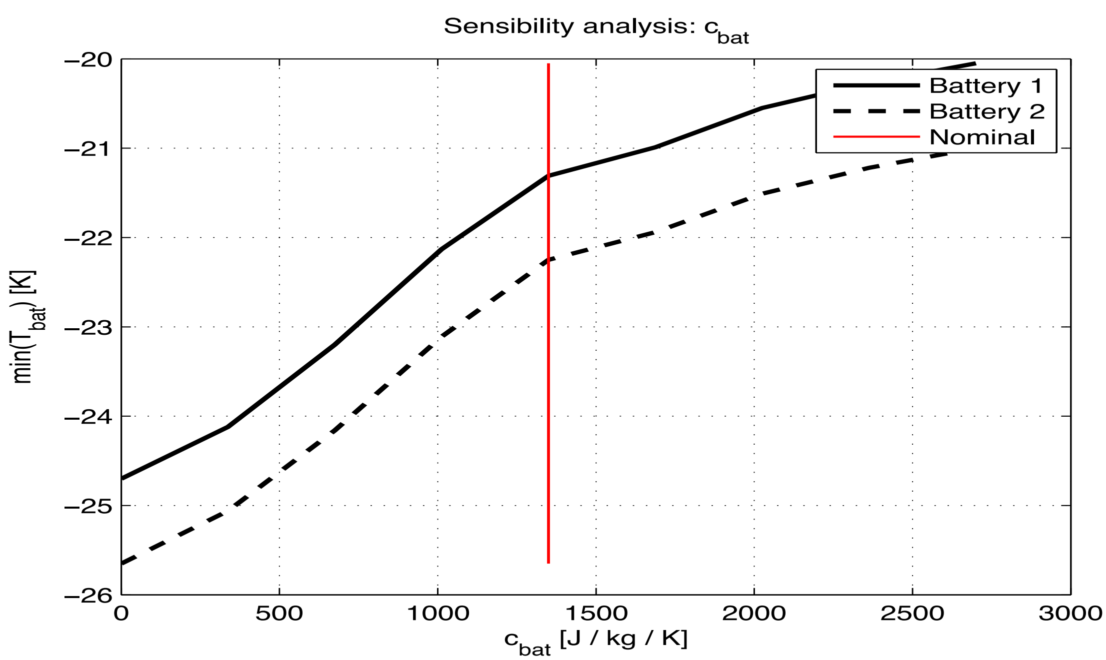

Figure 2.16: Sensitivity analysis: specific heat of the battery.

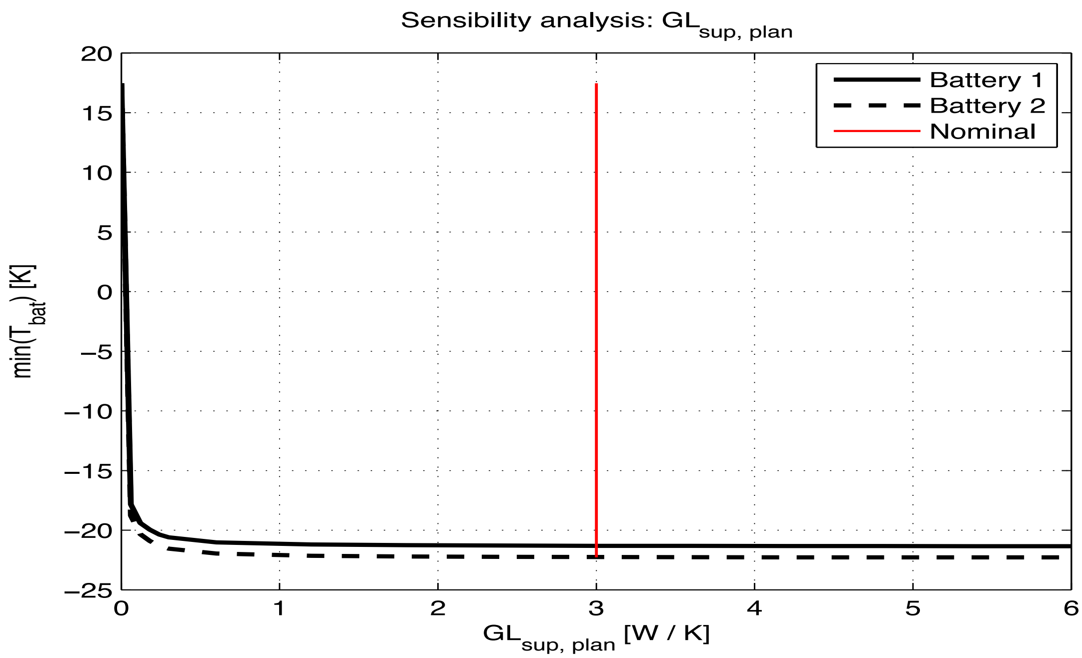

Figure 2.17: Sensitivity analysis: GL between support and copper interface.

equal to one and contact resistance null:

$$k_{ins}^{(eq)} \ : / \quad \frac{t_{ins}}{k_{ins}^{(eq)}\ A_{bat}} = \frac{1}{A_{bat}\ FR}\left(\frac{t_{ins}}{k_{ins}} + \frac{2}{GL_{cont} + \frac{t_{bat}}{2\ k_{bat}}}\right) \tag{2.8}$$

where all the variables were presented on Page 14.

- the thermal conductivity and the specific heat of the batteries, k_{bat} and C_{bat}, respectively;

- the GL between support and temperature-regulated panel at the four joints, $GL_{sup,plan}$, since its value was arbitrary set to $3\frac{W}{K}$ (which is largely grater than the other GL of the model).

Concerning the second question, the aim of the TCS is to prevent batteries from experiencing too low temperatures. For this reason, the minimum temperature attended by the batteries during the numerical simulation of the test (Figure 2.9) is retained as figure of merit.

The results of the sensitivity analysis are shown in Figures 2.14, 2.15, 2.16, 2.17. These graphs are obtained by sweeping on a parameter while keeping all the other variables to their nominal value defined in Section 2.2 (exception done for $k_{ins}^{(eq)}$, which is set to $10^{-3}\frac{W}{m\ K}$, since a conductivity null is not physical). The following conclusions emerge:

- as expected, the sensibility of the solution to small variations of $k_{ins}^{(eq)} \simeq 0\frac{W}{m\ K}$ is huge. For this reason, the hypothesis of perfect insulation is too hazardous;

- though $GL_{plan,sup}$ is the most difficult parameter to model (because of the particular geometry), the sensitivity analysis proves that the solution is not sensible for high values of this parameters. In fact, this condition means that the corresponding nodes of the support are essentially at the same temperature of the temperature-regulated panel;
- the sensibility respect to the other parameters (C_{bat} and k_{bat}) is negligible in proximity of their nominal values, so that an accurate identification of these parameters is not necessary.

2.5 Correlation between numerical model and experimental data

In this Section, the numerical model is correlated with the experimental results. To this purpose, the step to follow are:

- pairing the nodes of the numerical model with the thermocouples,
- identification of the steady states,
- choice of a correlation criterion,
- model update.

All these steps are considered one-by-one in the following paragraphs.

Pairing between nodes and thermocouples

In a lumped-parameters model developed in *ESATAN-TMS*, the list of the nodes is defined by the user itself, so that the pairing is eased.

The pairing is shown in Figure 2.18. It is to emphasize that, as stated in Section 2.3.2, the output of the thermocouples 1 and 3 are essentially undistinguishable by the output of 2 and 4, respectively, and thus they are considered just one time.

Identification of the steady states

[20] defines the *stabilised test temperature* as:

> *"specified temperature for equipment and subsystem tests that has been achieved and has not changed by more than 1^oC during the previous one-hour period"*

and, according to the CSL staff, this condition defines the steady states.

However, by considering this definition, any steady state is identified in the test results. Thus, the constraint about the one-hour period of stabilisation is removed, and the following stationary states are identified:

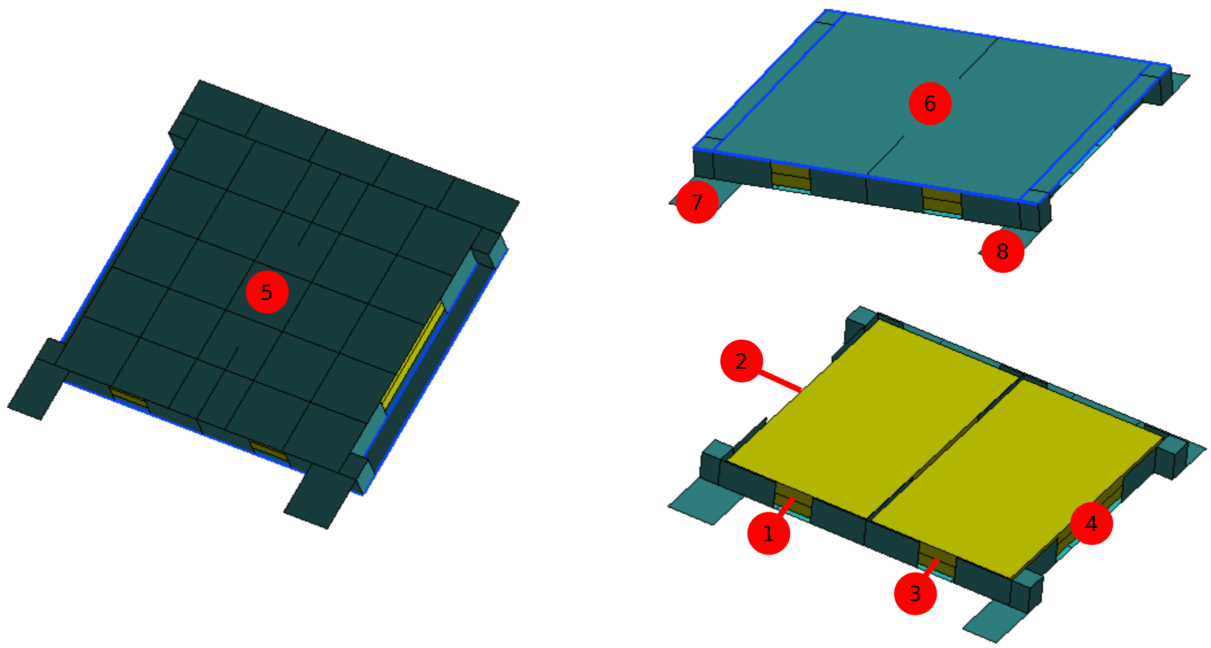

Figure 2.18: Pairing between nodes and thermocouples

Cold 1: during the first cold case, $t \in [2.4, 2.6]h$

Hot 1: during the hot case, $t \in [3.8, 4.6]h$

Cold 2: during the second cold case, $t \in [6.5, 7.5]h$

The corresponding temperatures of the transducers are listed in Table 2.7

Correlation criterion

The correlation criterion provided by the European Cooperation for Space Standardization (ECSS) is [20]:

	Cold 1	**Hot 1**	**Cold 2**
Time [h]	2.4-2.6	3.8-4.6	6.5-7.5
Panel	-22.0 ±0.5	49.5 ±0.5	-21.0 ±0.3
Sensor 1 & 2	-19.6 ±0.3	48.0 ±0.3	-20.5 ±0.5
Sensor 3 & 4	-19.8 ±0.3	47.6 ±0.3	-20.5 ±0.5
Sensor 5	-17.7 ±0.2	47.0 ±0.4	-18.6 ±0.6
Sensor 6	-18.6 ±0.2	47.4 ±0.4	-19.3 ±0.5
Sensor 7	-11.3 ±0.3	44.3 ±0.8	-13.4 ±1.1
Sensor 8	-13.9 ±0.2	43.3 ±0.8	-15.2 ±1.0

Table 2.7: Identification of the steady-states. Temperature are expressed in ^oC.

"As an adequate correlation criteria, an acceptable difference in the maximum temperature level between test temperatures (selected sensors) and TMM (corresponding nodes), a value for the mean deviation[13] is of between 1^oC and 2^oC, and a standard deviation of between 3^oC and 5^oC is normal practice."

so that, the two criterion are:

- the mean deviation of the error between the experimental and numerical data:

$$M = \frac{1}{N} \sum_{i=1}^{N} \left(T_i^{(num)} - T_i^{(exp)} \right) \tag{2.9}$$

- the standard deviation of the error between the experimental and numerical data:

$$\sigma = \sqrt{\sum_{i=1}^{N} \frac{\left(T_i^{(num)} - T_i^{(exp)} \right)^2}{N-1}} \tag{2.10}$$

where N is the number of transducers, $T_i^{(exp)}$ is the steady-state temperature of the $i-th$ transducer, and $T_i^{(num)}$ is the temperature node in the numerical model.

Model update

The updated parameters are:

1. the equivalent thermal conductivity of the insulator (defined in Section 2.4) from 0 to $0.0075 \frac{W}{m\ K}$. This parameter was updated as first, because of its remarkable sensitivity shown in Section 2.4,

2. introduction of a GR between the vacuum vessel and the MLI tent. To this purpose, the chamber is modelled as an isothermal aluminium cylinder (1.5m diameter), whose temperature is constant during the test (20^oC). In this way, the temperature gap that occurred during the case **Hot 1** is modelled[14]. The MLI tent is characterised by two different emittances. On the side of the specimen it is set to 5%, while on the side of the vacuum vessel it is set to 50% (i.e., emittance of Mylar according to [12][15]),

3. both heaters off during **Cold 2**. The test procedure was supposed to simulate a failure of one heater during this cycle. Nonetheless, the voltage drop described in Section 2.3.2 did not allowed to verify if this failure occurred either on one or two heaters,

[13] According to the ECSS [22], the mean deviation can be either positive or negative, so that the standard deviation is a more important indicator.

[14] Otherwise the temperature is uniform and equal to the one of the shroud, if any heat exchange occurs.

[15] The emissivity of Mylar, provided in this reference, sweeps from 28% (mil 0.15) to 77% (mil 5).

	Sensor	Temperature at each Iteration [^oC] 0	1	2	3	4	Experimental
Cold 1	Battery1	2.6	-20.6	-20	-20	-19.9	-19.6
	Battery2	2.6	-20.6	-20.1	-20.1	-19.9	-19.8
	Support	-21.3	-21.7	-21.2	-21.2	-20.8	-17.7
	Cover	-20.8	-21.8	-21.2	-21.2	-20.7	-18.6
	Foot1	-22	-21.9	-21.8	-21.8	-22.3	-11.3
	Foot2	-24	-21.9	-21.8	-21.8	-22.2	-13.9
Hot 1	Battery1	45.7	49.4	49.1	49.1	49.2	48
	Battery2	44.9	49.4	49.1	49.1	49.2	47.6
	Support	49	49.5	48.8	48.8	49.2	47
	Cover	49	49.5	49.2	49.2	49.1	47.4
	Foot1	49.3	49.4	49.5	49.5	49.4	44.3
	Foot2	49.4	49.4	49.5	49.5	49.5	43.3
Cold 2	Battery1	-0.2	-18.3	-19.1	-20.5	-20.5	-20.5
	Battery2	-15.2	-21	-20.7	-20.5	-20.5	-20.5
	Support	-16.9	-20.8	-20.4	-20	-20.7	-18.6
	Cover	-20.3	-20.8	-20.4	-20.2	-20.5	-19.3
	Foot1	-20.8	-21	-20.8	-21	-20.8	-13.4
	Foot2	-20.8	-21	-20.8	-20.8	-20.8	-15.2

Table 2.8: Correlation table: temperature of the numerical model at each iteration.

4. GL between heaters and batteries of $0.5\frac{W}{K}$. This conductance takes into account an eventual bad integration of the system, resulting in air trapped between heaters and batteries. In the previous model, the power of the heaters was directly introduced on one node of the batteries (i.e., this $GL \to \infty$).

The temperatures of the numerical model and the error committed at each iteration are listed in Tables 2.8 and 2.9, respectively. As already anticipated in Section 2.3.2, the thermocouples 7 and 8 (i.e., Foot1 and Foot2 in the Tables) are not considered in the computation of the correlation criterion, since their data are supposed to be unreliable (physically, the temperature of these nodes has to be the closest to the one of the copper panel).

Results and considerations

As emerged in the Table 2.9, the only update of $k_{iso}^{(eq)}$ (iteration 1) is able to satisfy the correlation criterion of both the mean and the standard deviation:

$$M^{(1)} = 0.27^oC < 2^oC \tag{2.11}$$

$$\sigma^{(1)} = 2.3^oC < 5^oC \tag{2.12}$$

Case	Sensor	Error at each Iteration $[^oC]$ 0	1	2	3	4
Cold 1	Battery1	22.2	-1	-0.4	-0.4	-0.3
	Battery2	22.4	-0.8	-0.2	-0.2	-0.1
	Support	-3.6	-4	-3.5	-3.5	-3.1
	Cover	-2.2	-3.2	-2.6	-2.6	-2.1
	Foot1	-10.7	-10.6	-10.5	-10.5	-11
	Foot2	-10.1	-8	-7.9	-7.9	-8.4
Hot 1	Battery1	-2.3	1.4	1.1	1.1	1.2
	Battery2	-2.7	1.8	1.5	1.5	1.6
	Support	2	2.5	1.8	1.8	2.2
	Cover	1.6	2.1	1.8	1.8	1.7
	Foot1	5	5.1	5.2	5.2	5.1
	Foot2	6	6.1	6.2	6.2	6.1
Cold 2	Battery1	20.3	2.2	1.4	0	0
	Battery2	5.3	-0.5	-0.2	0	0
	Support	1.7	-2.2	-1.8	-1.4	-2.1
	Cover	-1	-1.5	-1.1	-0.9	-1.2
	Foot1	-7.4	-7.6	-7.4	-7.6	-7.4
	Foot2	-5.6	-5.8	-5.6	-5.6	-5.6
	Mean	5.31	-0.27	-0.18	-0.23	-0.18
	DevStd	11.58	2.25	1.80	1.70	1.69

Table 2.9: Correlation table: error between experimental and numerical data.

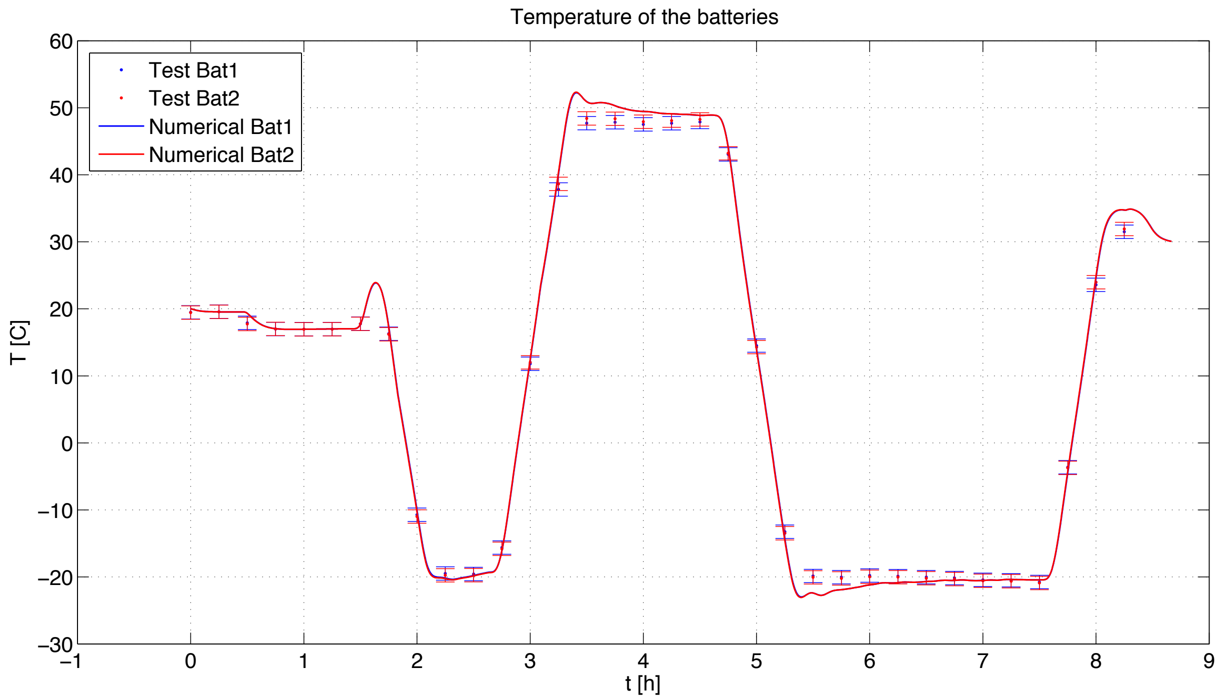

Figure 2.19: Numerical and experimental temperature of the batteries, after correlation.

where the apex (1) indicates the iteration.

The other iterations are just responsible of slight improvements (mean deviation up to 0.18^oC and standard deviation up to 1.69^oC).

It is to emphasize that, after the first iteration, the correlation becomes harder to perform. In fact, the conductive loss is so important that the temperature-regulated panel essentially imposes its temperature to the whole system. So, once updated $k_{iso}^{(eq)}$, the sensibility of the numerical solution to each parameter is extremely low (Section 2.4). Furthermore, the accuracy of the thermocouples is $\pm 1^oC$, so that it is useless and complicate to try to correlate the model below this threshold.

The temperature of the batteries after the correlation is shown in Figure 2.19, and it proves that the model is able to accurately represent the real behaviour of the system.

Then, the heat balance of the **Cold 1** case (i.e., the only one during which heaters are supplied) is shown in Figure 2.20. As anticipated in Section 2.4, the dynamic of the system is dominated by conduction, and, in fact, less than the 2% is dissipated by radiation. Thus, the reduction of the importance of the conductive path will be the drive-line of the design update performed in Section 2.6.

2.6 New design of the battery subsystem

As the actual design of the BAT was not able to fulfil the thermal requirements of the batteries, the following new design solutions were tailored:

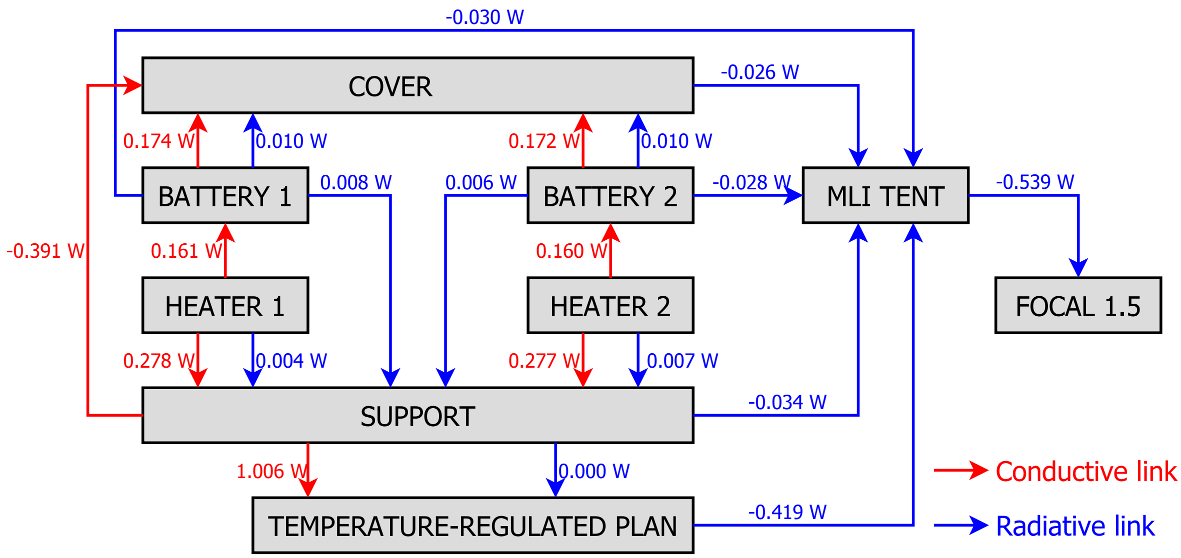

Figure 2.20: Heat balance of the first steady-state.

- to wait that batteries are heated by the sun before charging them. However, this is not possible, because the continuous disconnection and reconnection of the batteries would result in an important failure risk.

- to increase the power of the heaters. Nonetheless, as shown in Figure 2.21 the only introduction of this solution is not efficient. Indeed, it might be integrated with another solution, but a further waste of energy might be critical under the electrical point of view.

- to design a TCS exploiting PCM. The state of the OUFTI-1 project is too advanced for this solution. However, a feasibility study is performed in Section 2.8.

- to improve the insulation of the batteries,

- to insulate the BAT support,

So, the last two solutions appeared to be the best candidates, and they were the subject of several discussions during the year. For these reasons, a subsection is devoted to each one of them.

Then, the decision making process is exploited in the Subsection 2.6.3, where the *Simulink* and the updated *ESATAN* model are opportunely adapted to evaluate the performance of these two solutions.

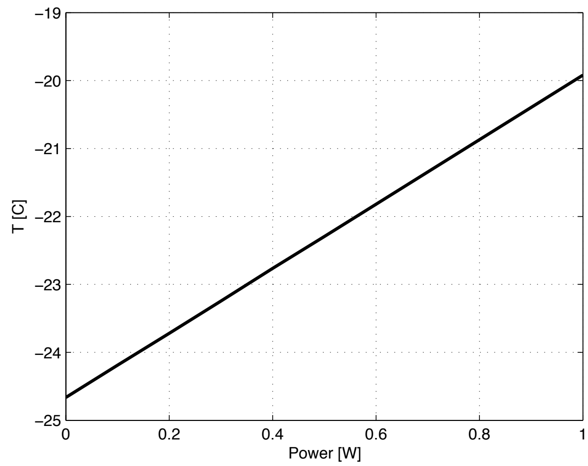

Figure 2.21: Equilibrium temperature of the batteries in function of the total power of the heaters. The temperature imposed to the copper panel is -25^oC. This simulation was obtained with the updated *ESATAN* model.

2.6.1 Isolation of the batteries

The first solution considered is the replacement of the insulator between batteries and support. Delrin and Teflon are commonly exploited as insulators in space applications. The values of their thermal conductivities are [15]:

- $k_{delrin} = 0.221 - 0.3505\frac{W}{m\ K}$
- $k_{teflon} = 0.242 - 0.261\frac{W}{m\ K}$

The order of magnitude of the contact conductances of these materials are shown in Figure 2.22.

In order to consider an optimistic solution[16], the following values are retained for the numerical simulations:

- conductivity of the insulator: $k_{ins} = 0.2\frac{W}{m\ K}$
- contact resistance: $R_c = 200\frac{W}{m^2\ K}$
- thickness: $t_{ins} = 0.5mm$

Furthermore, an optimistic fill ratio of the 10% is considered, too[17]. Nonetheless, as shown in Figure 2.23, this parameter is not responsible of remarkable improvements.

The spacers are in Al6061-T6[18], whose thermal conductivity is $160\frac{W}{m\ K}$ [16].

[16] The most optimistic parameters are considered, since, as discussed in Section 2.6.3, this solution provides extremely pessimistic results.

[17] Indeed, this value is extremely low, and contact between batteries and support might occur because of the strong clamping of the cover. Nonetheless this eventuality is not considered by the numerical model, where the fill ratio can be set as low as desired.

[18] The same material of all the other spacers of OUFTI-1.

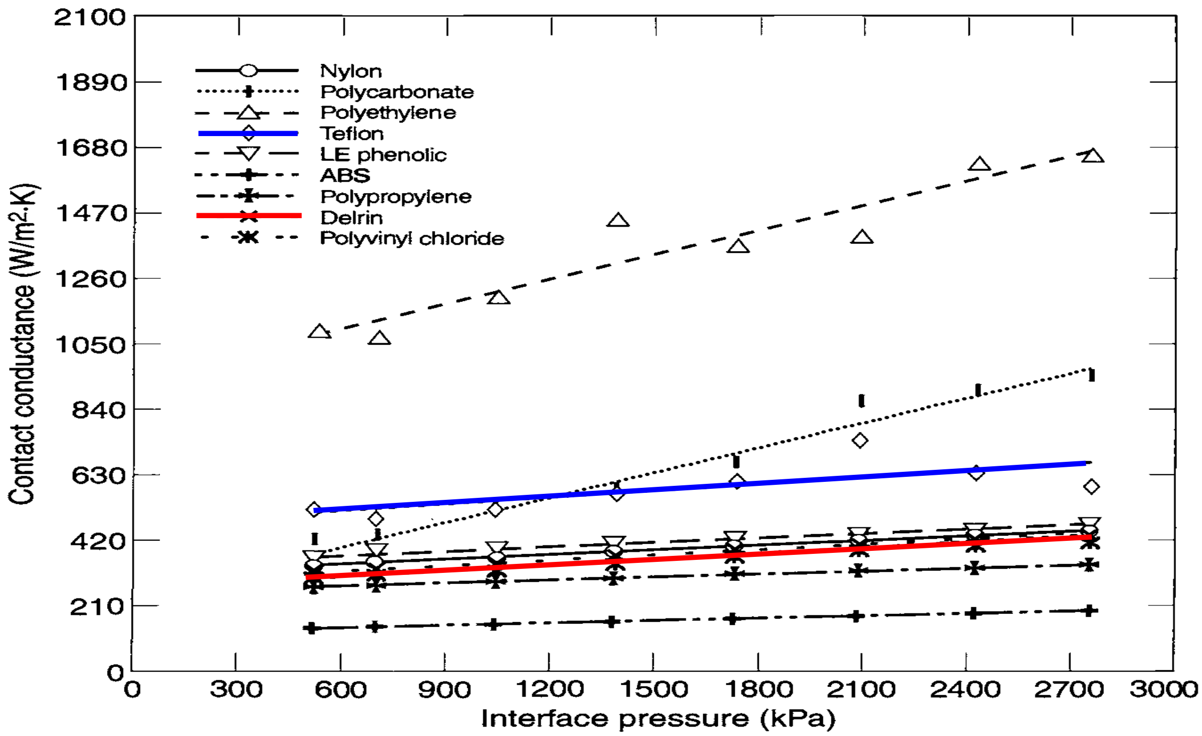

Figure 2.22: Contact heat-transfer coefficient of polymers as a function of apparent interface pressure (from [12]). TEFLON and DELRIN curves are shown in blue and red, respectively.

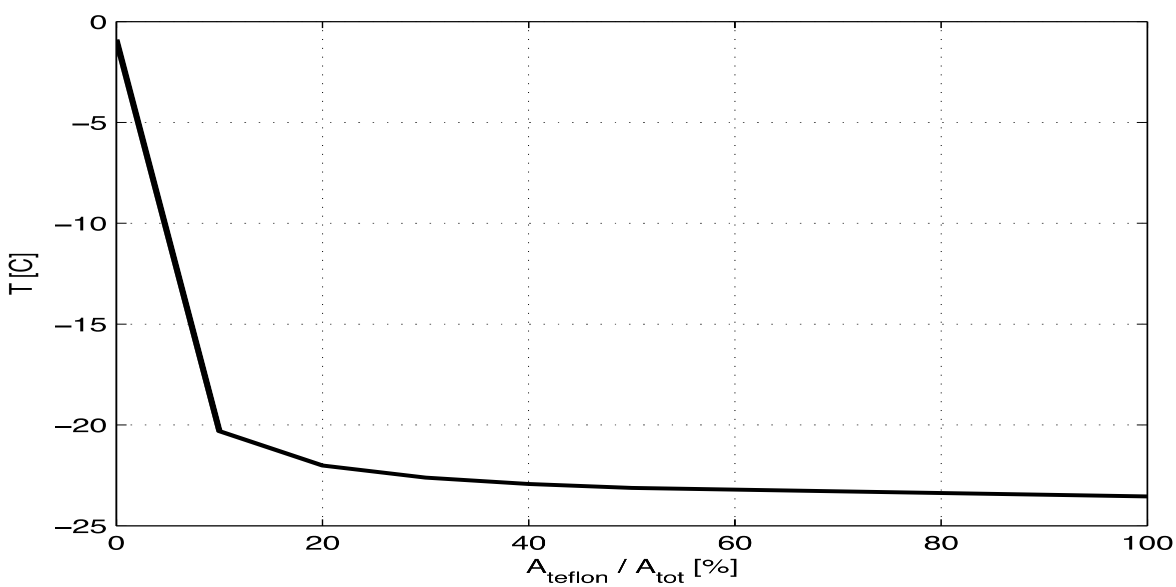

Figure 2.23: Equilibrium temperature of the batteries in function of the fill ratio of the insulator. The temperature imposed to the copper panel is -25^oC. This simulation was obtained with the updated *ESATAN* model.

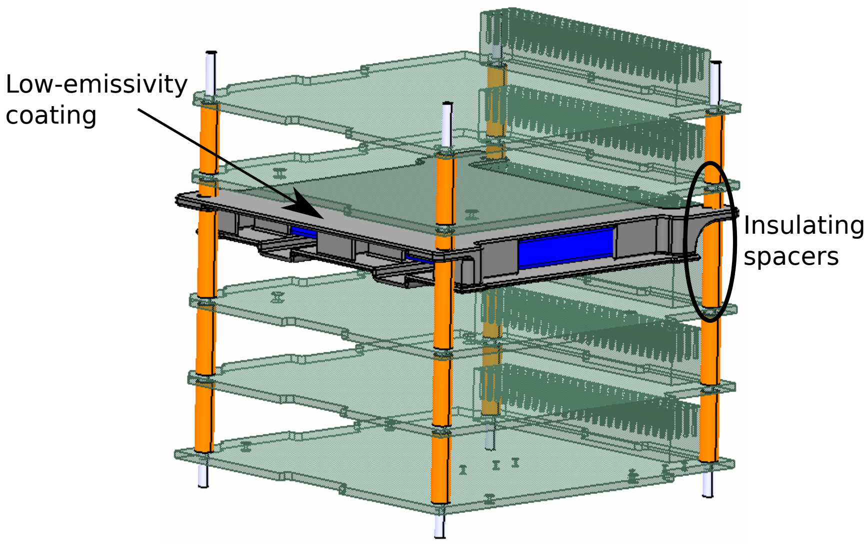

Figure 2.24: Insulation of the support.

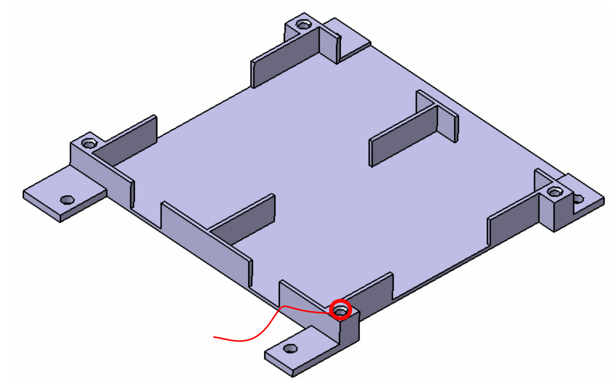

Figure 2.25: Electrical link of the batteries box

2.6.2 Isolation of the support

The other solution considered consists in the insulation of the support box. The isolation has to be both conductive and radiative (Figure 2.24).

Concerning the conductive insulation, it is performed by changing the material of the spacers. This operation has different implications on the satellite:

Electrical: a good thermal insulator is generally a good electrical insulator. For this reason, it is no more possible to perform the connection of the batteries support to the electrical mass by means of the spacers. To fix this problem, the support might be linked to the structure with a conductive wire, fixed on the box through a ring locked by a screw of the cover (Figure 2.25).

Structural: the spacers have to withstand the static and dynamic loads without exceeding the yield stress $\bar{\sigma}$ of the material. For this reason, the material selection is exploited as follow:

- The thermal conductance through a spacer is:

$$GL = \frac{k\ A}{L} \tag{2.13}$$

where k is its thermal conductivity, L its length, and $A = \pi\frac{d_{ext}^2 - d_{int}^2}{4}$ the surface of its cross section. Such conductance has to be minimised.

- The maximum (longitudinal) force, before that plasticity occurs, is[19]:

$$F_{max} = 4\ \bar{\sigma}\ A \tag{2.14}$$

and it has to be bigger than the imposed load.

- by combining the equations 2.14 and 2.13, the conductivity through a spacer is expressed as:

$$GL = \frac{k}{\bar{\sigma}}\ \frac{F_{max}}{4\ L} \tag{2.15}$$

where k and $\bar{\sigma}$ are the only parameters that depend on the material properties.

- So, the spacers material has to maximize the functional $f = \frac{\bar{\sigma}}{k}$. By applying the logarithm (monotonic operator) to this functional, the maximisation curve becomes:

$$\log f = \log\frac{\bar{\sigma}}{k} \Rightarrow \log\bar{\sigma} = \log k + \log f \tag{2.16}$$

The results of this maximisation are shown in Figure 3.2. Furthermore, the material has to respect the requirements of VEGA about the outgassing ($TML \leq 1\%$, $CVCM \leq 0.1\%$), and it cannot be considered hazardous for space applications, so that the choice is limited to:

  - Carbon Fibre Reinforced Polymer (CFRP),
  - Delrin (POM)

The final choice is the Delrin, since this solution is already employed in Swisscube [7], and since the manufacturing of CFRP spacers is far more complex.

The internal diameter of the spacers is fixed to $3.3mm$ (equal to the one of the other conventional Pumpkin spacers), while the external diameter d_{ext} is chosen by imposing that the maximum allowable load is equal to the one of the conventional aluminium spacers (with $d_{ext}^{(Al)} = 4.5mm$):

$$\bar{\sigma}^{(POM)}\ \pi\frac{d_{ext}^2 - d_{int}^2}{4} = \bar{\sigma}^{(Al)}\ \pi\frac{d_{ext}^{(Al)2} - d_{int}^2}{4} \tag{2.17}$$

[19] The coefficient 4 is due to the fact that 4 spacers have to withstand to this force (i.e., the cross section is equivalent to the one of the 4 spacers).

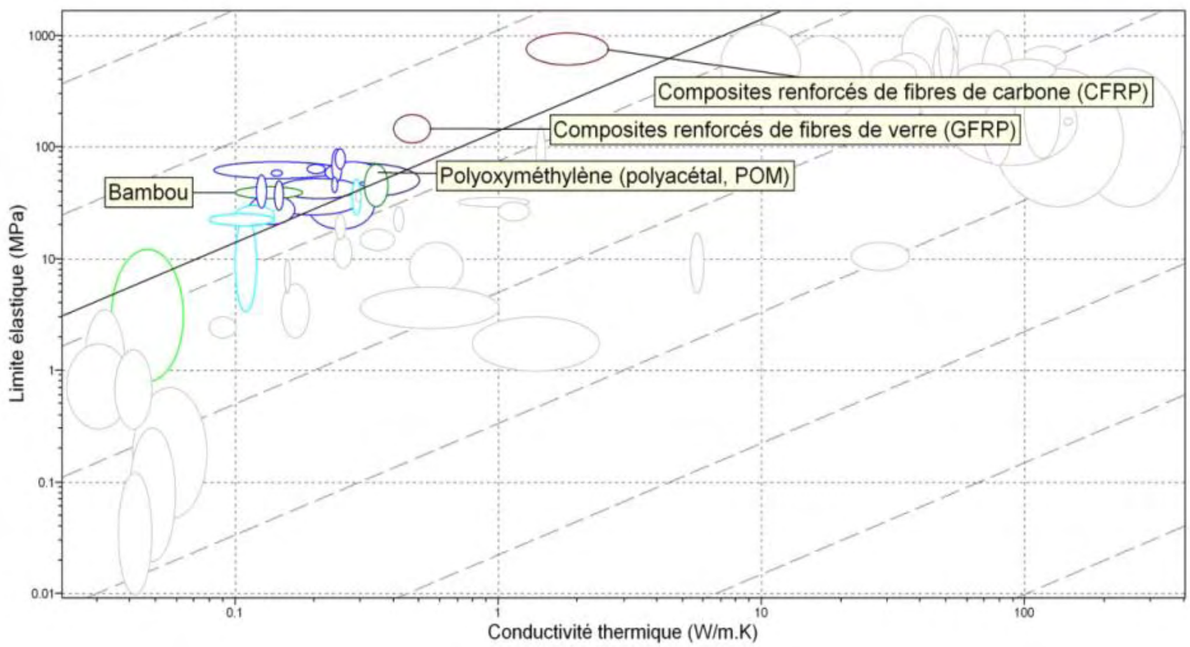

Figure 2.26: Selection of the material of the spacers.

so that[20]:

$$d_{ext} = \sqrt{d_{int}^2 + \frac{\bar{\sigma}^{(Al)}}{\bar{\sigma}^{(POM)}} \left(d_{ext}^{(Al)2} - d_{int}^2 \right)} \simeq 6mm \tag{2.18}$$

A pessimistic value of $0.45 \frac{W}{m\ K}$ is retained for the thermal conductivity of the delrin spacers during the simulations of Section 2.6.3.

On the other hand, the radiative insulation of the support is performed by placing on its external surface with a low-emittance coating. Aluminized mylar film and aluminized adhesive tape are available at the CSL. Their emissivities are of the order of 5% and 10%, respectively. However, the integration of the adhesive tape is easier, and thus it is chosen.

2.6.3 Decision making

To estimate the performance of the proposed solutions, two parameters are exploited:

- the steady-state temperature of the batteries, when a temperature of -20^oC is imposed to the support[21],
- the time constant of the system (see Appendix B for its computation).

In this way, a global indicator of the performance of the design is available, since both the stationary and inertial behaviour of the system are considered.

[20] The bearing yield strength of the Al6061-T6 is $386MPa$ [16], while the one of the Delrin is $125MPa$

[21] This will be the low-temperature limit in the new test procedure discussed in Section 2.7.2

	2 heaters on		**1 heater on**	
	Simulink	ESATAN	Simulink	ESATAN
Isolation of the batteries	-19.3	-18.0	-19.6	-18.9
Isolation of the support	9.6	9.1	-4.8	-0.7

Table 2.10: Performance parameter: steady-state temperature of the batteries. The temperature imposed to the shroud is -20^oC.

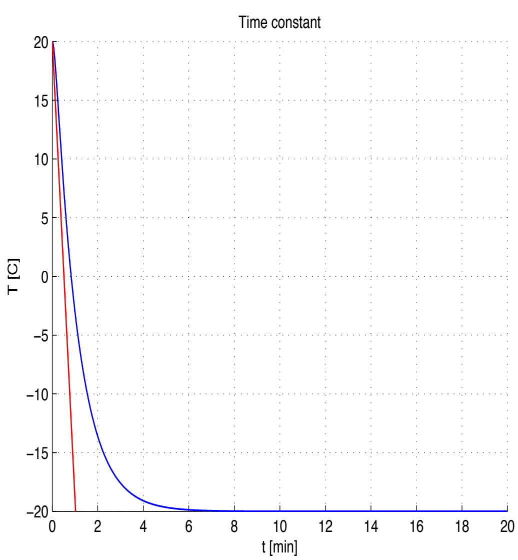

(a) Isolation of the batteries ($\tau = 1'1''$)

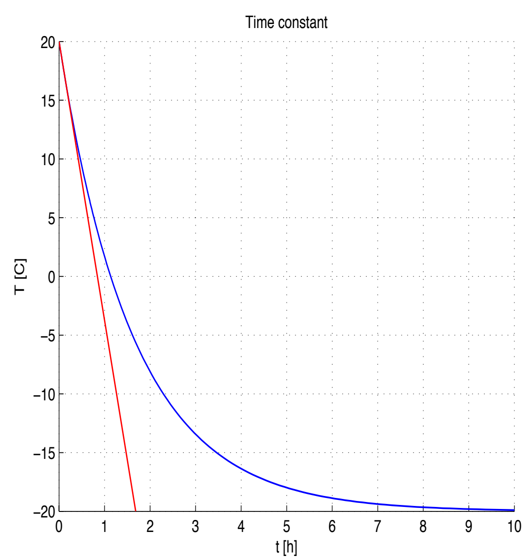

(b) Isolation of the support ($\tau = 1h\ 40'$)

Figure 2.27: Performance parameter: time constant.

	2 heaters on	**1 heater on**
Isolation of the batteries	99.9%	99.9%
Isolation of the support	74.0%	75.8%

Table 2.11: Conductive dissipation trough the spacers (Simulink model), expressed in percentage of the power dissipated by the heaters (i.e., $0.5W$ with both heaters on and $0.25W$ with just one heater on). The temperature of the panel is -20^oC. The radiative dissipation is the complement to 100% of the conductive one.

The value of the performance parameters are shown in Table 2.10 and in Figure 2.27. The superiority of the solution calling for the insulation of the support is overwhelming both under the steady-state and the inertial point of view. Furthermore, as already anticipated in the Subsections 2.6.1 and 2.6.2, the parameters considered for this simulation are pessimistic, while the insulation of the batteries was performed by considering optimistic data.

For these reasons, the retained solution is the insulation of the support. If both heaters are on, this design is also capable to respect the requirement of the batteries in the steady-state conditions. On the other hand, the requirements are not respected with just one heater. However, the time constant is about three time the maximum eclipse duration (i.e., $35'$ see Table 4.3), so that the thermal inertia should be able to prevent the temperature of the batteries from dropping below 0^oC in case of failure. Indeed, the definitive validation of the design requires the fulfilment of a development test (Section 2.7.2).

For sake of completeness, the percentage of power dissipated by conduction and radiation by the two solutions during the steady state is listed in Table 2.11. As already anticipated, in the case of the insulation of the batteries, the temperature gaps are so poor that the only important dissipation mechanism is the conduction.

2.7 Testing

In this Section, the tests on the new design of the BAT subsystem and their procedure are described.

They belong to the class of the *development test*, whose objective is [20]:

> *"to support the design feasibility and to assist in the evolution of the design. Development tests are used to validate new design concepts and the application of proven concepts and techniques to a new configuration."*

For this reason, much freedom is left to the developer in the choice of the technical objective and of the procedure.

At first, it is presented an ambient-condition test aimed at assessing the proper functioning of the thermostat. Then, the procedure for a new vacuum-condition test is detailed. However, this test is scheduled for the 14 of June 2011, so that its results are not available in this dissertation.

2.7.1 Ambient-condition test

The analysis of the results of the test on the BAT subsystem of 2010 (Section 2.3.2) revealed that one of the two series of thermostats closed the circuit when the temperature of its battery was below 0^oC, while the minimum temperature of the set point of these thermostats is 2.8^oC (Figure 2.2(b)). The thermostats are connected in series, so that the close-event is more susceptible to failure than the open one. In fact, the correct functioning of both the elements of the series is necessary to close the circuit correctly. For this reason, it is enough that just one thermostat does not work properly to jeopardize the functioning of the system during the close-event.

So, an ambient-condition test was performed to check if the thermostats work properly (especially in occurrence of the close-event). Furthermore, the functioning of the heaters is tested, too.

Finally, when this test was performed, the design solution calling for the insulation of the support (Section 2.6.2) was not approved yet, so that a secondary objective of this test was to check for the effectiveness of the Teflon exploited as insulator. However, convective exchanges dominate the behaviour of the system, while contact resistances are reduced, because of the presence of the air. For these reasons, this third objective is probably too ambitious for this kind of test, since the response of the system in vacuum conditions depends only on conductive and radiative exchanges.

Test set-up

Ambient-condition tests have the main advantage to be cheaper than vacuum ones. On the other hand, they are not representative of the operational environment of the specimen, since convection dominates the thermal exchanges.

Generally, they are performed by controlling the dew temperature of the air, so that it is lower than the temperature in the chamber at each instant, and condensation does not occur on the specimen. Otherwise, either dry air or dry nitrogen are exploited to prevent this phenomenon. However, this test is aimed at being as cheap as possible, and the first two objectives (i.e., check of the set point of the thermostats and of the proper functioning of the heaters) do not require a fine temperature control and a detailed heat balance determination. For this reason, a conventional freezer is employed to cool batteries.

The instrumentation and the specimen of the test are shown in Figure 2.28, and they are:

Multimeter: two multimeters are exploited to detect the current passing through the heaters. In this way, it is also possible to know when the thermostats close or open the circuit. The full scale is set to $2000A$, since the nominal resistance of the heaters is 26.6Ω, and the input voltage is $3.7V$ (so that the nominal current is about $140mA$).

Thermocouples: the thermocouples exploited [23] are type T (i.e., copper–constantan). Their sensitivity is $43\frac{\mu V}{K}$, and their accuracy is $\pm 0.6K$ (for absolute measures). The

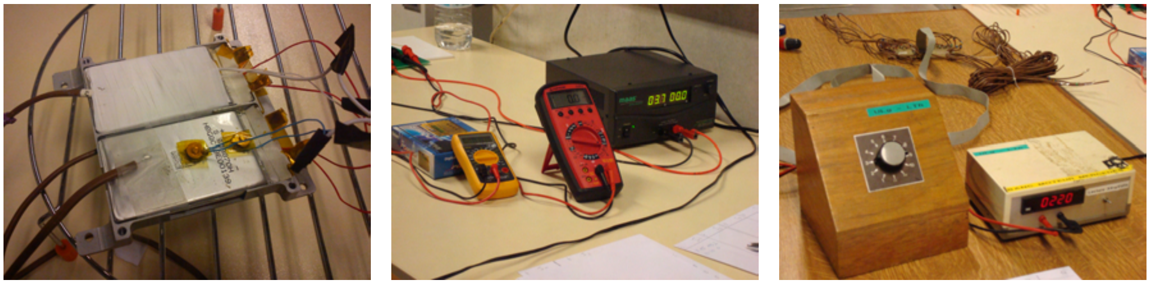

(a) Specimen (b) Multimeter and voltage source (c) Thermocouples and mux

Figure 2.28: Test set-up.

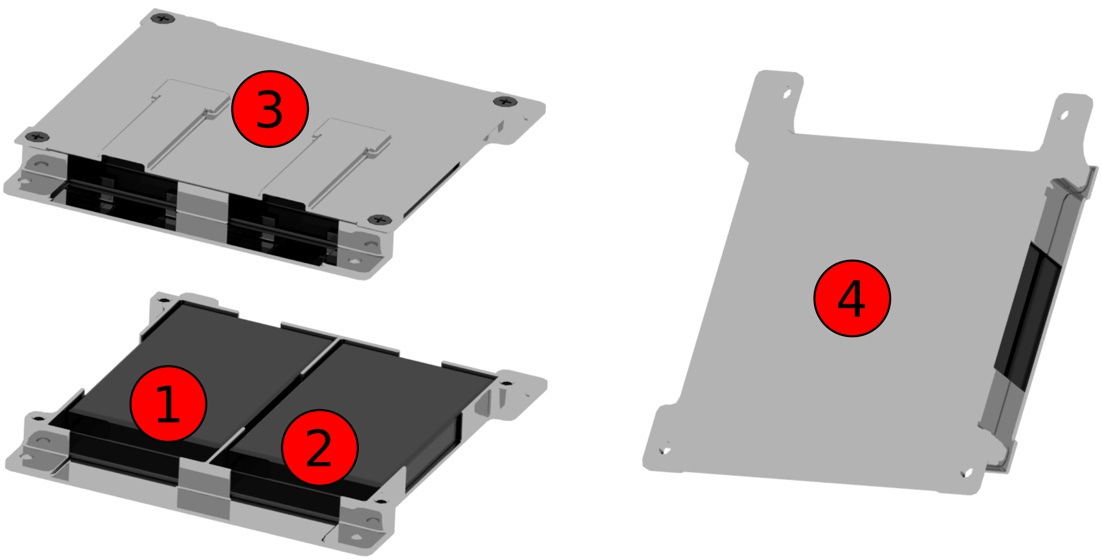

Figure 2.29: Location of the thermocouples on the specimen.

location of the thermocouples on the specimen is shown in Figure 2.29 . One transducer is placed at the top of each battery (i.e., on the side of the thermostats), and one at the center of the support and of the cover. Furthermore, one thermocouple is placed in the freezer and one measures the ambient temperature, so that a total of 6 temperatures are monitored during the test. The reference temperature is 0^oC, and it is measured by another transducer dip into the ice.

Voltage source: it is employed to supply heaters. The output is set to $3.7V$, which is the nominal voltage of the batteries.

Mux: a multiplexer is exploited to read the different signals coming from the thermocouples.

Freezer: as already anticipated, a conventional freezer is exploited to cool batteries. This

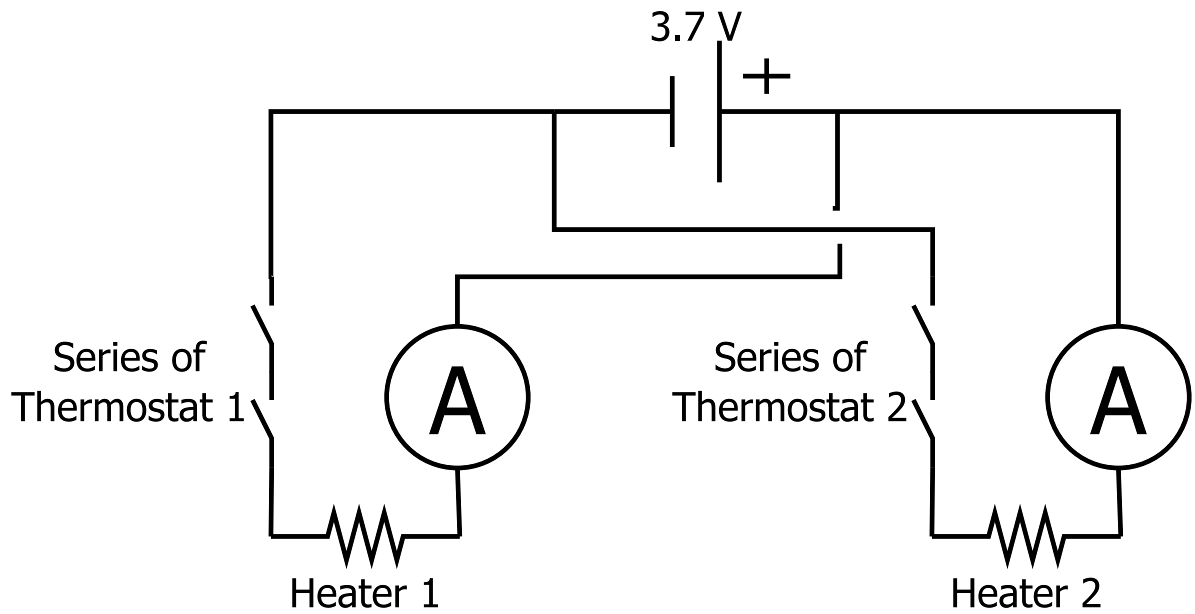

Figure 2.30: Electrical set-up of the test.

solution is extremely cheap, but a fine control of the imposed temperature and of the dew point is not possible.

Specimen: it consists in the integration of batteries, heaters, thermostats, insulator and support. Three layers of Teflon tape wrapping the batteries are exploited as insulator.

The electrical set-up of the test is shown in Figure 2.30. The ammeters are connected in series with the heaters and the thermostats. As already anticipated, an external voltage source is exploited to supply heaters, because of two main reasons:

- the heaters and the thermostats are already integrated on a couple of out of order batteries,
- in this way, the system is supplied by constant voltage, and, thus, constant power. On the contrary, the discharge of the batteries would result in a time-dependent power dissipation.

In conclusion, the physical quantities measured are two currents and six temperatures.

Test procedure

The test consists of two phases:

Cold phase: the specimen is placed in the freezer till the temperature of the batteries drops below 0^oC. During this phase, thermostats should close the circuit to supply heaters.

Hot phase: the specimen is removed from the freezer and heated by means of natural convection till thermostats open the circuit.

The specimen is placed on a grill to reduce the conductive exchange with the environment, so that the transitory is dominated by convection (Figure 2.28(a)).

Three different tests were performed to check for the efficacy of the insulation and the heaters:

1. The two heaters are supplied, but teflon insulator is just placed on the battery 2.

2. Teflon is placed on the two batteries, but the only battery two is supplied.

3. Teflon is only placed on the battery 2, but only heater 1 is supplied.

Furthermore, a preliminary test was performed to check for the right functioning of the set-up. During this test both heaters are supplied, but the temperature is detected only when thermostats close and open the circuit.

In this way, three measures of the set point and the operating temperature of the thermostats of each battery are performed.

Results

The set point and the operational temperature of the thermostats detected during the tests are listed in Table 2.12. All the test results show that thermostats work properly, since they open and close in the uncertainty interval shown in Figure 2.2. For this reason, the anomaly detected in the results of the vacuum-condition test of 2010 is not due to a malfunctioning of the thermostat. So, its most suitable causes are:

1. the thermocouples were not connected properly. However, the results provided by the two sensors on the battery were coherent each others (the maximum discrepancy between them was less than $10^{-3}C$ at each sampling time), so that this explication is not satisfactory;

2. the detected temperatures are not representative of the temperature of the core of the batteries. In fact, the thermocouples were placed on their thickness. For this reason, a thermocouple at the center of the batteries is mandatory for the next vacuum-condition test.

Concerning the heaters, the current detected by the multimeters when the thermostats closed the circuit was $I_1 = 112.6 \pm 1mA$ in the circuit of the first battery, and $I_2 = 124.8 \pm 1mA$ in the second one. The voltage source provides a tension of $V = 3.7V$, so that the power provided to the electrical circuits is:

$$P_1 = V \cdot I_1 = 417mW \tag{2.19}$$

$$P_2 = V \cdot I_2 = 462mW \tag{2.20}$$

	Battery 1		Battery 2	
Test	SP [^oC]	OT [^oC]	SP [^oC]	OT [^oC]
Preliminar	5.6	21.2	4.1	21.2
1	5.6	21.6	3.8	21.5
2	-	-	4.2	21.7
3	5.2	21.4	-	-

Table 2.12: Thermostats experimental set point (SP) and operating temperature (OT).

The nominal resistance of the heaters is 26.3Ω [2], while the effective ones, measured with the ohmmeter are about $R^{(heater)} = 28\Omega$, this resulting in a lower power supplied for a fixed voltage, since $P = \frac{V^2}{R}$. The error respect to the nominal value is about 6.5%, but the datasheet of the heaters states that the incertitude is of $\pm 10\%$ [9].

However, this surplus of resistance is not too critical, since the minimum design power to provide to a battery is fixed to $250mW$ [2], so that the minimum voltage required (by the effective resistance of the heaters) is $2.65V$, which is less than the cut-off voltage of the batteries ($2.7V$).

On the other hand, the global resistance of the circuit is:

$$R_1^{(circ)} = \frac{V}{I_1} = 32.9\Omega \tag{2.21}$$

$$R_2^{(circ)} = \frac{V}{I_2} = 29.6\Omega \tag{2.22}$$

which means that part of the power provided is not dissipated by the heaters, but by the other elements (series of thermostats, cables, ammeter). The wasted power $P^{(w)}$ to total power P ratio is:

$$\frac{P^{(w)}}{P} = 1 - \frac{P^{(heater)}}{P} = 1 - \frac{R^{(heater)}}{R^{(circ)}} \tag{2.23}$$

and it is equal to:

$$\left(\frac{P^{(w)}}{P}\right)_1 = 14.9\% \tag{2.24}$$

$$\left(\frac{P^{(w)}}{P}\right)_2 = 5.4\% \tag{2.25}$$

Finally, the effectiveness of the insulation of the batteries is envisaged. As already anticipated, the ambient-condition behaviour of the system is not representative of the under-vacuum one. Especially, the contact conductance between insulator and support is increased because of the presence of the air. However, this test is not aimed at improving the numerical modelling of the batteries subsystem, but it just wants to provide a preliminary idea of its response.

The evolution of the experimental temperatures in function of time is drawn in Figure 2.31. The cover is always the coldest component during cold cases and the hottest during the hot one. This is mainly due to the fact that the thermocouples on the batteries did not allow to clamp too strongly the support, so that the conductive path between the cover and the other elements is reduced. The temperatures of the two batteries are quite similar each others. Only during the second test, a slight difference between their temperatures rises as battery 2 is heated. However, the maximum gap between the temperature of the two batteries is about 2^oC, while, as previously stated, the incertitude on the signal of the thermocouples is 0.6^oC (and, consequently, the incertitude on the gap is $\sqrt{2} \cdot 0.6^oC = 0.85^oC$). For this reason, as expected, it is not possible to draw optimistic deductions on the effectiveness of the insulator with this test.

In conclusion, this test proved that:

1. the thermostats work properly,
2. the heaters work properly, though their resistance is grater than the nominal one, but this is not too critical,
3. the effectiveness of the insulation of the batteries cannot be proven with this test.

2.7.2 Vacuum-condition test procedure

A new vacuum-condition test has to be performed to validate the new design solution. In this Section, the test procedure is described.

Objectives and procedure

The objectives of this test are the same of the one of 2010, and they are listed in Section 2.3.1. The procedure is analogous to the one described in that Section, too. However some rectifications are made:

- The test facility is no more the *FOCAL 1.5*, but the *FOCAL 0.25* (i.e., $25cm$ of diameter, Figure 2.32), so that the test is much cheaper.
- The temperature limits are settled by exploiting the numerical simulation of the new global model, which takes into account the impact of the new design of the battery support (see Chapter 4 and Figure 4.6). So, the temperature of the batteries is computed to be in the range $[-10, 30]^oC$. A security margin of 10^oC is added (according to [2]), so that the temperature limits are $T_c = -20^oC$ and $T_h = +40^oC$ for the cold and the hot case, respectively.
- Concerning the duration of the cold cases[22], the order of magnitude of the time T_1 necessary to stabilize the solution at 1^oC is provided by equation B.2:

$$1^oC = (T_c - T_h)\ exp\left(-\frac{T_1}{\tau}\right) \qquad (2.26)$$

[22]The duration of the hot case is set to just $30'$ in order to gain time, since the hot case is mainly aimed at re-opening the thermostats.

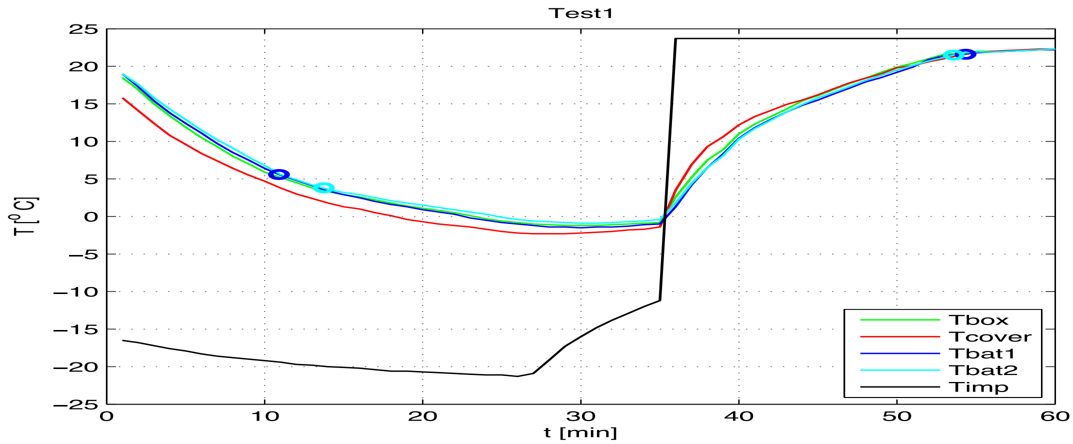

(a) Test 1

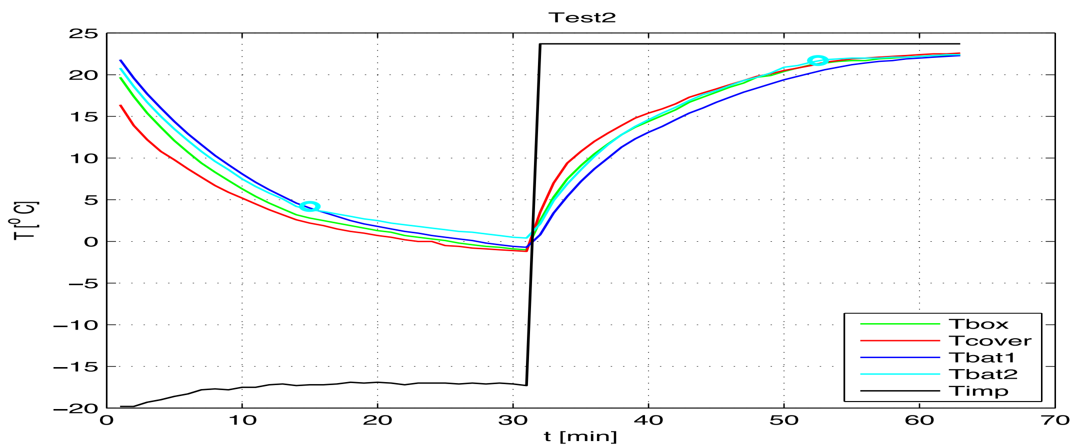

(b) Test 2

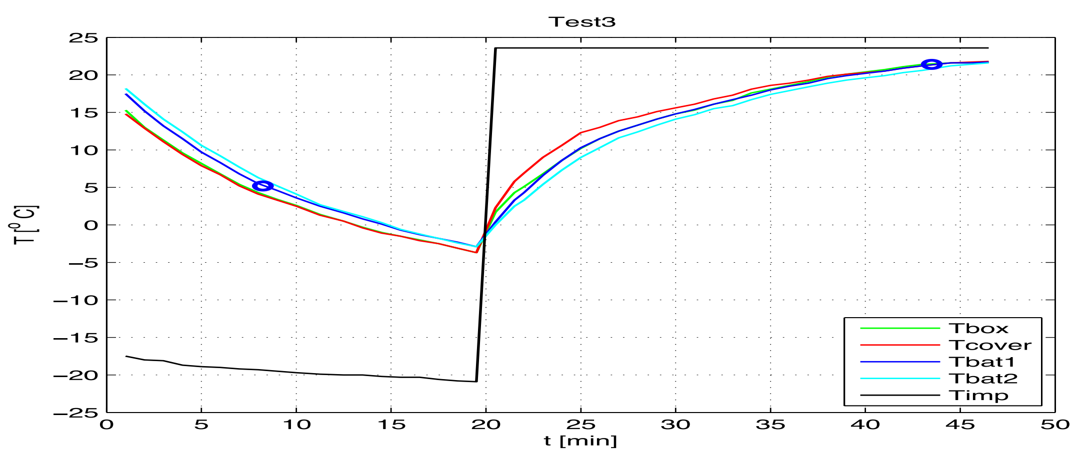

(c) Test 3

Figure 2.31: Experimental temperatures in function of time.

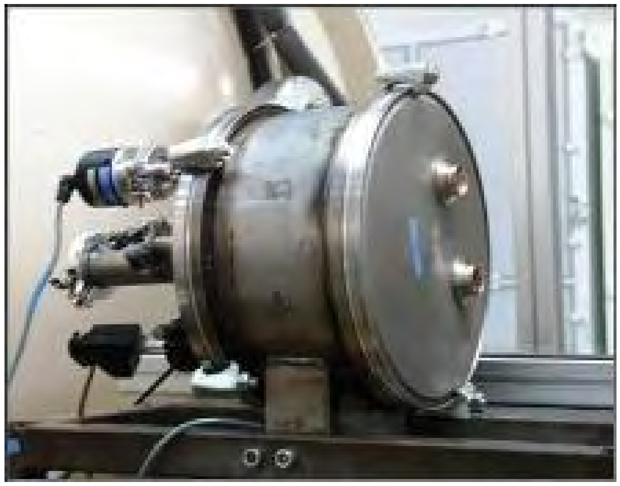

Figure 2.32: *FOCAL 0.25*, the vacuum chamber exploited for the new BAT test, courtesy of CSL [24].

so that:

$$T_1 = \tau \ \ln(T_c - T_h) \simeq 5^h \ 50' \tag{2.27}$$

being $\tau = 1^h \ 40'$ the time constant estimated in Section 2.6.3. However, this period is too long, so that the choice is to renounce to the achievement of a steady state in favour of a reasonable duration of the test. Thus, the period of the cold cycles is set to 2 hours, which is of the same order of magnitude of τ and more than three times the maximum eclipse time (i.e., $35'$).

- The numerical simulation of the test is shown in Figure 2.33 and it consists of:
  - Two hot cases (i.e., $T_{imposed} = 40^oC$). The first hot cycle is performed at the beginning of the test to prevent outgassing, as suggested by [20] and [12]. The second one is aimed at re-opening the thermostats in order to test their functioning twice.
  - Two cold cases (i.e., $T_{imposed} = -20^oC$). In the first case, heaters are supplied by an external voltage source, so that the power provided is constant during time, while, in the second, the batteries supply them (so that the energy consumption can be computed). After the first hour of the first cold cycle, one heater is switched off to simulate a failure. This is performed during the first cold cycle in order to save time; a third cold cycle would be preferred, but, in this way, the test would be too long. As shown in Figure 2.33, the sign of the slope of the curve of the temperature of the batteries should change as both heaters are turned on, which means that the equilibrium temperature of the batteries with both heaters on is grater than the set-up point of the thermostats[23].

[23]The numerical simulations were performed by considering a set-up point of the thermostats of 5^oC, and a dissipated power of $0.25W$ per heater.

Name	IN/OUT	Description
Bat1	IN	Battery 1 and its protection circuit
Bat2	IN	Battery 2 and its protection circuit
H1	IN	Heater 1
H2	IN	Heater 2
TS1	IN	Series of thermostats 1
TS2	IN	Series of thermostats 2
VS	OUT	Voltage source
Vbat	OUT	Voltmeter
I1	OUT	First ammeter
I2	OUT	Second ammeter
Fail	OUT	Switch to simulate a failure
C1/C2	OUT	Switch to choose the power source (VS or batteries)

Table 2.13: Components of the electrical scheme of Figure 2.34, and their location (in or out the *Focal 0.25*).

Integration of the system

The assembly of the BAT subsystem is analogous to the one described in [2], and it is shown in Figure 2.3. However, some changes are made:

- A Kapton film is placed on the temperature-regulated panel, to enhance the radiative exchange ($\epsilon_{Kapton} \simeq 80\%$).
- The electrical set-up is able to simulate the failure of a heater, and to commute the power source from the external voltage source (during the first cold cycle) to the batteries (during the second cold cycle). The electrical scheme is shown in Figure 2.34, and its nomenclature is defined in Table 2.13. The numbers in the red circles represent the electrical nodes implemented on the stripboard, which, differently from the 2010 test, is kept out of the vacuum vessel (*FOCAL 0.25* is much smaller than *FOCAL 1.5*).
- The thermostats are glued on a Kapton adhesive tape. This causes an undesired thermal resistance between batteries and thermostats, but in this way they can easily be removed after the test.

Furthermore, as described in Section 2.6, aluminium adhesive tape will be placed at the exterior of the support of the batteries, in order to reduce the radiative dissipation.

Then, the integration of the specimen on the copper interface is performed by means of four Pumpkin endless screw and eight POM spacers (4 below and 4 above the support), so that the real integration of the BAT system in OUFTI-1 is reproduced at best (Figure 2.35).

Finally, the location of the thermocouples is the same of Figure 2.29, but the thermocouples at the center of the batteries (blue circles in the Figure) are exploited, too.

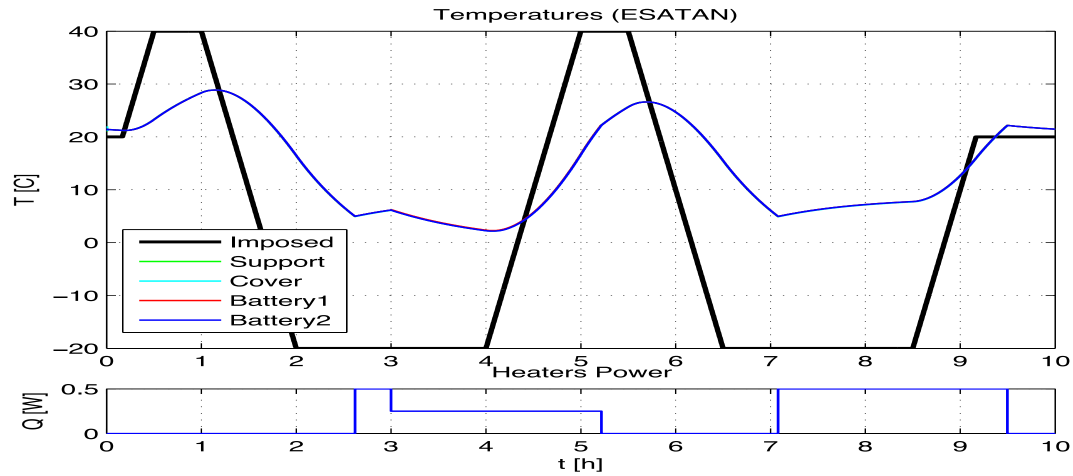

(a) ESATAN model

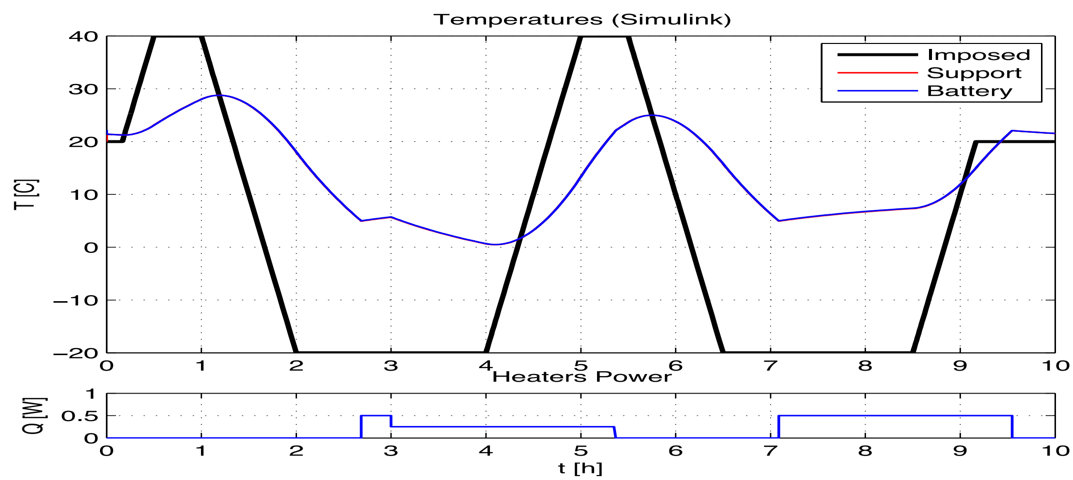

(b) Simulink model (temperature)

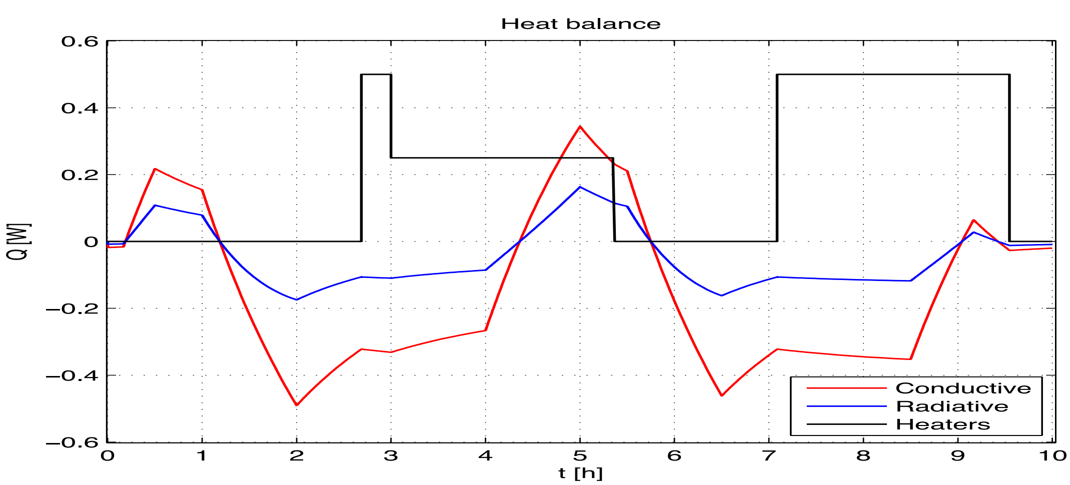

(c) Simulink model (heat balance. Power incoming in the BAT system from the temperature-regulated panel.)

Figure 2.33: Numerical simulation of the test.

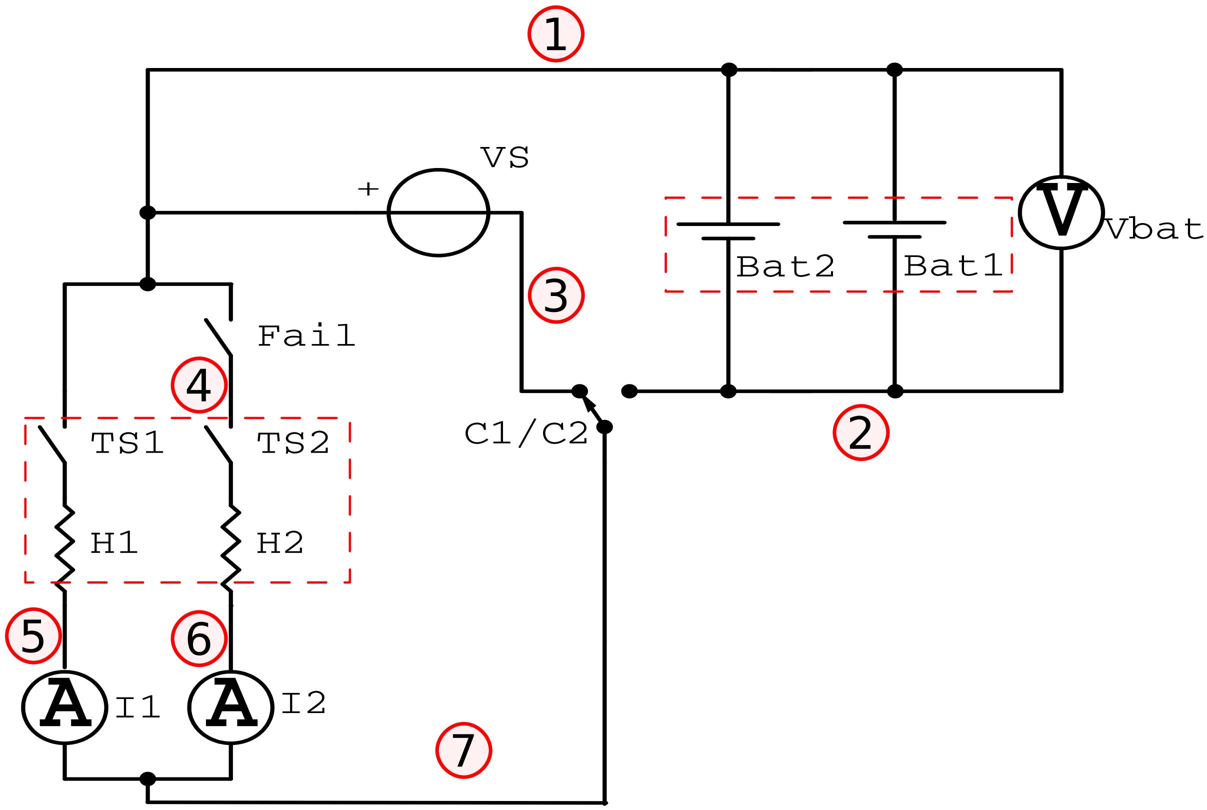

Figure 2.34: Electrical scheme of the test. The red-dashed rectangles represent the elements inside the vacuum vessel. The numbers in red circles are the electrical nodes implemented on the stripboard.

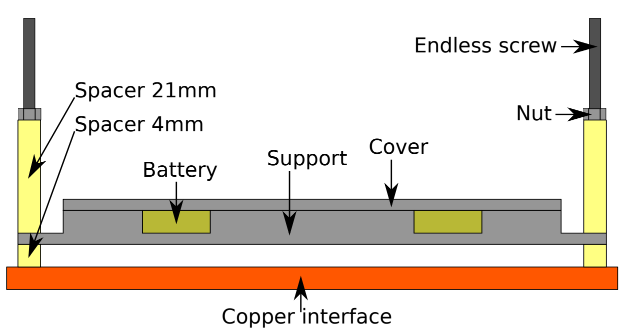

(a) Scheme

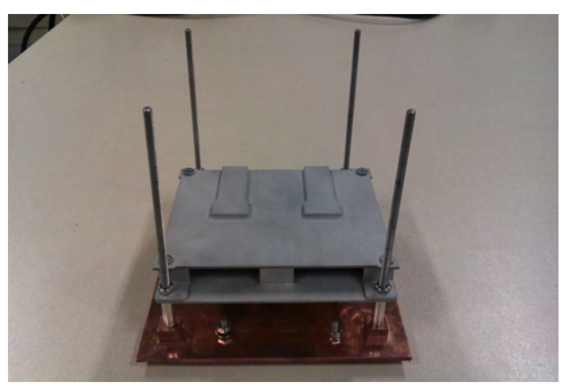

(b) Picture (POM spacers are missing)

Figure 2.35: Integration of the support on the copper interface.

2.8 Feasibility study of a TCS performed with Phase Change Materials

Throughout the various phases of every spacecraft mission, there are significant variations in the temperature level and heat fluxes of some components. This fact is enhanced in the pico and nano-satellites, because of their extremely low inertia. Dissipative devices are thus exploited to keep the temperature of the components in their operational range. Nevertheless, the demand of compensation heating power may become critical for the spacecraft EPS and more particularly on the battery design.

A promising solution to this issue consists in the involvement of PCM, which absorb transient dissipation and thus limit the functioning temperature range.

A PCM is a material having a high heat of fusion, whose change of state (melting and solidifying) at the relevant temperature is able to store and release a large amount of energy: heat is absorbed when the material changes from solid to liquid and vice versa. During this change of state, the temperature remains essentially constant.

So, the employment of the PCM in the TCS of spacecrafts is aimed at:

- reducing the power consumption,
- improving the mass efficiency of the spacecraft itself (i.e., lighter batteries and radiators).

The OUFTI-1 project is already in a phase of design review, so that the introduction of a TCS of the BAT subsystem exploiting PCM is not possible. However, in this Section, a feasibility study of this kind of solution is proposed for three reasons:

- the topic of the PCM is becoming more and more attractive for space applications, where the quest for mass efficiency and power saving is a primary issue,
- in the context of a university project, the research for new and innovative solutions is a priority,
- technological demonstrations represent the 75% of the CubeSats missions [25], so that this kind of solution might be included as a possible payload for other CubeSats.

2.8.1 Problem statement

The TCS based upon PCM belongs to the category of the Thermal Energy Storage (TES) devices. The most exploited physical storage mechanism is the thermal inertia. However, high inertia is necessary associated to high mass. On the contrary PCM are able to store energy by performing a phase change, where large amount of specific energy is necessary.

Because of the very large volumetric changes involved in vaporization and sublimation, consideration of these two phase-change transformations for reversible heat storage is impractical. So, the only phase-change considered in this Section are the liquid-solid ones.

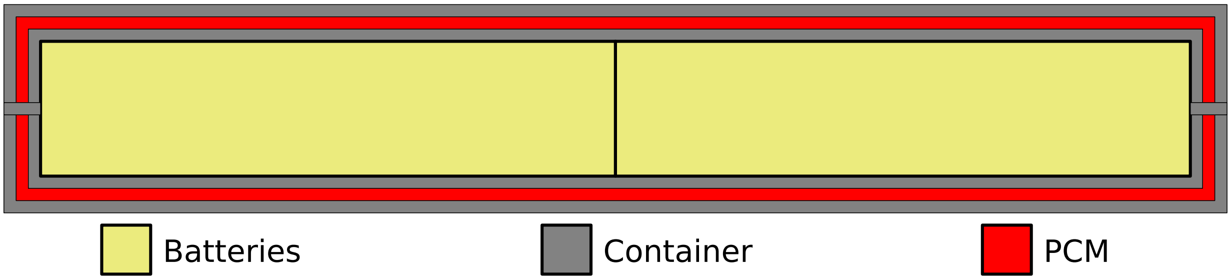

Figure 2.36: Schematic representation of the cross section of the battery support with PCM.

In the BAT issue of OUFTI-1, the necessity is to prevent batteries from experiencing temperature below 0^oC. To this purpose, the idea is to build a new support for the batteries, filled with a PCM, as shown in Figure 2.36. Thus, the support is also exploited as container of the PCM itself.

Concerning the estimation of the performance of the system, the two parameters exploited in Section 2.6.3 (i.e., steady-state temperature and time constant) are no more representative, since there is no more a power source (i.e., when steady-state is reached, the system is isothermal) and the thermal inertia is just a secondary mechanism of storage.

A possible indicator of the performance might be the total storable energy, which is a property of the PCM system. However, this parameter is not completely satisfactory, since the duration of the transition depends by the power exchanged (i.e., the higher the power, the faster the transition).

For this reason, the duration of the transition itself is chosen as best indicator. Indeed, this is not a property of the system, since it depends on external factors (like the temperature imposed and the GL and GR), but it is provides a preliminary description of the response of the system.

In conclusion, the requirement imposed is that the system has to be able to survive to the same conditions of the vacuum test (Section 2.7.2), which means that:

- the minimum duration of the phase transition is $2h$ (which is the same length of time of the cold cycles of the vacuum test, and more than three time the maximum eclipse period),
- the temperature of the copper panel is -20^oC,
- during the transition, the temperature of the batteries must be kept in their operational range (i.e., the melt point must be above the 0^oC).

Since the test conditions are supposed to be more stressing than the in-orbit ones, this requirement is adequate for the design of the system.

2.8.2 Feasibility study

A design procedure for a PCM system is proposed by Gilmore [12]. However, these driveline are valable for the case of the TCS of a component with pulsing power and a radiator toward cold space to dissipate it. On the contrary, in the case in analysis, the aim of the PCM TCS is just to damp the oscillation of temperature, in order to keep batteries temperature in the operational range.

For this reason, the design procedure of [12] was rearranged as follows:

- choice of the PCM,
- establishment of the thermodynamic and heat transfer relations, and sizing of the TCS,
- choice of the container material,
- thermal analysis,
- manufacturing,
- testing.

However, this Section is just aimed at performing a feasibility study, so that the last two points are not discussed.

Choice of the material

The most important parameters of the selection of the PCM are:

- the melting point, T_{melt}. It has to be as close as possible to the average operating temperature of the component, so that *under-cooling* is prevented. Under-cooling means that the temperature of the component drops quickly as phase change is completed. This phenomenon is shown in Figures[24] 2.37(a) and 2.37(b): the lower T_{melt}, the longer is the transition. Indeed, the minimum T_{melt} for the case in exam is 0^oC.
- the heat of fusion per unit of mass, h_f. It has to be as large as possible to minimize weight.

However, the choice of the PCM is generally thread of a complex process of decision making and compromises. Some of the secondary properties that have to be tailored are [12]:

- a good thermal conductivity, in order to have a uniform phase-change transition within the component,

[24] These simulations are performed with the *Simulink* model described in the next paragraph. The heat of fusion is set to $100\frac{kJ}{kg}$.

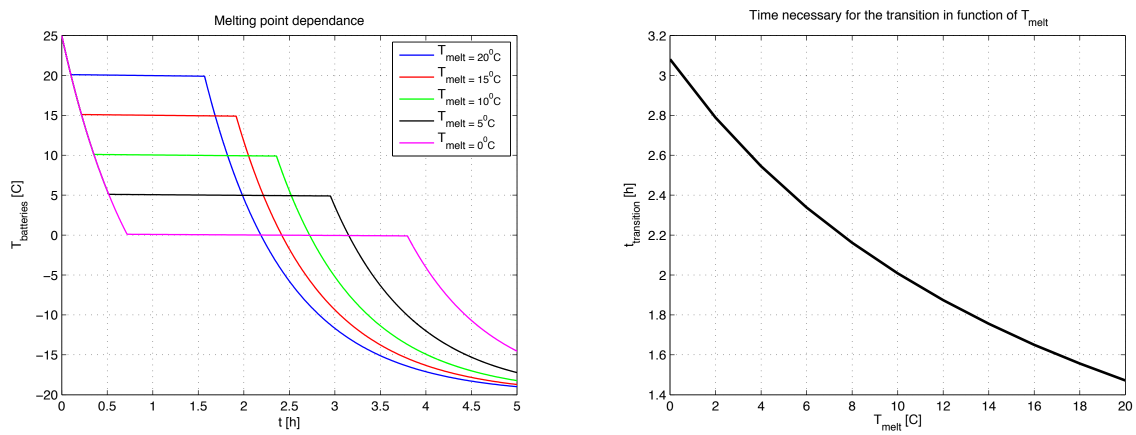

(a) Temperature of the batteries (b) Time of transition

Figure 2.37: Importance of the melting point on the under-cooling phenomenon.

- high density to reduce the size of the container,
- moderate volume change during the transformation,
- a reversible melting and freezing behaviour,
- compatibility with the container material,
- non toxicity,
- low cost, availability, and well documented property data, if possible.

Nonetheless, those data require a detailed experimental analysis and characterisation of the materials in exam, which is not easily available in literature. Furthermore, Gilmore [12] states:

> *"If more than one PCM is found with suitable melting-point temperatures, comparisons of other characteristics should be made to eliminate all but the best PCM."*

So, by considering the Table C.1 of the Appendix C, the only suitable PCM for the case in exam, whose T_{melt} is close to the 0^oC, is the *n-Tetradecane* ($C_{14}H_{30}$). The secondary properties are not considered in this work. The properties available for this material are listed in Table 2.14.

Thermodynamic and heat transfer relations

In this paragraph, a zero-dimensional approach of the problem is proposed. This approach is based upon thermodynamic and heat transfer considerations, and it allows to estimate a preliminary value of the mass of PCM to employ.

Property	Value General	Value Liquid	Value Solid	Reference
Melting point $[^oC]$	6	-	-	[12]
	5.9	-	-	[26]
	5.5	-	-	[27]
Heat of fusion $\left[\frac{kJ}{kg}\right]$	228	-	-	[12]
	227.2	-	-	[27]
Specific heat $\left[\frac{J}{kg\ K}\right]$	-	2100	1800	[28]
Thermal conductivity $\left[\frac{W}{m\ K}\right]$	0.1363	-	-	[26]
	-	0.211	0.273	[28]
Density $\left[\frac{kg}{m^3}\right]$	763	-	-	[26]
	762	-	-	[27]
	-	765	803	[28]

Table 2.14: Properties of the *n-Tetradecane*.

The total energy stored during the phase-change transition by a PCM with mass m and heat of fusion h_f is:

$$E_t = m\ h_f = \int_0^{t_{melt}} P(t)\ dt \tag{2.28}$$

where $P(t)$ is the power absorbed by the PCM, and t_{melt} the duration of the transition.

During the vacuum test, the power incoming in the BAT subsystem is due to:

- conduction through spacers:

$$GL_{sp} = \frac{k_{sp}\ A_{sp}}{L_{sp}} \tag{2.29}$$

  where k_{sp} is the thermal conductivity of the spacers, A_{sp} their cross section and L_{sp} their lenght,

- radiation between support and temperature-regulated panel

$$GR_{panel} \simeq \sigma\ \epsilon_c\ \epsilon_{support}\ A \tag{2.30}$$

  where ϵ_c and $\epsilon_{support}$ are the emittance of the copper and of the support, respectively, $\sigma = 5.67 \cdot 10^{-8} \frac{W}{m^2\ K^4}$ is the Boltzmann constant, $A = 90 \times 75 mm^2$ the surface of the base of the support, and a view factor equal to 1 is supposed.

The phase-change is essentially isothermal[25], and it occurs at the melting point T_{melt}. So, by supposing that the process is homothermal (i.e., the temperature of the PCM is uniform in space), the power incoming in the BAT subsystem during the transition is:

$$P = GL_{sp}\left(T_{panel} - T_{melt}\right) + GR_{panel}\left(T^4_{panel} - T^4_{melt}\right) \tag{2.31}$$

[25]For sake of clarity, most of the PCM exhibit a phase-transition which is not rigorously isothermal.

where $T_{panel} = -20^oC$ is the constant temperature of the copper panel.

By substituting the Equation 2.31 in 2.28, and by considering that the function to be integrated is constant:

$$E_t = m\ h_f = \left[GL_{sp}\left(T_{panel} - T_{melt}\right) + GR_{panel}\left(T^4_{panel} - T^4_{melt}\right)\right] t_{melt} \tag{2.32}$$

So that, for a given PCM (i.e., h_f, T_{melt}) and fixed the boundary conditions (i.e., T_{panel}), the mass of PCM in function of the desired duration of the transition is:

$$m\left(t_{melt}\right) = \frac{GL_{sp}\left(T_{panel} - T_{melt}\right) + GR_{panel}\left(T^4_{panel} - T^4_{melt}\right)}{h_f}\ t_{melt} \tag{2.33}$$

As already anticipated, to minimize the mass, T_{melt} has to be as close as possible to the imposed temperature, and the heat of fusion has to be large. Furthermore, conduction through spacers has to be minimised, too, so that POM spacers are considered (Section 2.6.2).

By substituting the data of Table[26] 2.14 in Equation 2.33, and by imposing a t_{melt} equal to 2 hours, the mass of PCM necessary is equal to 18 g.

Choice of the material of the container

Concerning the selection of the material of the container, Gilmore [12] states:

> *"In selecting container and filler materials, the engineer must consider their thermal and mechanical properties as well as the compatibility of PCM materials with their containers. [...] Three metals are currently used for PCM containers: aluminum, titanium, and stainless steel. They have high strength-to-mass ratios and are corrosion-resistant."*

The most important thermal property of the container is the thermal conductivity. In fact, most of the PCM are bad conductors, so that the container has to prevent high temperature gradients, and to grant that the phase change occurs as homogeneously as possible in the material. The importance of this parameter is emphasized in the numerical simulations of next paragraph.

Because of its low density, resistance to corrosion, and high thermal conductivity, Aluminium is the most exploited material for PCM containers. As it is compatible also with Alkanes [12], it is chosen as container material for the case in analysis.

Thermal analysis

Two numerical models are implemented to study the behaviour of the system. The first one is a lumped-parameters model developed with *Simulink*. The second one is built with *COMSOL* and it is aimed at providing numerical informations about the evolution of the phase-change.

[26] If more than one value is available, they are averaged.

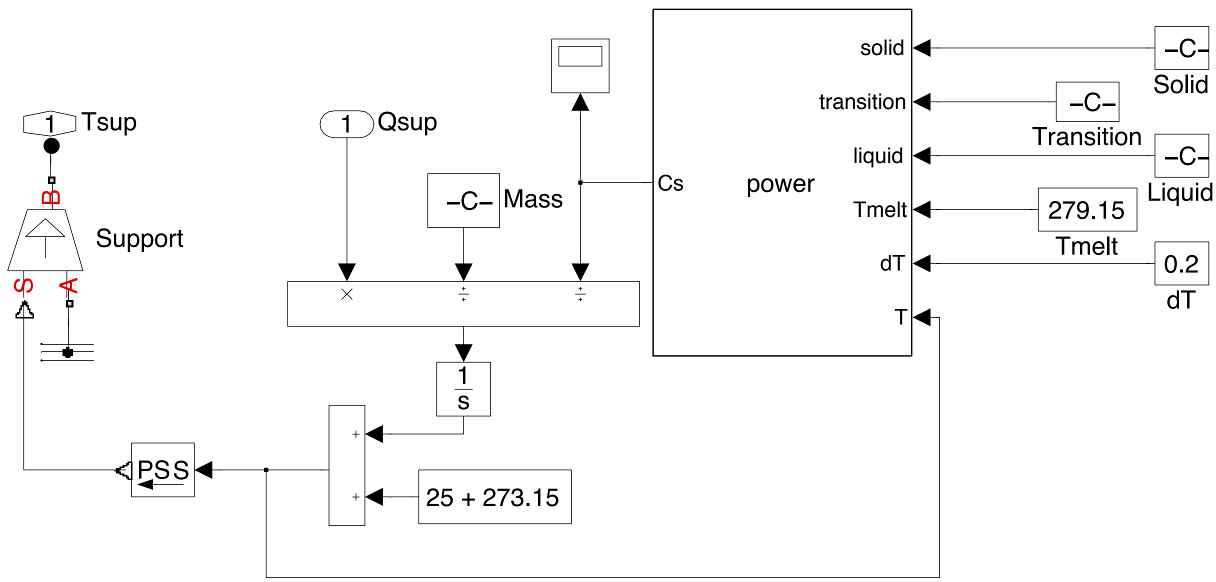

Figure 2.38: Scheme of the PCM block of the *Simulink* model.

The *Simulink* model is analogous to the one described in Section 2.2.2. However, the thermal node of the support is replaced by the block shown in Figure 2.38. This block receives in input the net power, Q, incoming in the support (i.e., power exchanged with batteries and temperature-regulated panel) and computes the temperature of the support itself, T_s.

To this purpose, it is introduced the hypothesis that the thermal inertia of the container is negligible, so that all the power incoming is absorbed by the PCM. In this way, the energy-balance of the support is:

$$m_s \; C_p(T_s) \; \frac{d \; T_s}{dt} = Q \tag{2.34}$$

where m_s is the mass of the PCM and $C_p(T_s)$ its specific heat.

However, the equation 2.34 cannot be exploited when phase-change occurs, since the specific heat is not defined. To overcome this issue in the numerical model, a transition zone of half-width ΔT is defined. This means that the transition occurs in a range of temperature between $T_{melt} - \Delta T$ and $T_{melt} + \Delta T$. In this range, the heat absorbed by the PCM has to be equal to the heat of fusion, so that the specific heat of transition, $C_p^{(t)}$, is defined as:

$$C_p^{(t)} : / \quad \int_{T_{melt}-\Delta T}^{T_{melt}+\Delta T} C_p^{(t)} \; dT \equiv H_f \tag{2.35}$$

so that, by hypothesizing that $C_p^{(t)}$ is constant, the *numerical specific heat* in function of the temperature is:

$$C_p(T) = \begin{cases} C_p^{(s)} & if\ T \leq T_{melt} - \Delta T \\ \frac{H_f}{2\ \Delta T} & if\ T_{melt} - \Delta T < T < T_{melt} + \Delta T \\ C_p^{(l)} & if\ T \geq T_{melt} + \Delta T \end{cases} \tag{2.36}$$

However, with this definition, the specific heat is characterized by two zero-order discontinuities. To avoid this problem, [29] proposes the employment of a gaussian distribution[27]:

$$\delta(T) = \frac{exp\left(-\frac{(T-T_{melt})^2}{\Delta T^2}\right)}{\Delta T\ \sqrt{\pi}} \tag{2.37}$$

which modulates H_f in the definition of the specific heat:

$$C_p(T) = \chi C_p^{(l)} + (1-\chi)C_p^{(s)} + \delta H_f \tag{2.38}$$

where $\chi(T)$ is the liquid fraction defined as:

$$\chi(T) = \begin{cases} 0 & if\ T \leq T_{melt} - \Delta T \\ \frac{1}{2} + \frac{T-T_{melt}}{\Delta T} & if\ T_{melt} - \Delta T < T < T_{melt} + \Delta T \\ 1 & if\ T \geq T_{melt} + \Delta T \end{cases} \tag{2.39}$$

The drawback of this technique is that ΔT has to be as low as possible to well represent the real behaviour of the phase-change (Figure 2.39, the transition is isothermal if $\Delta T \to 0$), but the smaller ΔT, the shorter must be the integration time step, since it has to be able to detect with accuracy the small variations of temperature occurring during the transition. However, this problem is fixed by exploiting a numerical scheme with adaptive step, as Runge-Kutta 15 (**ode15s** in *MATLAB*, suitable for stiff problems).

The temperature of the batteries and of the support in function of time is shown in Figure 2.40 (the temperature imposed to the copper panel is a step from 25 to -20^oC). The transition zone width is set to $\Delta T = 0.05^oC$. As required by the specification imposed in Section 2.8.1, the quantity of PCM estimated in the previous Paragraph is enough to have a duration of the transition of two hours.

Concerning the *COMSOL* model, it is implemented in order to analyse the dynamic behaviour of the phase change and to assess the importance of the thermal conduction of the container. The geometry of the model, shown in Figure 2.41, is bi-dimensional, so that temperature gradients through the thickness of the support are neglected. The geometry is quite simplified, and the only PCM domain is modelled, but it is enough for the purpose of a feasibility study.

The same definitions of Equations 2.38 and 2.39 are exploited, but here they assume the role of local properties.

[27] It is to emphasize that $\int_{-\infty}^{+\infty} \delta = 1$, so that the conservation of energy is preserved.

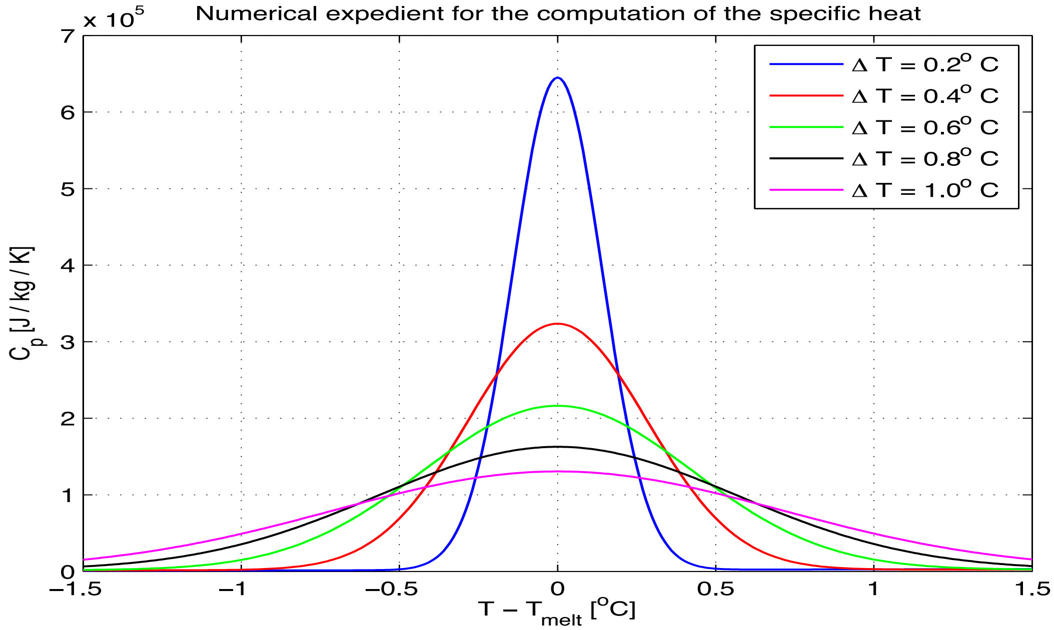

Figure 2.39: Specific heat in function of $(T - T_{melt})$ and of the transition zone width. The lower ΔT, the more accurately an isothermal transition is represented.

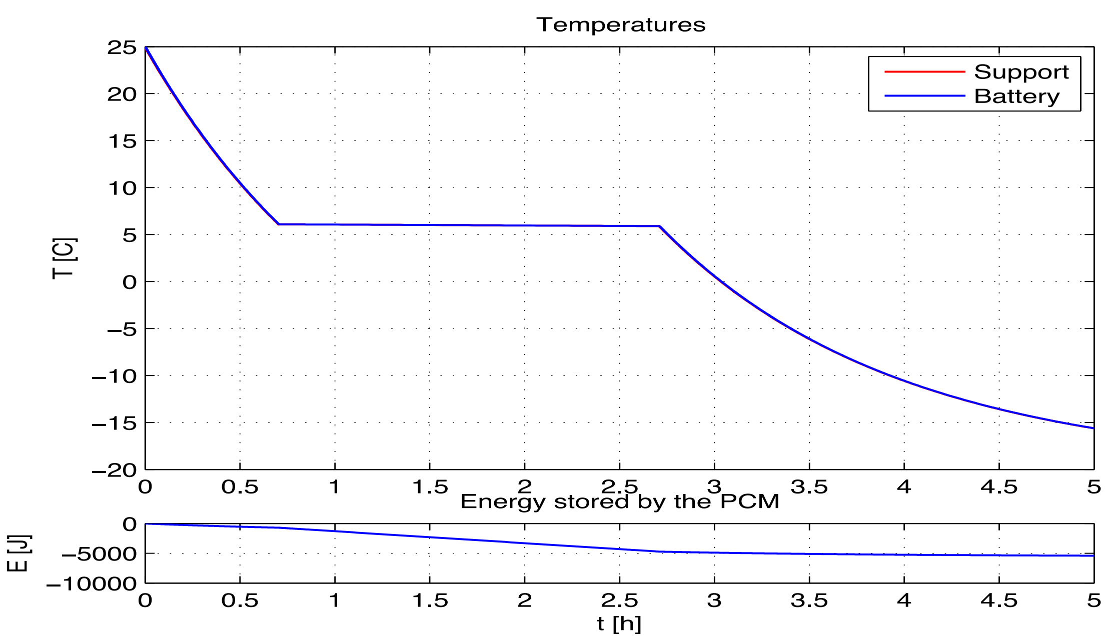

Figure 2.40: Simulation of the phase-transition obtained with the *Simulink*-0D model. The temperature imposed to the copper panel is a step from 25 to -20^oC.

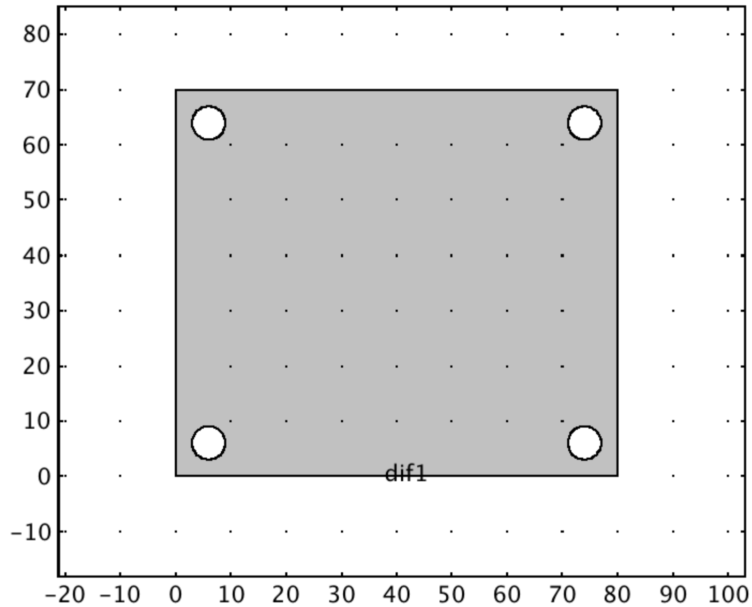

Figure 2.41: Geometry of the *COMSOL* model. Dimensions are in $[mm]$.

The thickness of the PCM is just 2 mm[28], so that heat conduction is supposed to occur only through the container, because of the poor conductivity of the PCM itself [12]. For this reason, two container materials are envisaged. The first one is the aluminium ($k_{Al} = 160 \frac{W}{m\ K}$), while the second one is a fictious bad conductor, whose thermal conductivity is supposed to be equal to $1 \frac{W}{m\ K}$.

In these simulation, the transition width is set to 0.05^oC, too. In this model, not only the time step, but also the refinement of the grid has to be improved in function of this parameter.

The evolution of the global liquid fraction in function of time is shown in Figure 2.42. In the case of the conductive container, the transition is completed in about 2 h, as desired, while in the other case it takes more time. However, this is not positive, since important temperature gradients are present. In fact, the heat is not evacuated by solidifying the PCM, but by cooling the fraction of liquid, as shown in Figure 2.44, and the transition occurs in a reduced volume. On the contrary, in the case of the aluminium container (Figure 2.43), the transition involves most of the domain and the temperature is essentially constant both in time and in space.

2.8.3 Conclusions

The mass of PCM estimated is $18g$, which is of the same order of magnitude of the actual support (46 g [17]), so that, by supposing that the container is at least as heavy as the

[28]It is estimated by knowing the mass and the density of the PCM and the front sizes of the container.

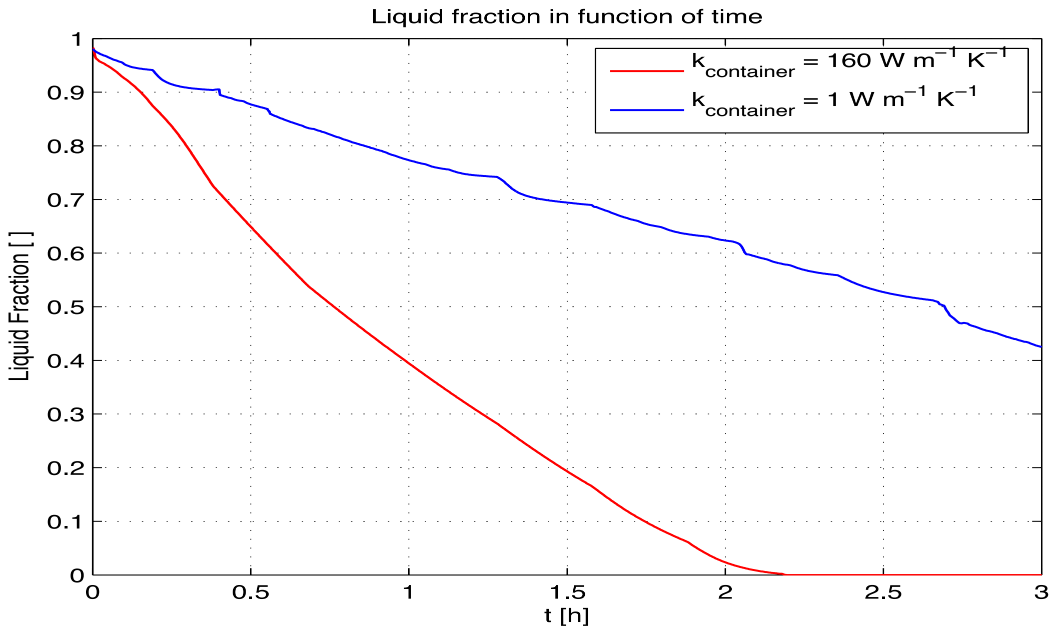

Figure 2.42: Global liquid fraction in function of time, obtained with the *COMSOL* model.

actual support, the solution of the PCM is not convenient under the mass-efficiency point of view. However, this TCS does not require any electrical power dissipation, so that it is power-saving, and, thus, it might allow to under-size the batteries.

However, several details were not considered in this study, for example:

- three-dimensional effects,
- contact resistance between PCM and container,
- density variations throughout the phase-change, which require a "dead volume" when the PCM is in solid state
- long term stability of the PCM

In conclusion, though this solution might be not optimal for a CubeSat, it is feasible, and it shows several positive aspects. However, it deserves to be studied in more detail. Indeed, this topic represents an active research field, and no Commercial Off The Self (COTS) are available, but, as previously stated, technological demonstrations are the main missions of the CubeSat, so that this solution might be included as a payload for a future CubeSat.

Summary

The BAT problem represents the most important thermal issue of the CubeSat, and, thus, the largest part of this work was devoted to it.

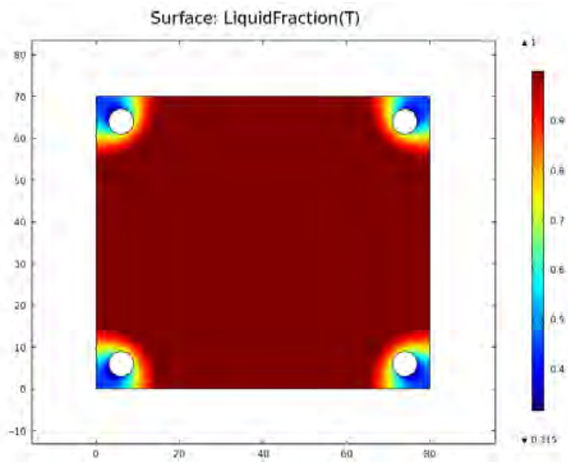

(a) Liquid fraction, t = 100 s

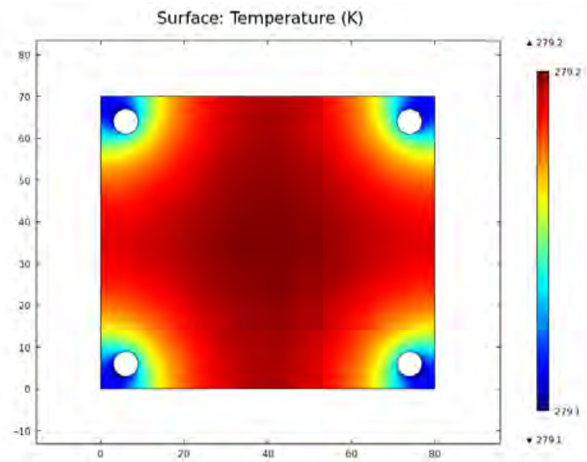

(b) $T \in (279.1, 279.2)K$, t = 100 s

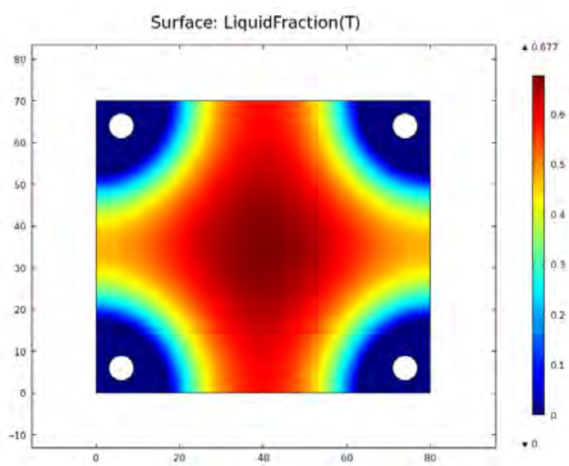

(c) Liquid fraction, t = 3600 s

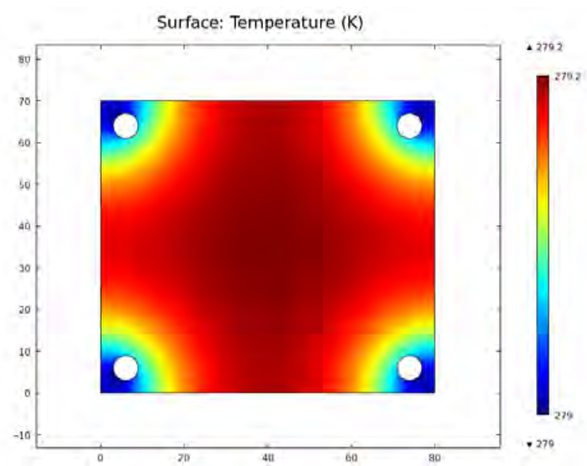

(d) $T \in (279.0, 279.2)K$, t = 3600 s

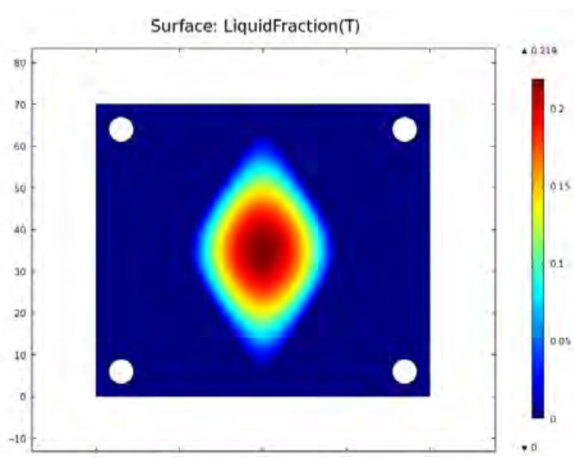

(e) Liquid fraction, t = 7200 s

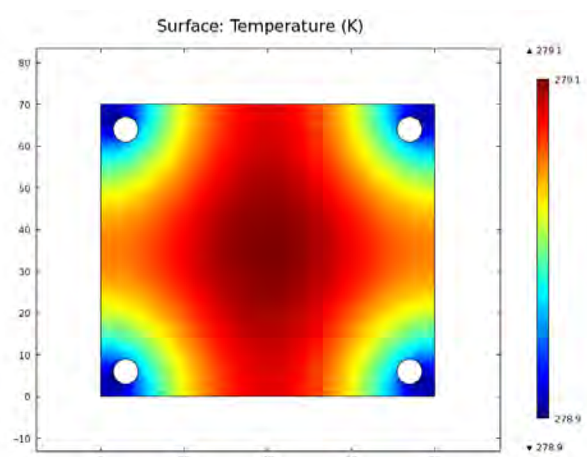

(f) $T \in (278.9, 279.1)K$, t = 7200 s

Figure 2.43: Evolution of the phase change transition at different time steps. Liquid fraction (left) and temperature distribution (right). The container is a good conductor.

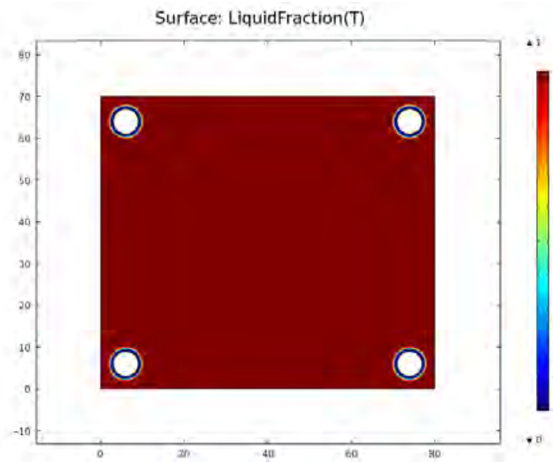

(a) Liquid fraction, t = 100 s

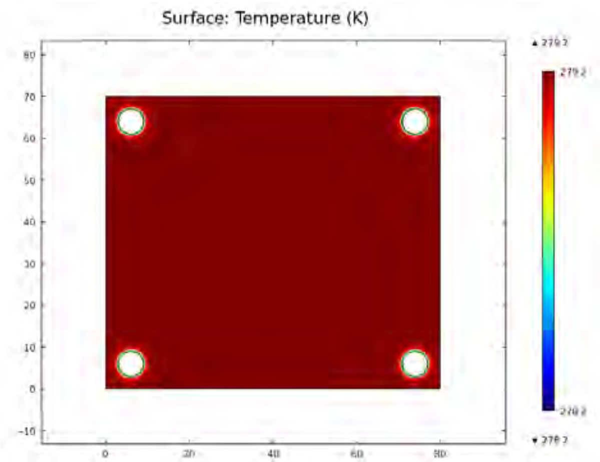

(b) $T \in (278.2, 279.2)K$, t = 100 s

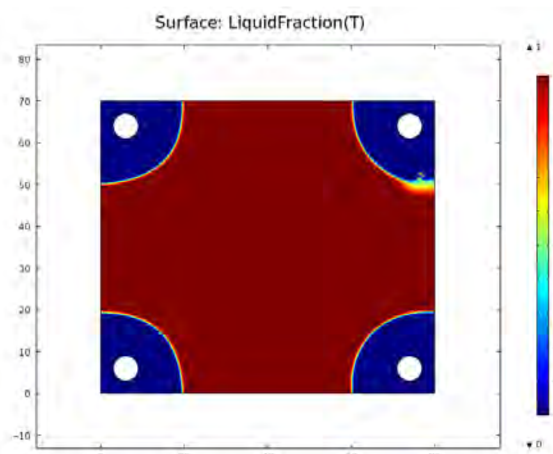

(c) Liquid fraction, t = 3600 s

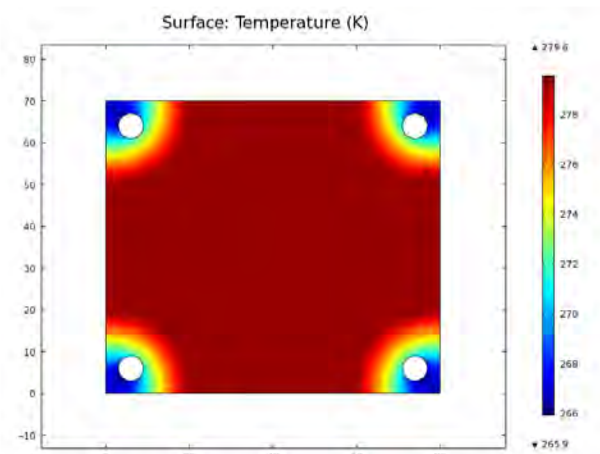

(d) $T \in (268.0, 279.2)K$, t = 3600 s

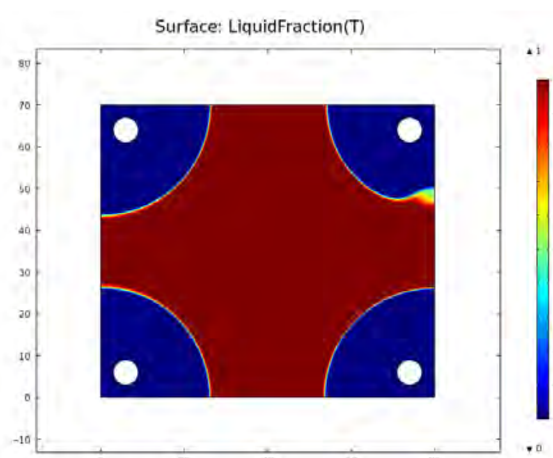

(e) Liquid fraction, t = 7200 s

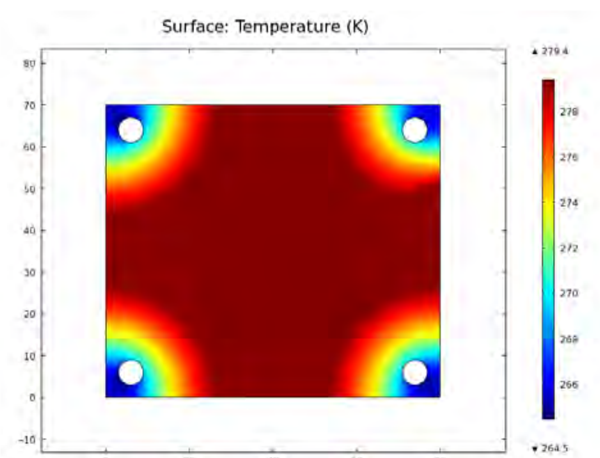

(f) $T \in (264.0, 279.2)K$, t = 7200 s

Figure 2.44: Evolution of the phase change transition at different time steps. Liquid fraction (left) and temperature distribution (right). The container is a bad conductor.

After a detailed description of the actual state of the system, the results of the vacuum test performed in 2009-2010 were analysed, and they revealed that the design was not able to solve the issue.

So, new design solutions were envisaged, and the most suitable appeared to be the one calling for the insulation of the support rather than the batteries.

A new vacuum test, scheduled for the 14 of June, is aimed at proving that this new solution is capable to keep the temperature of the batteries in their operational range.

Chapter 3

Transistor issue

The electrical power generated by the solar cells might exceed the instantaneous power demand of the spacecraft. For this reason, a dissipation system was designed to drain this excess of power.

At first, a transistor located on the EPS was introduced to this purpose, but it was responsible of a detrimental hotspot[1] during the hot case[2] (about 115^oC).

For this reason, the numerical simulations of L. Jacques [1] emphasized the necessity to shunt part of this power toward two patch resistors (Figure 3.1) glued on the antenna panel, and to encircle the transistor itself with a thermal strap, aimed at draining heat toward the antenna panel, too. In this way, the temperature of the transistor itself is reduced, and detrimental hotspots of the close devices are avoided. The EPS team fixed the value of the maximum power to be dissipated by the transistor to $1.88W$.

In this Chapter, the thermal conception of the strap is described. After the selection of the material, and after having introduced the hypotheses taken into account in the

[1]For sake of completeness, this hotspot was not too detrimental for the transistor itself (whose operational range is $[-65, 200]^oC$ [30]), but for the other electronical components close to it.

[2]See Chapter 4 and Table 4.3 for the definition of the hot case.

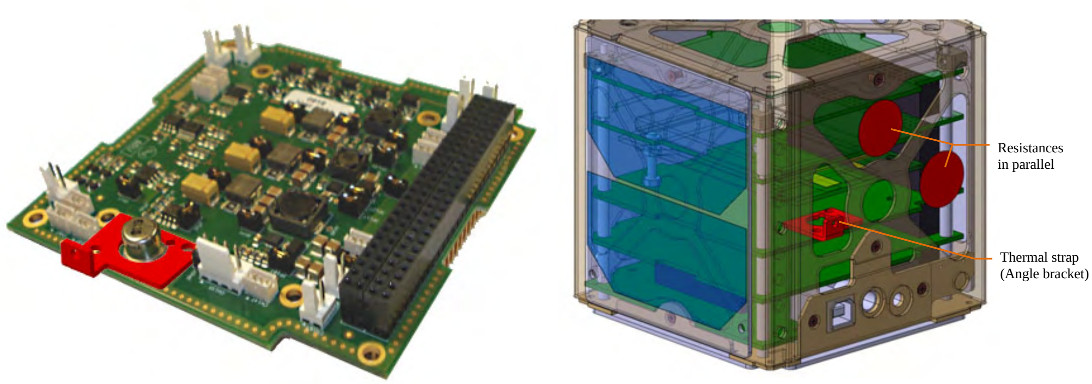

Figure 3.1: Dissipation system of the excessive-generated electrical power.

modelling, a preliminary sizing of the strap is performed by means of an analytical optimisation. Then, a FE model is developed in *COMSOL*, in order to study the sensibility of the solution to the most unknown parameters, and to finalize the sizing.

3.1 Material selection

The strap has to be as conductive and light as possible. So, the material property to be maximised is the thermal conductivity to density ratio, $f = \frac{k}{\rho}$, whose logarithmic maximisation curve is[3]:

$$\log f = \log \frac{k}{\rho} \Rightarrow \log k = \log \rho + \log f \tag{3.1}$$

The material selection was performed by means of *CES EduPack*, as shown in Figure 3.2. Furthermore, just materials suitable for space applications were considered, and the choice was reduced to:

- Aluminium alloys,
- Pure copper.

Finally, copper was chosen because it allows to have a tinier strap and a smaller w_2 (i.e., no contact between the Pumpkin frame and the strap, see Figures 3.3(a) and 3.1), because of its higher conductivity.

The density of the copper is $8900\frac{kg}{m^3}$[15], while, as pessimistic value, the thermal conductivity is supposed to be $k_{Cu} = 200\frac{W}{m\ K}$ [15].

3.2 Hypotheses of the numerical model

The geometry and the nomenclature of the numerical model of the strap are shown in Figure 3.3(a). Furthermore, its integration is shown in Figure 3.3(b), where the red and the blue panels represent the antenna and EPS board, respectively. The strap has to be able to evacuate $1.88W$ in each situation. For this reason, the lowest ΔT forecast by the numerical simulations is considered [1]:

- temperature of the transistor: $T_{trans} = 67^oC$,
- temperature of the antenna panel: $T_{an} = 35^oC$.

[3]An analogous reasoning but more detailed was performed in Section 2.6.

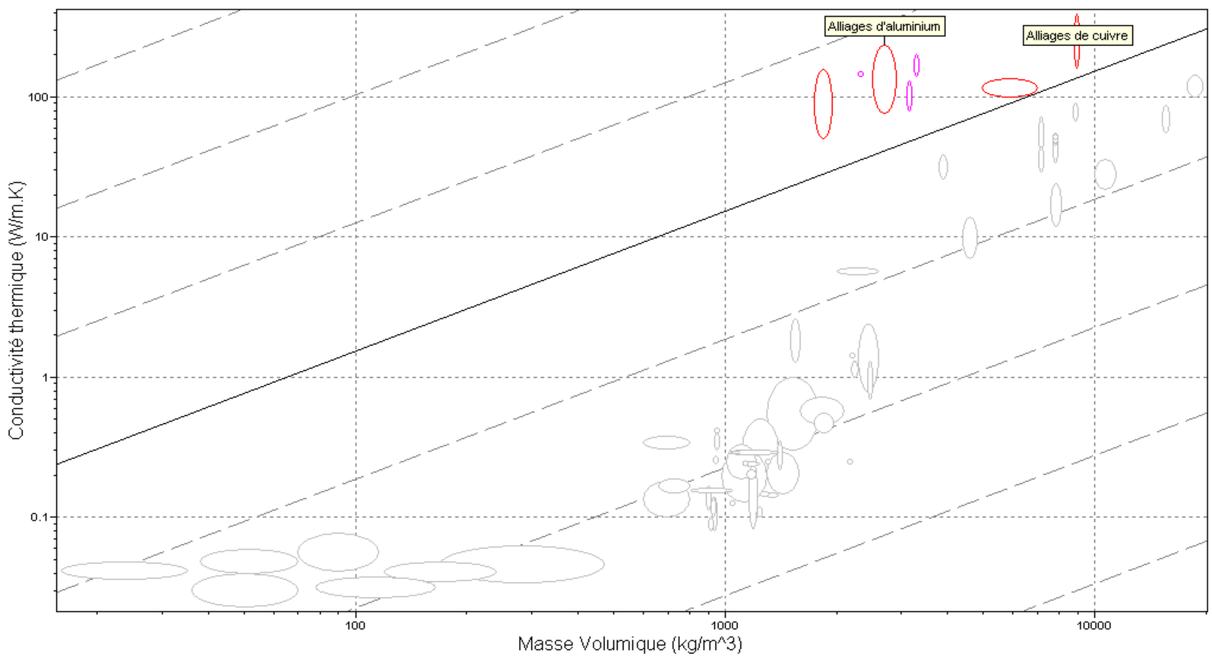

Figure 3.2: Material selection: in x-axis the density ρ $\left[\frac{kg}{m^3}\right]$, and in y-axis the thermal conductivity k $\left[\frac{W}{m\ K}\right]$.

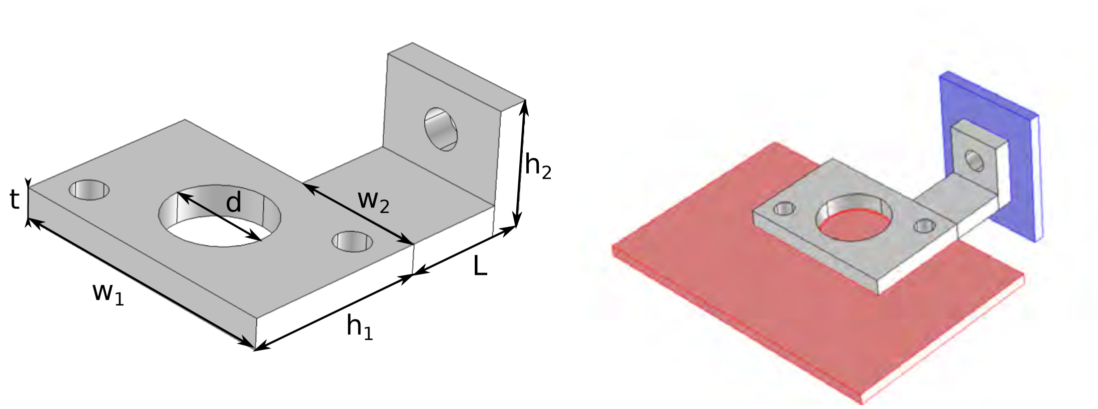

(a) Nomenclature (b) Integration

Figure 3.3: Geometry of the strap.

The numerical model implemented is based upon different hypotheses, mostly due to the presence of several uncertain parameters:

- The composition of the PCB, and so its conductivity. It is known that 6 copper layers compose the EPS PCB, nonetheless data on their thickness are not available. For this reason, as pessimistic value, a transverse conductivity of $0.3\frac{W}{m\ K}$ is retained (i.e., FR4 conductivity, according to [15]), and a longitudinal conductivity of $15\frac{W}{mK}$ is supposed [31].

- The characteristics of the insulating coating that will be placed on the EPS PCB. To this purpose, a contact conductance of $5000\frac{W}{m^2\ K}$ was considered between PCB and strap (i.e., a foil of thickness $0.1mm$ and conductivity $0.5\frac{W}{m^1\ K}$). However, if possible, it is advised not to employ such insulator on this part of the EPS.
- The contact conductance between the antenna panel and the strap. A parametric analysis in function of this variable is performed in Section 3.4.
- The length L. The distance between the end of the EPS PCB and the antenna panel is $d_{EPS-AP} = 6.015mm$. Nonetheless, the strap will be fabricated by bending a plane copper sheet, so that the length of the link depends on the bending radius. For this reason, a guess value of $10mm$ is considered; later, the consistence of this hypothesis will be verified in Section 3.5.
- The radiative exchanges are neglected in order to consider the worst conditions for the strap (i.e., all the power has to be dissipated by conduction).
- Concerning the link between transistor and EPS PCB, it consists of three metallic flaps (fixed to the transistor itself), which cross the PCB and are welded on the other side[4]. Nonetheless, in the FE model, this joint was simplified by considering the only contact between the base of the transistor and the external surface of the EPS.
- The power to be dissipated is considered to be the 10% more than the maximum value (i.e., about $2.1W$).

Furthermore, the transistor is considered isotherm, because of its metallic box and small dimensions). Thus, the boundary conditions imposed to the model are:

- T_{trans} on the connection surface of the transistor (Figure 3.4(a)),
- T_{an} on the external surface of the antennas panel (Figure 3.4(b)). Such condition is imposed on the external section rather than the internal or the central one, because it represents the worst case.

In this way, the heat path, shown in Figure 3.7, consists of:

- Transistor base[5] (imposed temperature)
- EPS PCB

[4] the geometry and the sizes of the transistor are shown in Appendix D.1.

[5] For sake of completeness, the joint resistance of the transistor is $10\frac{^oC}{W}$, but it is not taken into account, since the numerical simulations of L. Jacques directly estimated the temperature on the PCB in correspondence of the transistor.

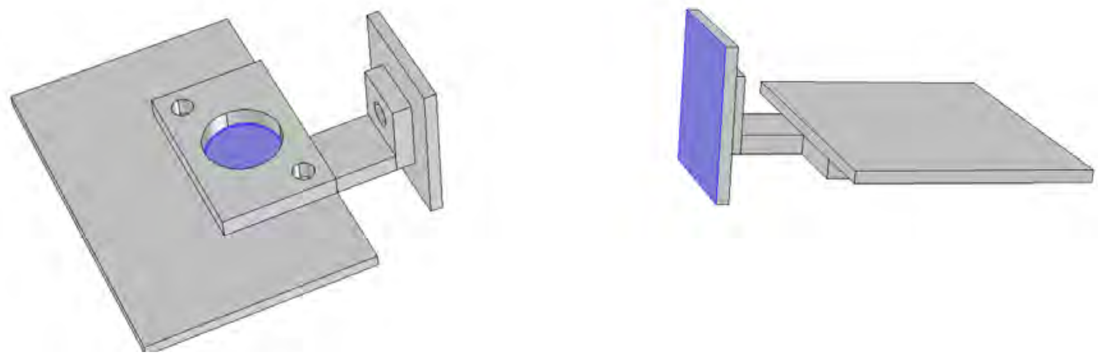

(a) $T = 67^oC$ (b) $T = 35^oC$

Figure 3.4: Boundary conditions.

- Insulating coating on the EPS PCB
- Strap
- Antenna panel (imposed temperature)

3.3 Preliminary sizing

Before proceeding with the discussion of the results of the numerical model, a preliminary sizing of the strap is proposed.

Considering Figure 3.3(a), the following parameters are retained as design variables:

- the width of the strap, w_2,
- the diameter of the hole encircling the transistor, d,
- the thickness of the strap, t.

On the contrary, the variables w_1 and h_1 are considered constant, because, as shown in Figure 3.5, a surface of 23×15 mm^2 is already present on the EPS to house the strap. Furthermore, h_2 is not considered since, as shown in Section 3.4, it does not affect significantly the solution.

The sizing procedure proposed in this section is analytical, and it allows to estimate just w_2 and t by means of a constrained optimisation.

The objective function to minimize is the mass of the strap, that is (Figure 3.3(a)):

$$M = \rho_{Cu} t \left[w_2 \left(L + h_2 - t \right) + h_1 \cdot w_1 - \frac{\pi}{4} d^2 \right] \tag{3.2}$$

while the constraints of the problem are:

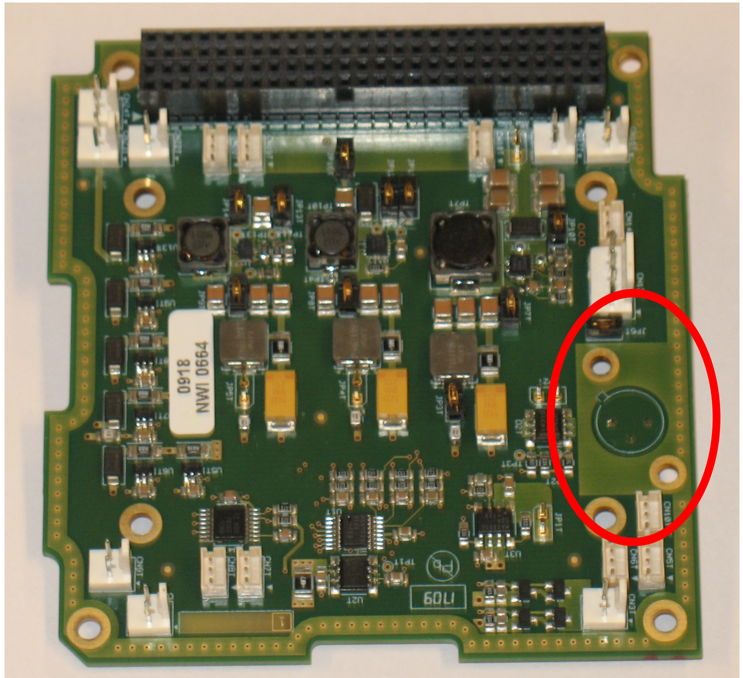

Figure 3.5: Surface reserved to the strap on the EPS. The circle in the center of such area corresponds to the placement of the transistor.

- the total thermal resistance R_{tot} has to be such that the power dissipated is at least equal to Q_{max}, with a margin of $n = 10\%$:

$$n\ Q_{max} \geq \frac{T_{trans} - T_{an}}{R_{tot}} \tag{3.3}$$

where R_{tot} is the sum of the contact resistance between EPS and strap, $R_k^{(PCB)}$, the conductive EPS PCB resistance, and the conductive strap resistance.

The EPS PCB resistance is then approximated as:

$$R_c^{(PCB)} \simeq \frac{t_{PCB}}{w_1\ h_1\ k_{FR4}} \tag{3.4}$$

where $t_{PCB} = 1.6mm$ is the thickness of the PCB, and k_{FR4} its cross thermal conductivity.

The strap resistance is supposed to be mainly due to the flap of length L, so that:

$$R_c^{(strap)} \simeq \frac{L}{w_2\ t\ k_{Cu}} \tag{3.5}$$

The conduction through the antenna panel is neglected because of the good thermal conductivity of the aluminium and the small thickness of the panel (i.e., $1.5mm$).

- Both t and w_2 have to be non-negative,
- w_2 has to be smaller than $8mm$ to avoid a contact between the strap and the pumpkin frame (see Figure 3.1, right).

So, the optimisation problem is

$$min_{t,w_2}\,(M) \qquad with \tag{3.6}$$

$$\begin{cases} t \cdot w_2 & \geq & n\,\frac{L}{k_{Cu}}\left(\frac{T_{trans}-T_{an}}{n\ Q_{tot}} - R_k^{(PCB)} - R_c^{(strap)}\right)^{-1} \\ t & \geq & 0 \\ w_2 & \geq & 0 \\ w_2 & \leq & 10 \end{cases} \tag{3.7}$$

where the parameter h_2 is set to $10mm$[6], and d is supposed to be equal to the diameter of the transistor (i.e., $9.4mm$, see Appendix D.1).

The results of the optimisation are shown in Figure 3.6. The optimal solution activates two constraints, and the values estimated are:

$$t = 2\ mm \tag{3.8}$$

$$w_2 = 8\ mm \tag{3.9}$$

Indeed, these data are just an approximation, but they provide an order of magnitude, and, above all, they show that the parameter w_2 has to be set to its maximum value.

3.4 Parametric analysis and final sizing

In the numerical model, the figure of merit is the power dissipated by the strap, and it is computed as:

$$W_{dis} = \int_S \vec{q}\ \cdot\ \vec{n}\ dS \tag{3.10}$$

where $\vec{q}$ is the conductive heat flux, S the surface shown in Figure 3.7, and $\vec{n}$ the unit vector normal to such surface.

In Figures 3.8, 3.9 3.10, it is shown the power dissipated by the strap in function of w_2, d, t, respectively. Concerning w_2 and t, the slope of the regression curve is $53.3\frac{mW}{mm}$ and $152.1\frac{mW}{mm}$, respectively. Nonetheless, the parameter which most affects the solution is d, and, for this reason, its fabrication tolerance has to be carefully determined. The sensibility of the solution to this parameter is $-462\frac{mW}{mm}$, and it has to be as close as possible to the diameter of the strap to maximize the conductive exchange.

On the contrary, the parameter h_2 has little influence on the solution (slope of the regression curve $2.7\frac{mW}{mm}$). At first, a configuration characterised by a symmetric allocation

[6] A smaller value might be critical under the point of view of the integration (performed with a bolted screw, as discussed in Section 3.5).

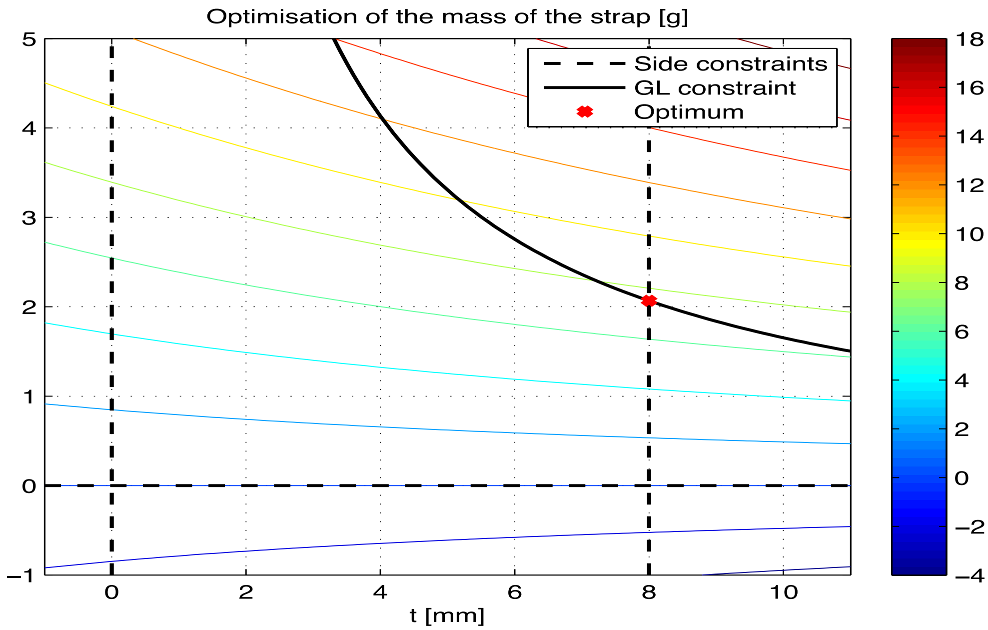

Figure 3.6: Analytical optimisation.

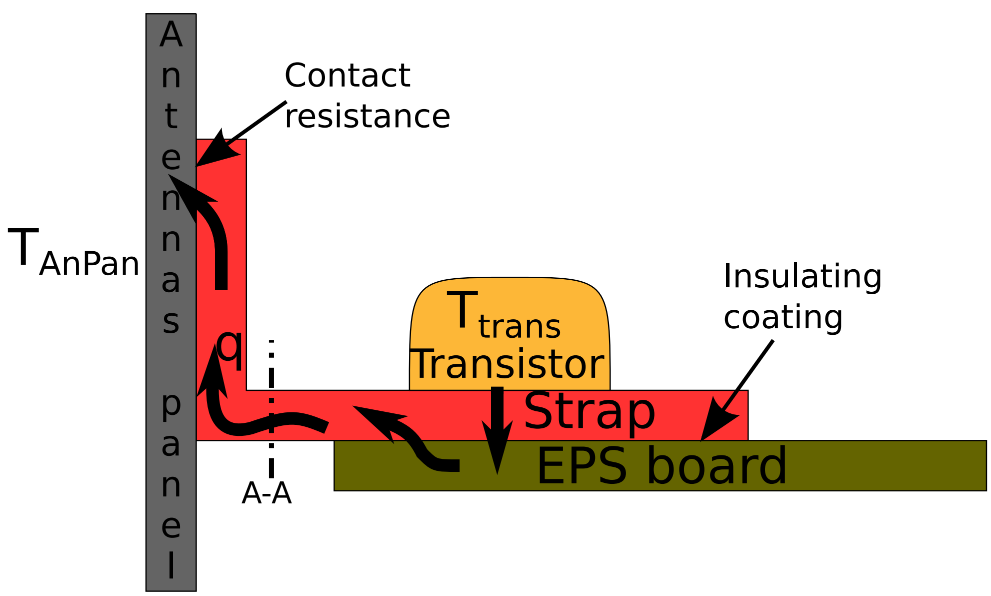

Figure 3.7: Heat path. The integration of the conductive flux is performed in the section A-A.

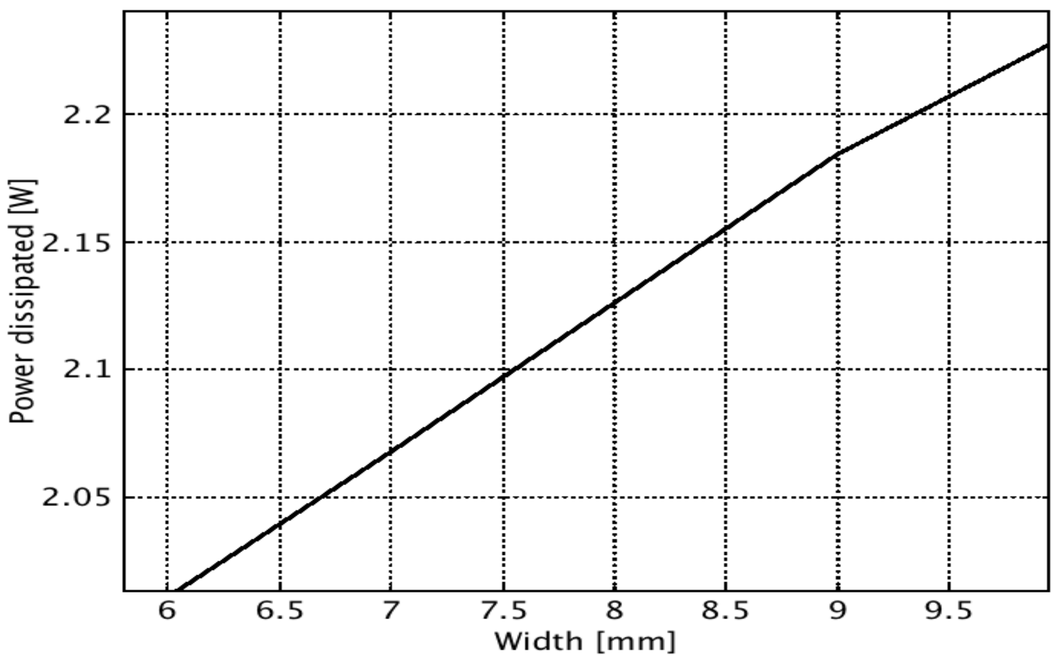

Figure 3.8: Power dissipated in function of w_2 ($d = 10.1mm$, $t = 2.5mm$).

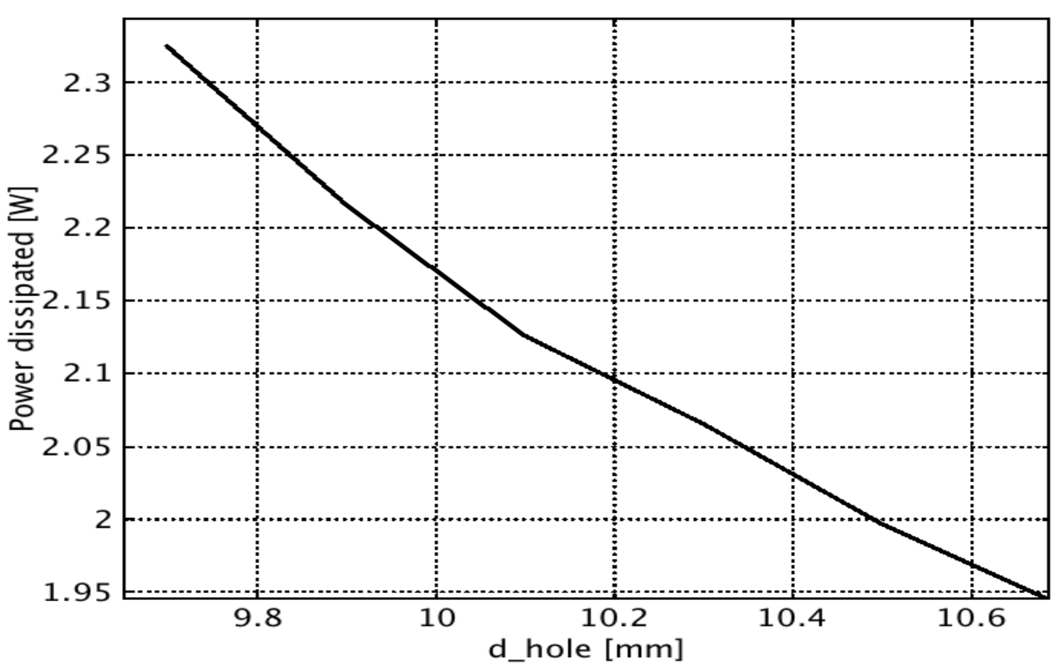

Figure 3.9: Power dissipated in function of d ($w_2 = 8mm$, $t = 2.5mm$).

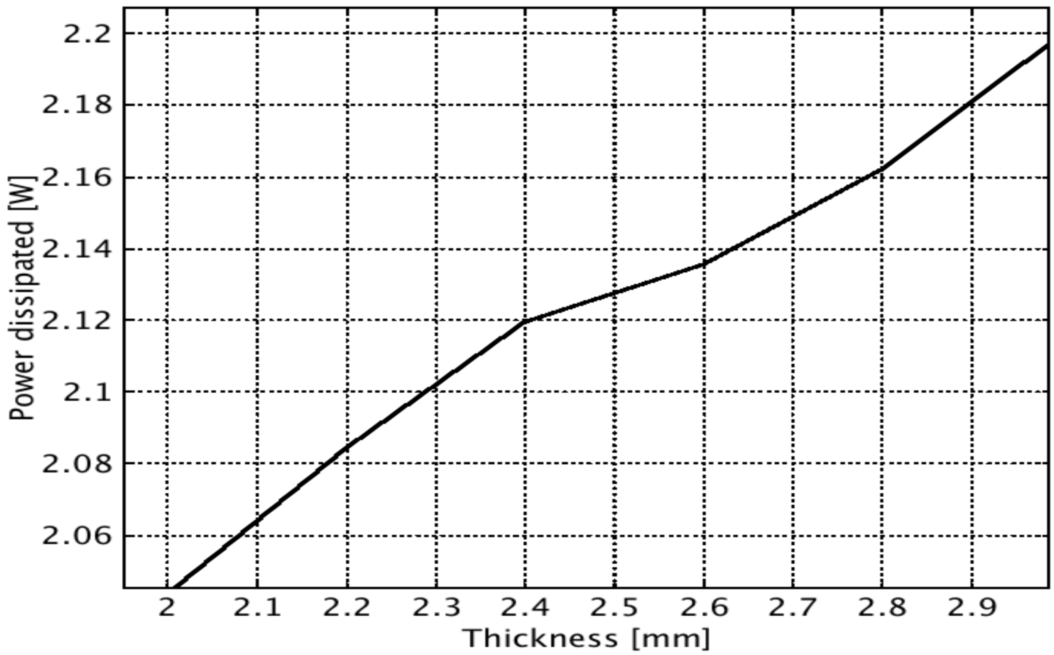

Figure 3.10: Power dissipated in function of t ($w_2 = 8mm$, $d = 10.1mm$).

of the segment h_2 (Figure 3.11) was envisaged. In this way, the heat flux coming from the segment L was able to be evacuated in two directions. Nonetheless the advantage of this configuration was minimal ($\mathcal{O}(1\%)$), and it did not justified the higher complexity in the realisation of the piece.

Then, the presence of a contact resistance in the interfaces was envisaged. Such element represent the most unknown variable.

Concerning the PCB, the characteristics of the insulating layer placed on the surface are unknown. For this reason, as stated in Section 3.2, a contact conductance of $5000\frac{W}{m^{-2}K}$ was considered in the nominal case.

On the other side, $25\mu m$ of oxide of aluminium are present on the surface of the antenna panel[7]. The conductivity of this oxide is $18\frac{W}{m\ K}$ [32], so that the surface conductance is $720000\frac{W}{m^2K}$. Nonetheless, as suggested in Figure 3.12, further resistance due to the contact is taken into account, so that a global contact conductance of $100000\frac{W}{m^2K}$ is retained in the nominal solution.

The sensibility of the solution in function of the interface conductances is shown in Figures 3.13 and 3.14.

Another unknown parameter is the longitudinal conductivity of the PCB. The influence of this parameter on the solution is shown in Figure 3.15. The slope of the regression curve is 0.057 mK. However, the nominal value assumed ($15\frac{W}{mK}$) is likely reasonable (or even

[7]It is not known if these two insulating means can be removed from the contact surface of the strap. Meanwhile, they are taken into account in this analysis, in order to considerate the worst conditions.

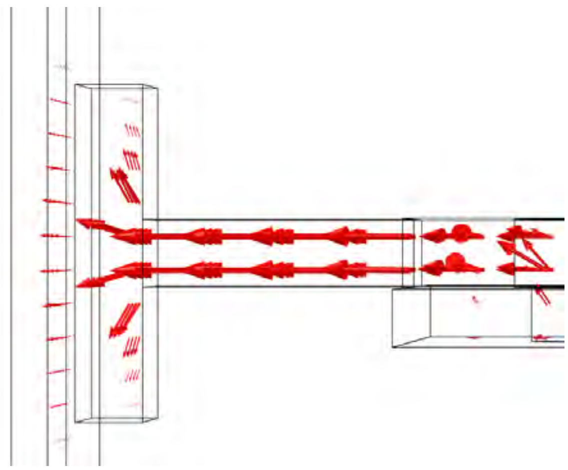

Figure 3.11: Configuration with the symmetrically-distributed contact surface.

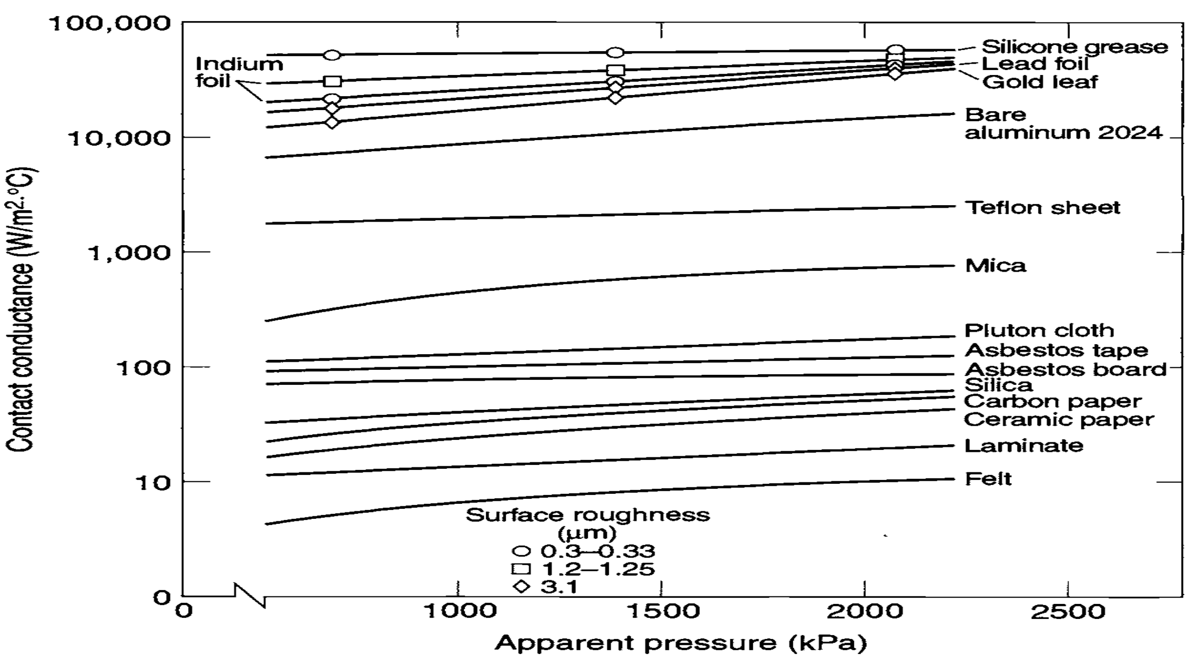

Figure 3.12: Contact conductance in function of pressure and filler (from [12]).

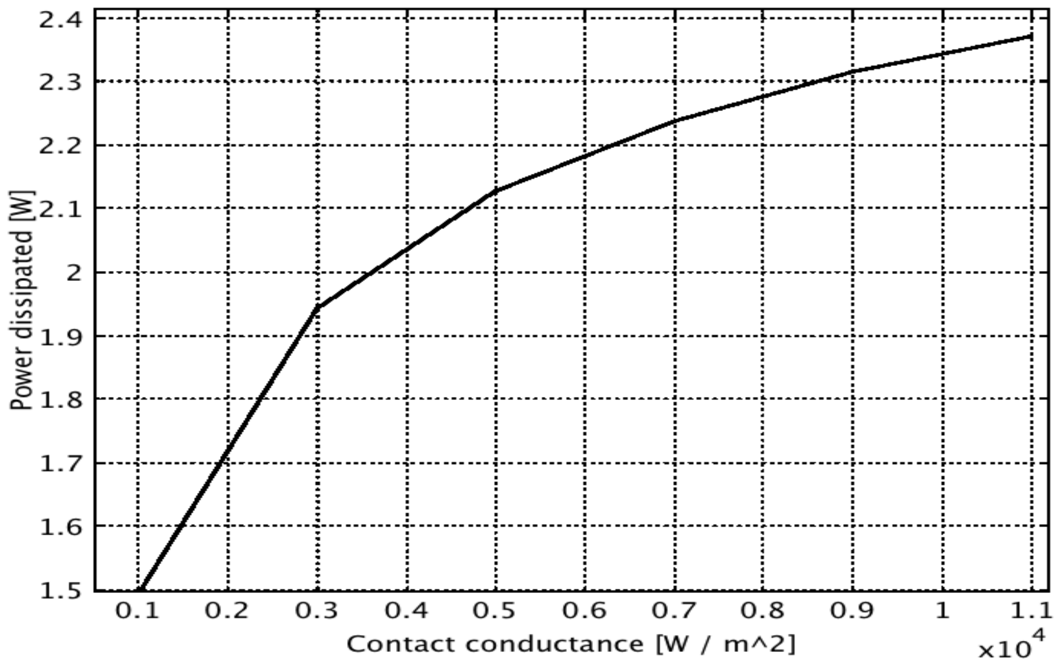

Figure 3.13: Power dissipated in function of the contact conductance between strap and EPS PCB ($w_2 = 8mm$, $t = 2.5mm$, $d = 10.1mm$).

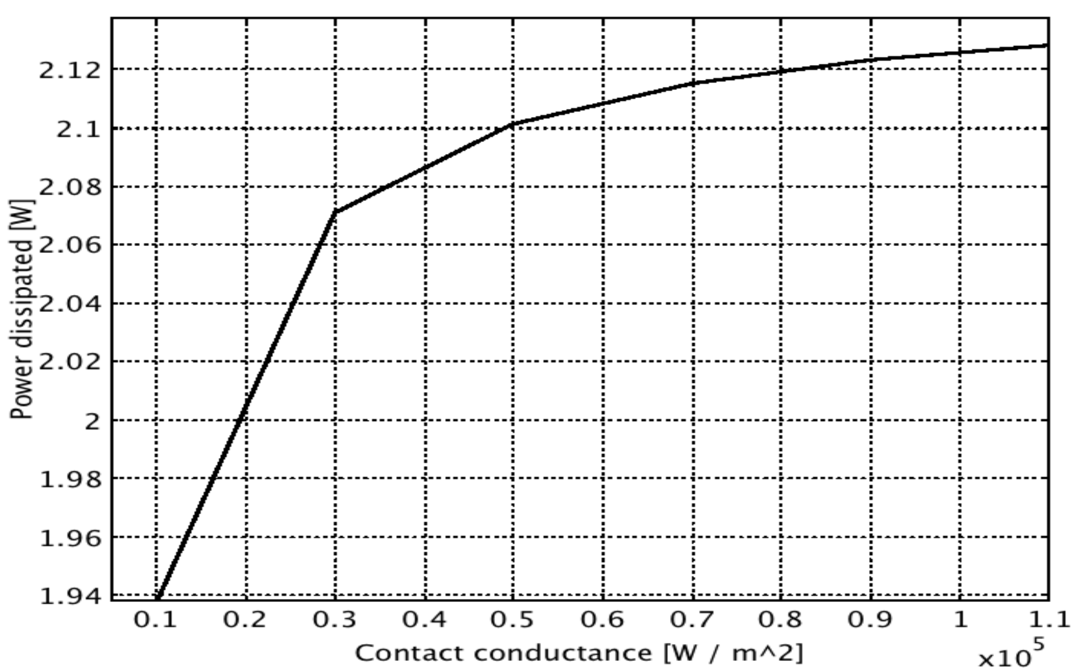

Figure 3.14: Power dissipated in function of the contact conductance between strap and antenna panel ($w_2 = 8mm$, $t = 2.5mm$, $d = 10.1mm$).

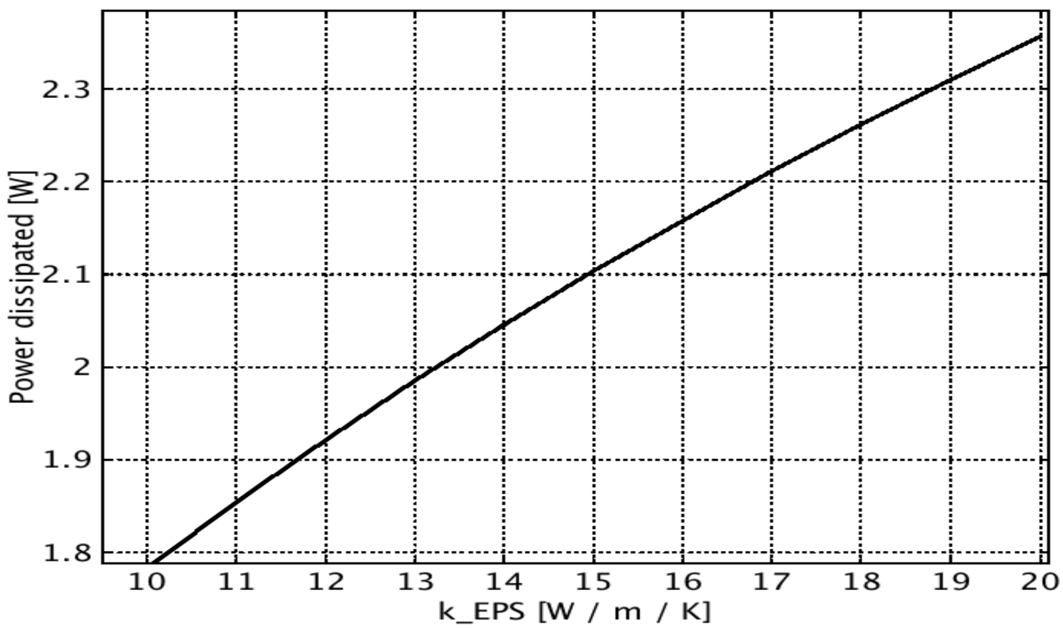

Figure 3.15: Power dissipated in function of the longitudinal conductivity of the PCB ($w_2 = 8mm$, $t = 2.5mm$, $d = 10.1mm$).

pessimistic) for a 6-layer PCB, according to [31]. Nonetheless, a more accurate estimation of it will be performed as more detailed data on the composition of the EPS PCB will be allowable.

Finally, the values of the design parameters were fixed at:

$$w_2 = 8mm \tag{3.11}$$
$$t = 2.5mm \tag{3.12}$$
$$d = 10.1mm \tag{3.13}$$

Their determination was performed (manually) by granting a minimum margin of $n = 10\%$ in the power dissipated in the nominal case, while trying to minimise the weight.

In this way, the power dissipated is $2.1257W > n\ Q_{max}$. The solution in terms of temperature field, obtained in the nominal case, is shown in Figure 3.16.

3.5 Fixing means and manufacturing

As shown in Figure 3.5, two holes are already present on the EPS board to screw the strap. Two screws $M2.5 \times 8$ are exploited for this purpose. Then, one screw $M3 \times 8$ is employed to fix the strap on the antenna panel.

Finally, to improve contact conductance, the introduction of a conductive filler, as *CHO-THERM 1678* [33], in the interfaces is strongly advised.

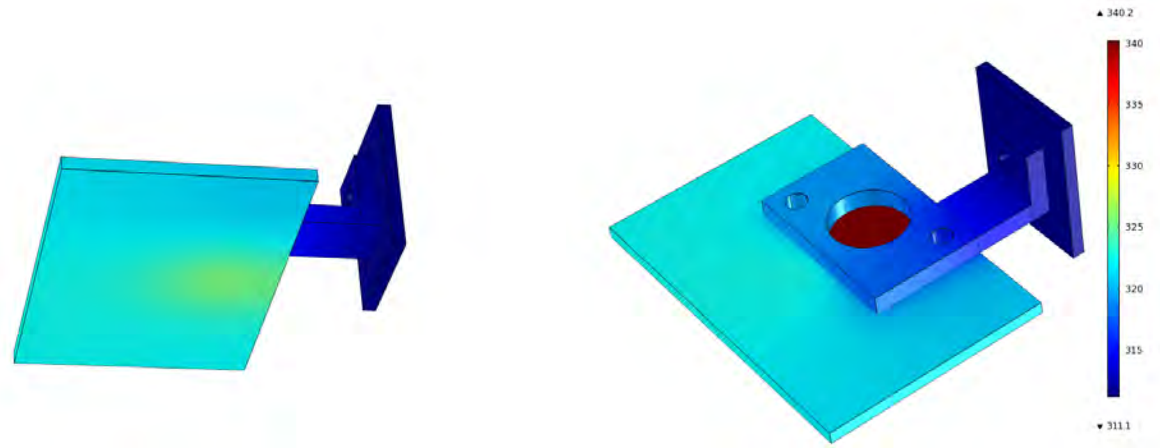

Figure 3.16: Numerical solution in the nominal case.

The manufacturing of the strap is performed by giving the shape of Figure 3.17(a) to a copper sheet. Then, the central hole (encircling the transistor) and the holes for the screws are made ($2.9mm$ of diameter on the EPS side, $3.2mm$ on the antenna panel side). Finally, the strap is bended to get the final shape (Figure 3.17(b)).

For a ductile material, like the copper, the bending radius has to be equal or bigger than the thickness. So, by considering the nominal thickness ($2.5mm$), the internal radius is $R_{int} = 2.5mm$, and the external $R_{ext} = 5mm$, while the length of the external fibres is:

$$L_{ext} = d_{EPS-AP} - R_{ext} + \frac{\pi}{2} R_{ext} = 8.87mm \tag{3.14}$$

which is less than $L = 10mm$. In this way, the numerical model discussed in Section 3.4 represents a pessimistic valuation of the reality. In fact, a simulation with a more realistic geometry was performed a posteriori (Figure 3.18), and the dissipated power is $2.1907W$.

Summary

The design of the strap is summarized in:

- The material employed for the strap is the **pure copper**.
- The functionality of the strap is granted for a minimum $\Delta T = 32^oC$.
- The geometrical parameters of the strap are:
  - $w_1 = 23\ mm$
  - $h_1 = 15\ mm$
  - $w_2 = 8\ mm$
  - $h_2 = 10\ mm$

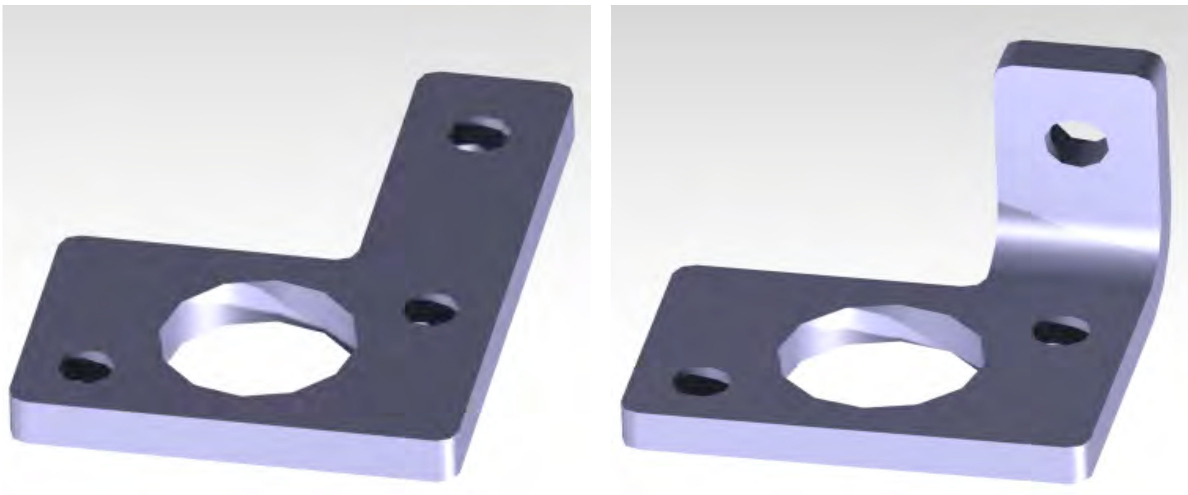

(a) Plane sheet (b) Final strap

Figure 3.17: Fabrication process

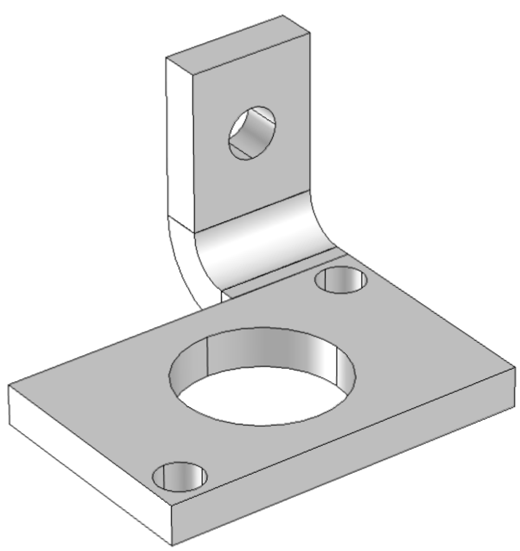

Figure 3.18: Geometry of the FE model "a posteriori".

  - $t = 2.5\ mm$
  - $d = 10.1\ mm$

- The strap is fixed by means of two screw $M2.5 \times 8$ on the EPS board and one $M3 \times 8$ on the antenna panel. *CHO-THERM 1678* has to be employed as filler in the interface.

- The thermal conductance between transistor and antenna panel is $GL = 0.0664 \frac{W}{K}$ in the nominal case.

- The weight of the strap is $8.25g$ (by considering a density of $8900 \frac{kg}{m^3}$).

The piece is not manufactured, yet. Furthermore, a development test, not discussed in this dissertation, is strongly advised in order to validate the design.

Chapter 4

Global numerical model

This Chapter is devoted to the global numerical modelling of OUFTI-1, developed with *ESATAN-TMS*.

A global and detailed model was already developed by L. Jacques [1] in 2009-2010. However, the introduction of the new BAT subsystem requires its update.

The new model is aimed at:

1. assessing the impact of the bare introduction of the new BAT support on the temperature range of the batteries, in order to determining the temperature levels to impose during the BAT test described in Section 2.7.2,

2. verifying that the battery issue is fixed after the introduction of the new design discussed in Section 2.6,

3. verifying that the transistor issue is fixed with the introduction of the thermal strap described in Section 3,

4. verifying that there are not new thermal issues,

5. estimating the temperature range of the spacecraft, which is necessary to make the proflight test procedure (Chapter 5).

For these reasons, this Chapter has the main purpose to answer to these questions, and the numerical model is just an instrument to pursue this object. Indeed a description of the modelling is provided, but more details about the analogous model developed by L. Jacques are available in [1], so that useless repetitions are avoided.

So, the Chapter begins with a brief recall of how to build a *ESATAN* model. Then, the OUFTI-1 model is described. Finally, the five question listed above are answered one-by-one.

4.1 The numerical model

An *ESATAN* model is defined by [34]:

GMM: it consists in the definition of the geometry and of the nodal breakdown of the spacecraft. Furthermore, the optical properties of the surfaces and the analysis case are defined, too. The analysis case might be either an in-orbit simulation or not. The GMM is then exploited to perform the *radiative analysis*, whose output are the GR between the nodes and the external fluxes (solar, albedo, earth infrared).

TMM: it consists in the definition of the thermal properties of the nodes (thermal capacities) and between the nodes (GL). Furthermore, the internal dissipation is defined, too, as well as the eventual subroutines (e.g., in the OUFTI-1 model they are: heaters, dissipation system and electrical power management). The outputs of the GMM are an input for the TMM, and they define the radiative couplings (GR) and the boundary conditions (external fluxes). The TMM is then exploited to perform the *thermal analysis*, which provides the temperature of the nodes as output.

In this Section, both the GMM and the TMM of the OUFTI-1 model are briefly presented.

4.1.1 The Geometrical Mathematical Model

Nodal breakdown

The geometry of the model is shown in Figure 4.1, and it consists of:

Structure: because of the good conductivity of the aluminium, just one node is exploited to model each face of the Pumpkin Frame (Figure 4.1(b)), and another node for each foot.

Solar cells: one node for each. 2 solar cells are placed on 5 of the 6 faces (Figure 4.1(a)).

Shielding: it consists of five $1.5mm$-thick aluminium panels that are glued on the Pumpkin Frame (Figure 4.1(a)). Solar cells are glued on them. As for the main structure, just one node is exploited to model each panel.

Antenna panel: is the panel devoted to the antenna deployment mechanism, and it is placed on the only face without solar cells. It is modelled with just one node.

PCBs: the two OBC (home-made and Pumpkin) are discretized with just 4 nodes each, while 100 nodes are exploited for the EPS, xEPS, and COM.

The discretization of the two OBC is less refined than the one of the other PCBs, because of the their low power dissipation (Table 3.1 and Section 4.1.2), and the absence of "hot points" (i.e., with localised dissipation).

BAT subsystem: the same discretization descibed in Section 2.2.

Antennas: 20 nodes for each antenna (Figure 4.1(a)), because of the high temperature gradients that they have to withstand (see Section 4.2).

Spacers: one node for each.

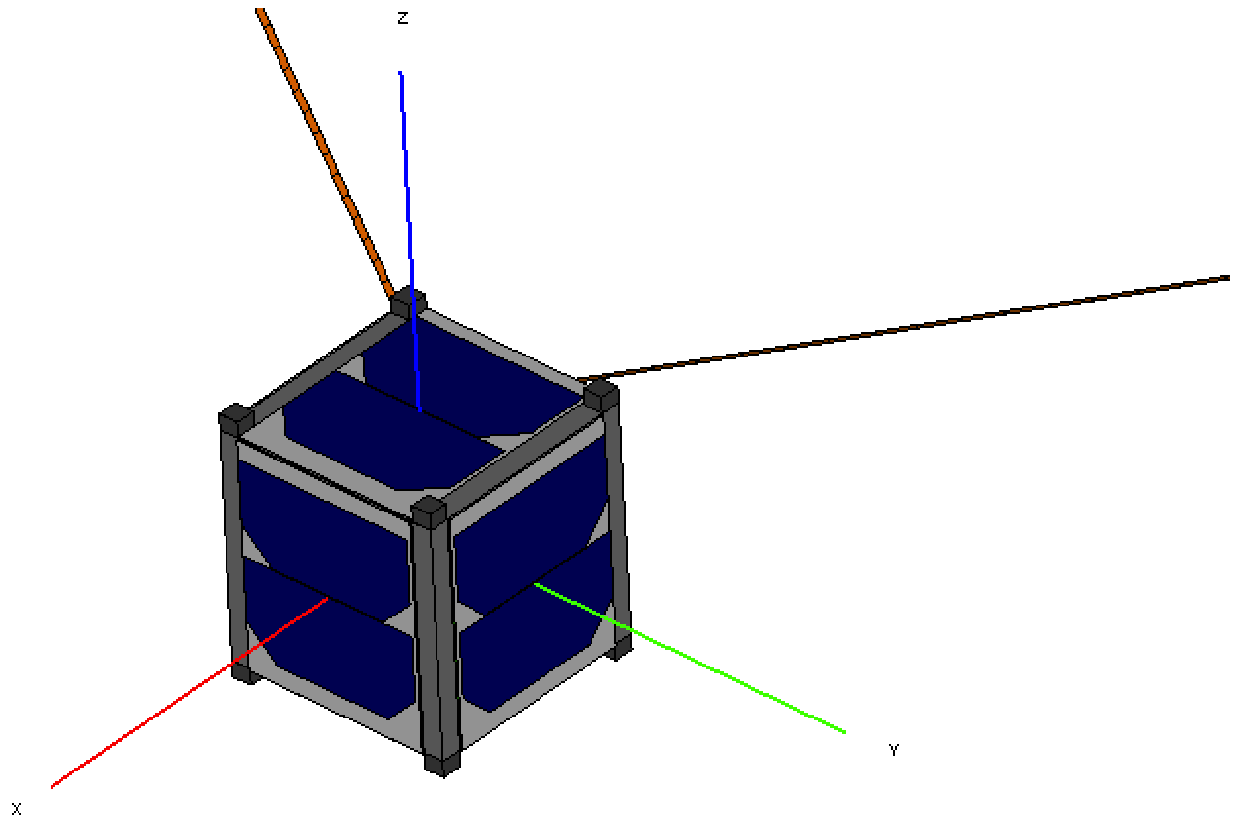

(a) Exterior

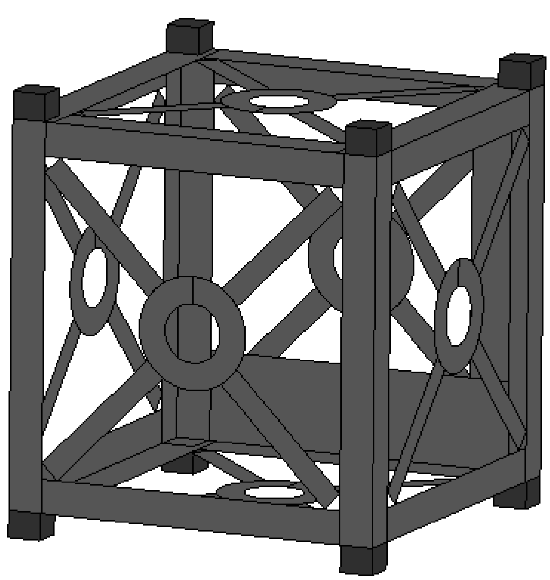

(b) Pumpkin Frame

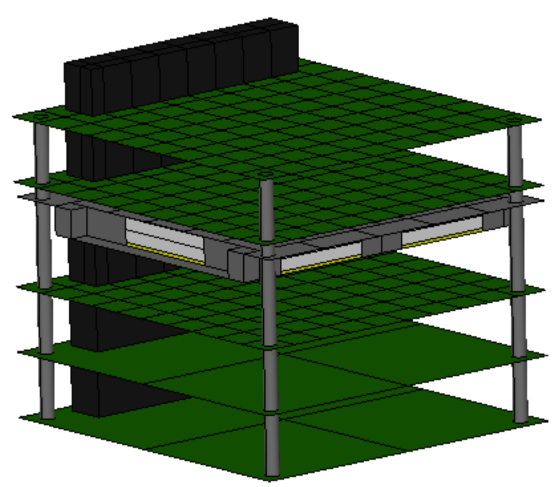

(c) PCB stack

Figure 4.1: The geometry of the model

Material or Coating	ϵ	α	**Surfaces**
Al 5052-H32, Alodine treatment	0.15	0.08	Pumpkin frame
Al 6061-T6, Alodine1200 treatment	0.1	0.3	Spacers
Al 7075-T6	0.07	0.5	Batteries support, Shielding (in)
Anodized Aluminium	0.7	0.8	Rails, Antenna panel
Batteries	0.8	-	
Copper	0.02	0.32	Antennas, Strap
Delrin	0.8	-	BAT Spacers
FR4	0.8	-	PCBs
Kapton 2mil	0.81	0.87	Shielding (out)
Polystyrene	0.8	-	I2C
Solar Cell	0.81	0.91	

Table 4.1: Optical properties, from [1] and [36].

Optical properties

Optical properties are defined for each radiative-active surface, independently by the nodal breakdown.

The properties required by *ESATAN* are just the solar absorptance, α_s, and the infra-red emittance, ϵ_{IR}. Indeed, this notation might be confusing, since, by hypothesising that [35] the radiation is diffuse and that the body is grey, the Kirchhoff's law[1] becomes:

$$\epsilon(T) = \alpha(T) \tag{4.1}$$

so that the solar absorptance is also equal to the solar emittance (and idem for ϵ_{IR}), and there seems to be no reason to call one absoptance and the other emittance.

However, since the solar radiation is disjointed by the infra-red one, it is reasonable to suppose that the spacecraft emits in the infra-red with emissivity $\epsilon(T_{spacecraft}) \simeq \epsilon_{IR}$, and absorbs direct and albedo solar fluxes with absorptance $\alpha(T_{sun}) = \alpha_S$. On the contrary, the earth infra-red flux is absorbed with absorptance $\alpha(T_{Earth}) \simeq \epsilon_{IR}$.

The list of the optical properties employed in the model is provided in Table 4.1.

Analysis case

The only orbital parameters known are [1]:

- apogee altitude $354km$,
- perigee altitude $1447km$,
- inclination 71^o.

[1]The monochromatic, directional emittance and the monochromatic, directional absorptance for a surface that is in thermodynamic equilibrium with its surrounding, are equal [35].

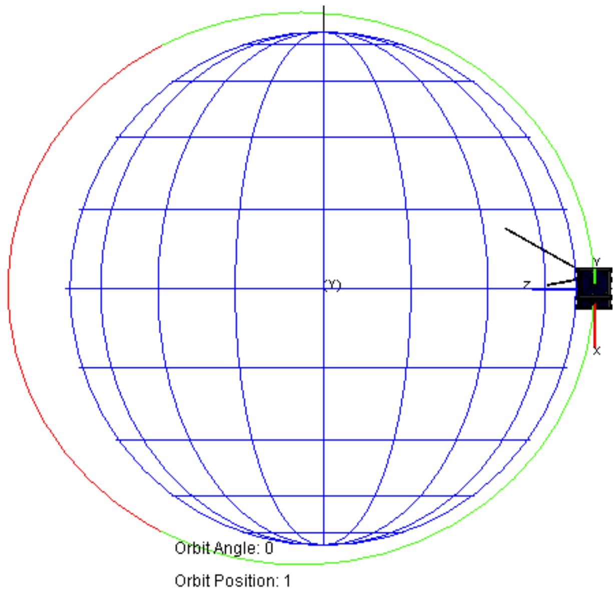

Figure 4.2: OUFTI-1 orbit (seen from the orbital plane, z axis is the node line). The red line is the maximum eclipse, characterizing the cold case.

For this reason, two analysis case are defined to represent the worst conditions the satellite will have to withstand to:

Hot case orbit: the node line is orthogonal to the sun direction, so that the orbit is permanently illuminated. The sun constant is set to the winter solstice value, $1414\frac{W}{m^2}$. The argument of perigee is set to 0^o (but it is not relevant in this case).

Cold case orbit: the node line is toward the sun direction, and the argument of perigee is set to 0^o, so that the perigee is on the ascending node between Earth and Sun. In this way, the eclipse time is maximised[2], and it is equal to $35'$ (see Figure 4.2). The sun constant is set to the summer solstice value, $1322\frac{W}{m^2}$.

Concerning the attitude, the Attitude Determination and Control System (ADCS) of the spacecraft is fully passive and it consists of:

- one permanent magnet polarised along the direction y of the body axes of OUFTI-1 (shown in Figure 4.1(a)), aimed at aligning this axis along the direction of the geomagnetic field,
- two hysteretic bars, aimed at damping the rotations about the other two axes.

As the orbit inclination is relatively high, the alignment with the geomagnetic field is approximated by prescribing a constant rotation speed around y axis such that the CubeSat performs two revolutions during one orbit, as Shown in Figure 4.3.

[2]The apogee is in eclipse, and the orbital velocity is the minimum in this point.

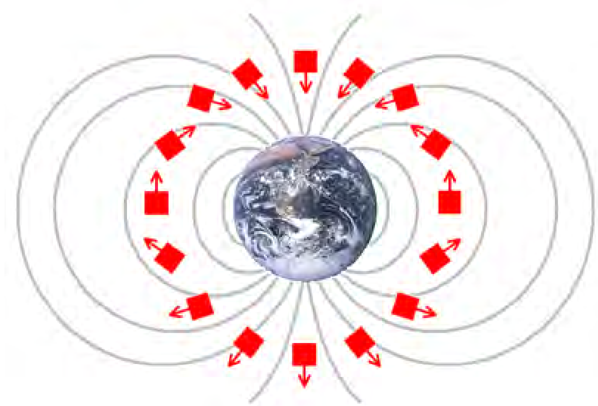

Figure 4.3: Alignment of the spacecraft with the local geomagnetic field, from [37].

4.1.2 The Thermal Mathematical Model

Heat capacities

The heat capacities are defined by multiplying the mass of each node by the specific heat of its bulk material. The properties of the material employed and the associated components are listed in Table 4.2.

The conductive network

Apart from some exception, most of the GL between two nodes (i and j) where computed as follow:

$$GL_{i,j} = \left(\frac{1}{2} \frac{t_i}{k_i\ S} + \frac{1}{2} \frac{t_j}{k_i\ S} + \frac{1}{GL_f} \right)^{-1} \tag{4.2}$$

where, considering Figure 4.4, t_i and t_j are the thickness of the $i-th$ and $j-th$ nodes, respectively, k_i and k_j the thermal conductivities of their bulk materials, S the contact surface ($S \equiv S_1$ in the Figure), and GL_f is either due to an eventual filler ($GL_f = \frac{k_f\ S}{t_f}$) or to a contact resistance ($GL_f = \frac{1}{R_{cont}}$), or to both of them.

However, for more complicate geometries, the GL was computed by means of a finite element model, as described in Chapter 3 concerning the conductance through the thermal strap, or in [1] concerning the conductances between the faces of the Pumpkin structure.

The network of the GL between the different subsystems is shown in Figure 4.5.

The power dissipated

The internal power dissipated is imposed according to the power budget of P. Thirion [39]. Three cases are defined to consider the most stressing conditions for the spacecraft:

Cold: minimum dissipation of the PCBs, and the efficiency of the solar cells is 30% (Begin of Life (BOL) value, according to [1]). Maximum eclipse time, as described in Section

Material	$k\left[\frac{W}{m\ K}\right]$	$C_s\left[\frac{J}{kg\ K}\right]$	$\rho\left[\frac{kg}{m^3}\right]$	**Components**
Al 5052-H32	145	980	2680	Pumpkin frame, Shielding
Al 6061-T6	160	900	2700	Spacers
Al 7075-T6	130	960	2810	Batteries support
Anodized Aluminium	145	980	2680	Rails, Antenna panel
Batteries	1.11	1315	4079	
Copper	390	380	8935	Antennas, Strap
Delrin	0.31	1400	1430	BAT Spacers
FR4	16.5	1136	1550	PCBs
Kapton	0.12	-	-	Shielding (exterior coating)
Phosphorus bronze	75	-	-	104 fins
Polystyrene	0.245	1600	1160	I2C
Glue Stycast 2850FT	1.44	-	-	
Solar Cell	100	711	-	

Table 4.2: Bulk properties, from [1], [15] and [38]. Thermal conductivity (k), specific heat (C_s) and density (ρ).

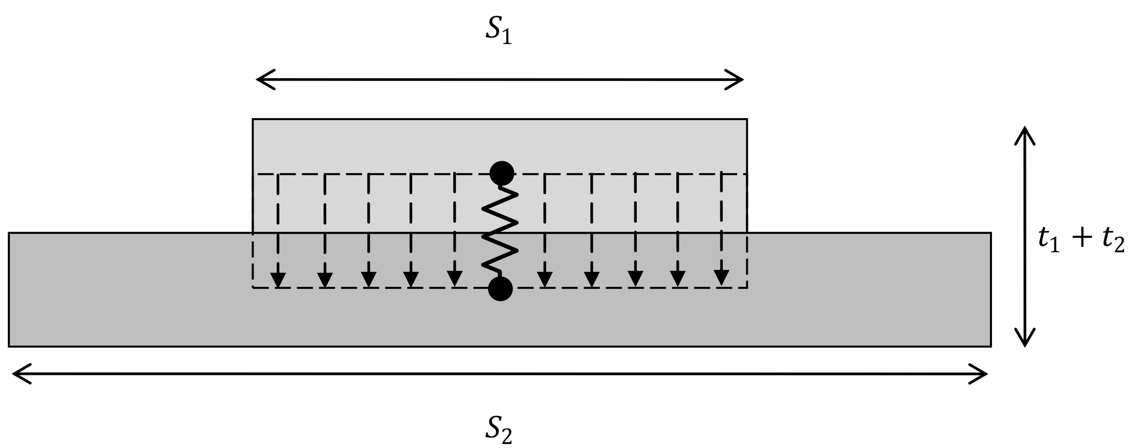

Figure 4.4: Computation of the linear conductances, from [1]

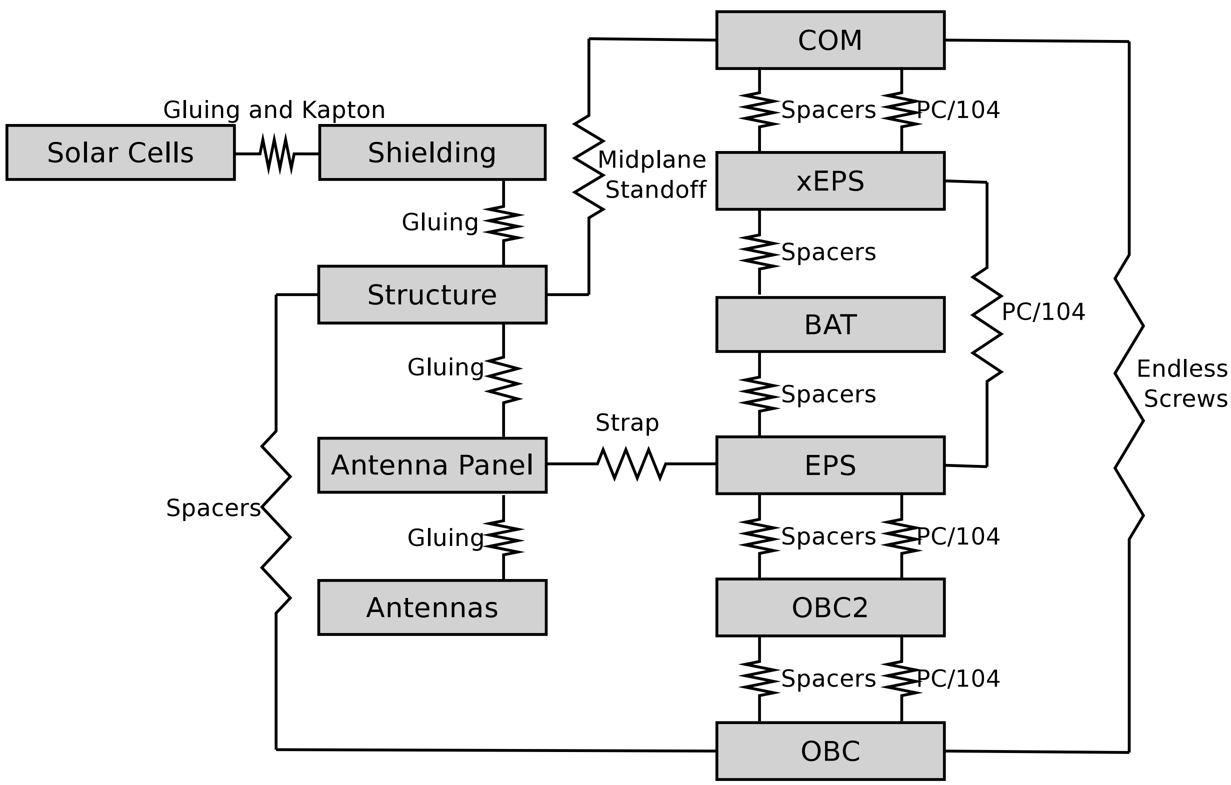

Figure 4.5: Network of the GL between the different subsystems. Internal GL are not represented.

	Parameter	Case Cold	Hot1	Hot2
	Solar constant $[W \cdot m^{-2}]$	1322	1414	1414
	Eclipse time	35'	0	0
	Solar Cell Efficiency	30%	27%	27%
Power $[W]$	OBC	0	0.05	0
	OBC2	0	0.05	0
	EPS	0	$0.625 + P_e$	P_e
	xEPS	0	0.3	0
	COM Amplifier	0	1.75	0

Table 4.3: Worst case definition. Apart from the COM, the other power are distributed on the PCBs. P_e is the excessive power dissipated by transistor and patch resistors.

4.1.1.

Hot1 maximum power distributed on the PCBs, and the efficiency of the solar cells is 27% (End of Life (EOL) value, according to [1]). Permanently illuminated orbit, as described in Section 4.1.1.

Hot2 minimum power distributed on the PCBs, the batteries are supposed to be fully charged, and the efficiency of the solar cells is 27% . Permanently illuminated orbit, as described in Section 4.1.1. This case is implemented to estimate the maximum temperature level of the transistor[3].

The location of the COM amplifier is still unknown, but a parametric analysis performed in [1] revealed that its hotspot is minimised if it is placed close to a corner of the COM PCB. And thus, in this model, it is supposed that this configuration is adopted (corner in direction $(+x, -y)$, considering the reference frame of Figure 4.1(a)).

For sake of clarity, all the parameters (orbital and power) defining the cold and the two hot cases are resumed in Table 4.3.

The subroutines

Two subroutines are implemented to model the behaviour of the heaters of the BAT subsystem, and the dissipation of the excessive generated power:

Heaters: the principle is analogous to the one described in Section 2.1. If the temperature of a battery drops below the set point of the thermostats (7.2^oC), its heater is turned on. Then, if the operating temperature is overtaken (23.9^oC), the heater is turned off. It is to emphasize the hysteretic behaviour of this system, because of the gap between set point and operating temperature.

[3] All the power that is not dissipated by the PCBs and that does not charge the batteries is transmitted to the transistor and to the patch resistors, described in Chapter 3.

Excessive power dissipation: the total electrical power generated by the solar cells is computed as:

$$Q_{elec} = \eta \sum_{j=1}^{N} Q_i^{(j)} \tag{4.3}$$

where N is the number of the cells, $Q_i^{(j)}$ is the total incident solar flux on the j_{th} cell[4] (direct and albedo) and η the efficiency of the cells.

So, by considering that $Q_{PCB} \geq Q_{elec}$ is the total electrical power employed by the PCBs (Table 4.3), according to [39], the power dissipated by the patch resistors is computed to be:

$$Q_{res} = \frac{R_{res}}{V_{bus}^2} \ (Q_{elec} - Q_{PCB})^2 \tag{4.4}$$

where $V_{bus} = 4.2V$, and $R_{res} = 2.35\Omega$ is the resistance of the patch resistors[5]. Finally, the power dissipated by the transistor is computed as:

$$Q_{trans} = Q_{elec} - Q_{PCB} - Q_{res} \tag{4.5}$$

4.2 Results

In this Section, the questions posed at the beginning of the Chapter are answered one-by-one by exploiting the new global model described in Section 4.1.

4.2.1 The impact of the introduction of the new support

At first, the model is exploited to assess the impact of the introduction of the new support of the batteries. The temperature limits of the vacuum test performed by J.P. Nöel [2] were estabilished by considering the minimum temperature attended by the batteries during the **Cold** case, while heaters are not installed. However, this limit was estimated with the old model, where the new support was not introduced.

So, by following the same logical path, a simulation without heaters, and also without any insulation of the batteries[6] was performed. The results are shown in Figure 4.6. The minimum temperature experienced by the batteries is about -10^oC, while the one forecast by the old model was -15^oC [1].

So, in conclusion, the only introduction of the new support has a positive impact on the BAT subsystem, but, indeed, it is not able to fix the BAT issue without any other solution.

[4] For sake of completeness, in ESATAN it is directly provided the absorbed solar power, so that to get the incident one, it is enough to divide the absorbed by the absoptance of the solar cells.

[5] A parallel of two resistances of 4.7Ω is exploited.

[6] i.e., with aluminium spacers, without aluminium tape on the surface support, and without any insulator between batteries and support

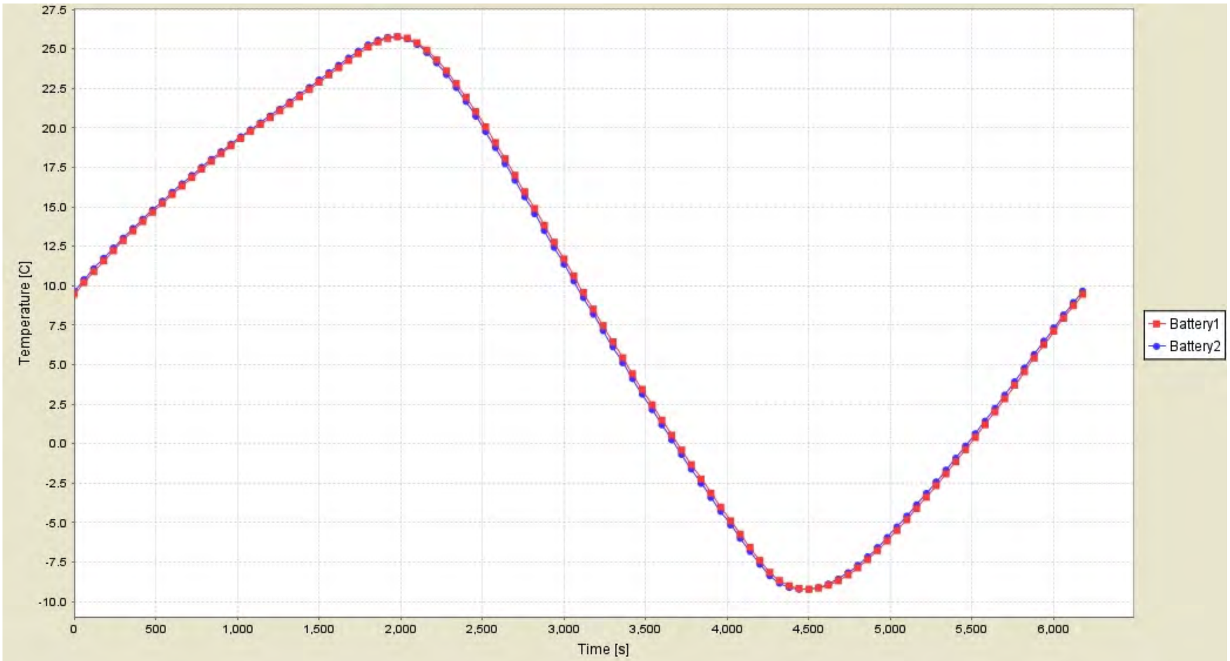

Figure 4.6: Impact of the introduction of the new support on the temperature of the batteries during **Cold** case.

4.2.2 The new design of the BAT subsystem

The effect of the introduction of the new design of the BAT subsystem is shown in Figure 4.8. During the whole **Cold** case, the temperature of the batteries is almost constant, and close to 10^oC, and heaters are never supplied, which means that this solution is not only satisfactory under the thermal point of view, but also under the power saving one. Indeed, heaters cannot be removed, since the thermal simulations have to be considered with their margin of error (as discussed in Chapter 5).

However, if the vacuum test on the new BAT design provides optimistic results, the cold case BAT issue will be considered solved.

4.2.3 The transistor issue

The evolution of the temperature of the transistor during the **Hot2** case is shown in Figure 4.7.

As already discussed in Chapter 3, the temperature estimated by *ESATAN* is the temperature on the PCB, $T_t^{(PCB)}$, in correspondence of the joint with the transistor. The real temperature of the transistor is obtained by means of its junction to case resistance, $R_{\theta JC} = 10\frac{^oC}{W}$ [30], with the relation:

$$T_t = T_t^{PCB} + R_{\theta JC} Q_t \tag{4.6}$$

where Q_t is the power dissipated by the transistor.

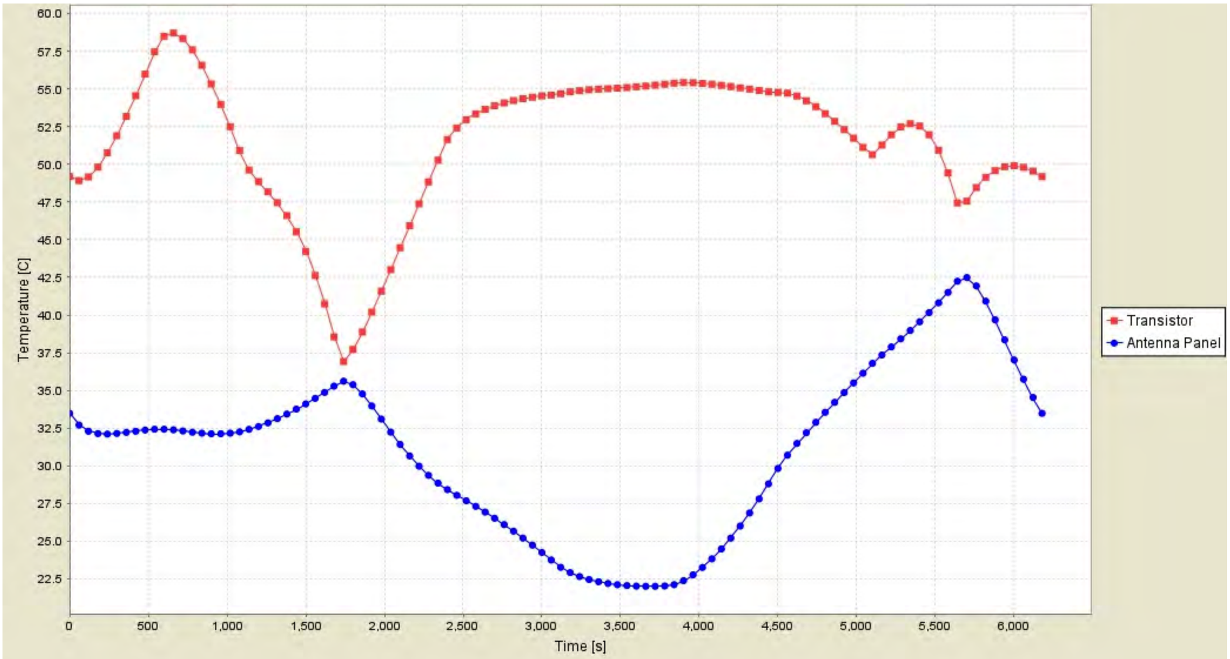

(a) Temperature

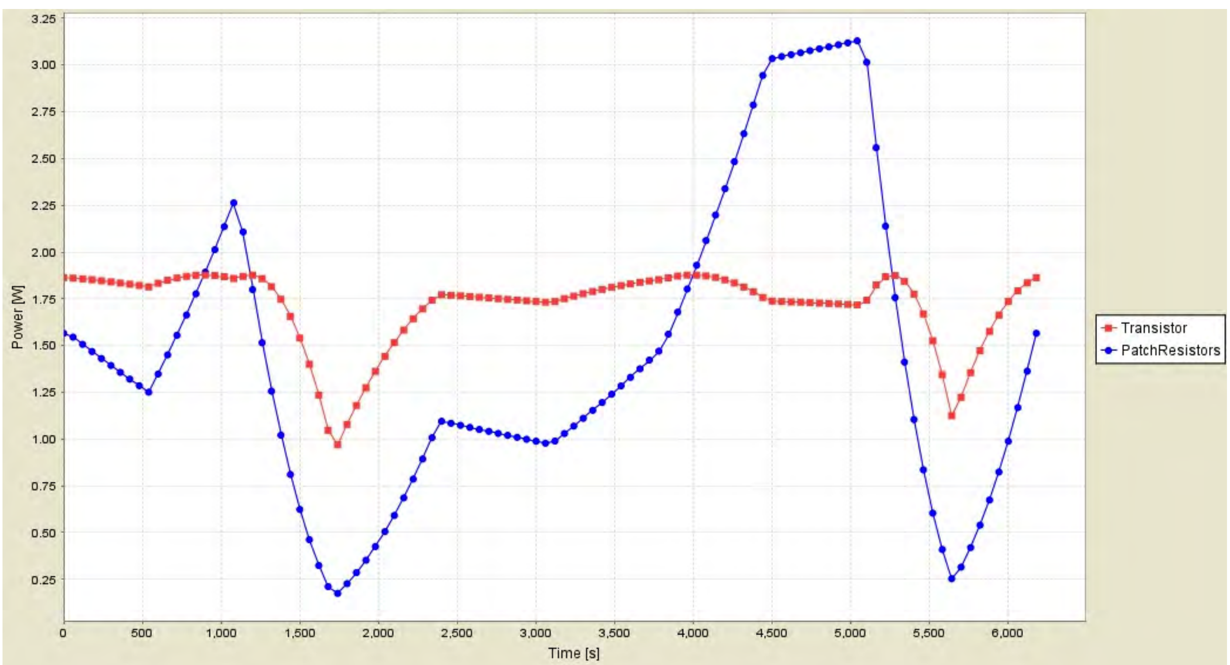

(b) Power

Figure 4.7: Temperature of the transistor and antenna panel, and power dissipated by the transistor and patch resistors during the **Hot2** case.

The maximum $T_t^{(PCB)}$ estimated (Figure 4.7) is about 60^oC and it occurs when the dissipation is almost maximum ($Q_t = 1.88W$), so that the maximum temperature of the transistor forecast is about 100^oC, which is within the operational range of the transistor itself is $[-65, 200]^oC$.

On the other hand, the maximum $T_t^{(PCB)}$ is even below the value forecast by L. Jacques [1] (i.e., 67^oC), because of the over-sizing of the strap discussed in Chapter 3.

So, if the eventual development test of the thermal strap provide optimistic results, also this issue will be considered solved.

4.2.4 Respect of the requirements

The mean, as well as the maximum and minimum temperatures of the different subsystems are represented in Figures 4.8 and 4.9 for the **Cold** and the **Hot1** cases, respectively.

Most of them are within the limits imposed by the requirements of Table 1.1, even by adding an incertitude margin of 15^oC to the forecast ranges, as suggested by the ECSS [20]. The only exception is the COM amplifier, which achieves a maximum temperature of about 80^oC during **Hot1** case (and so 95^oC with incertitude margins). This issue was already underlined by L. Jacques [1], but it is still far to be solved, since neither the model nor the location of the amplifier are actually known.

Furthermore, in order to ease the readability of the Figures, the temperature of the antennas is not represented. Because of their feeble emittance to absorptance ratio (see Table 4.1) and their poor thermal inertia, their range is extremely wide, and it achieves the highest temperatures of the satellite (i.e., $[-20, 200]^oC$). However, under the thermal point of view, it is not problematic (they are out of the satellite and copper melts above 1000^oC [15]). Indeed, it could represent a issue for the COM subsystem.

4.2.5 Temperature range of the Spacecraft

The temperature range of the spacecraft is exploited to determine the temperature levels that have to be imposed during the protoflight test (Chapter 5). Indeed, the hotspots (like COM amplifier, EPS transistor, or antennas) do not have to be considered to this purpose, since they are not representative of the global thermal status of the satellite, or because they require internal power dissipation to reach those levels.

For these reasons, the minimum and maximum temperature of the external skin are considered as the spacecraft range, since they are the most critical values, and they are strictly related to the temperatures of each subsystem.

So, by considering Figures 4.8 and 4.9, the range deduced by the numerical model (i.e., without margins) is $[-25, 55]^oC$.

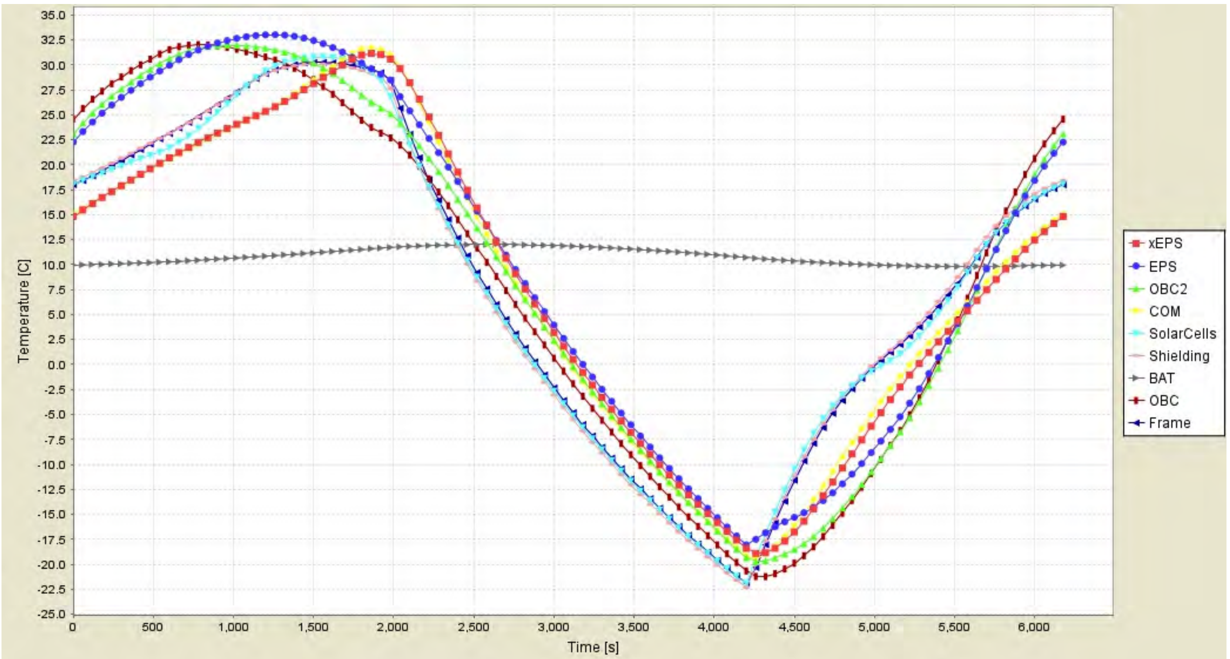

(a) Mean temperatures

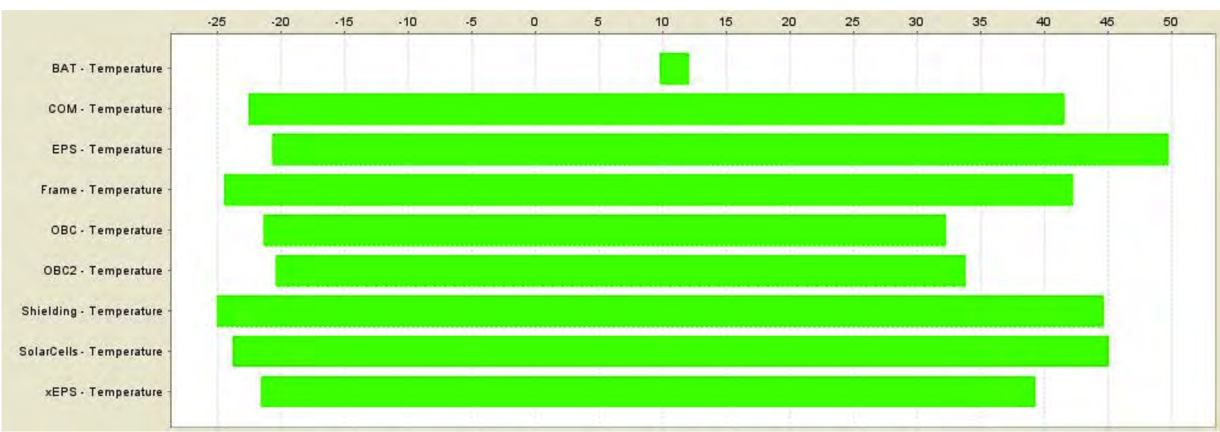

(b) Max/Min temperatures

Figure 4.8: **Cold** case: mean temperature of the subsystems during the orbit and their temperature limits.

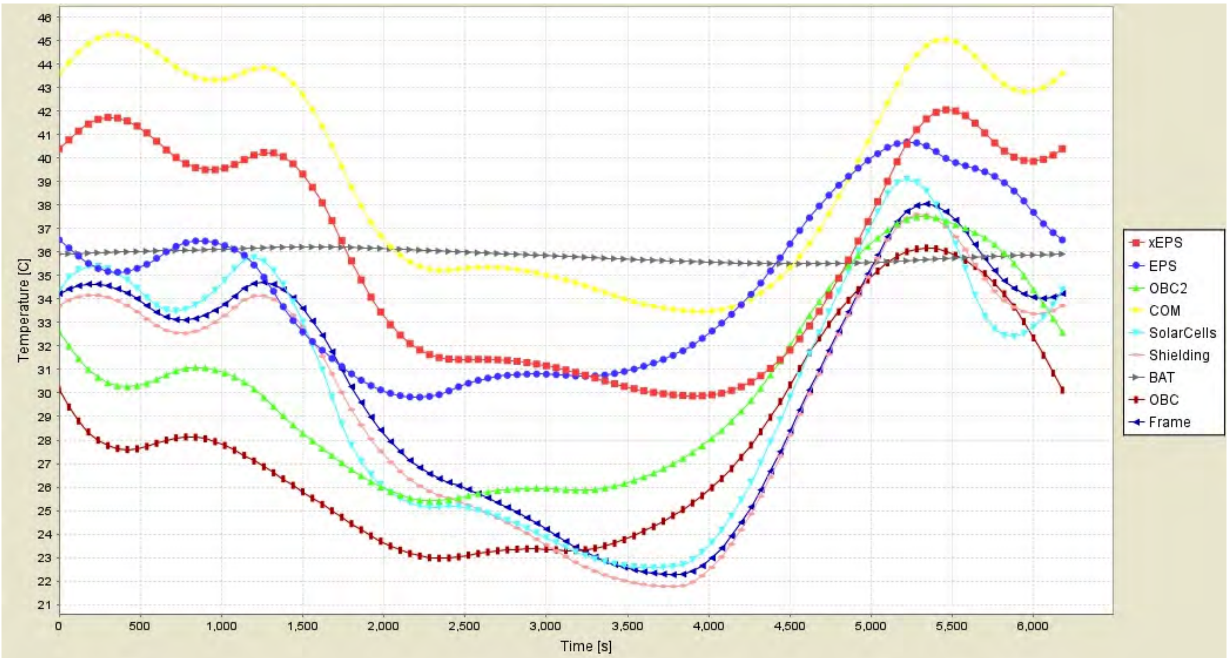

(a) Mean temperatures

(b) Max/Min temperatures

Figure 4.9: **Hot1** case: mean temperature of the subsystems during the orbit and their temperature limits.

Summary

After a brief description of the new global model, the results of its simulations were presented.

According to these results, the new design of the BAT subsystem appears to be adequate, and, if the vacuum test of June will provide optimistic results, this issue will be considered closed.

Concerning the transistor issue, the design of the strap has provided optimistic results, too.

Indeed, an accurate sensitivity analysis of this model was not performed both because of a lack of time, and because it was already argued in the work of L. Jacques [1], and the most important changes in the design concern the BAT subsystem, whose model was accurately studied in Chapter 2. Furthermore, a geometric modelling of the strap is missing, too (actually it is only modelled with a GL).

The COM amplifier issue has still to be solved, and its hotspots represent an important hot-case issue. However, before fixing this issue, it is necessary that the design of the COM is completed, and that more data about the location and the nature of the amplifier are available.

Chapter 5

Procedure for the protoflight testing

The Cubesat Specification Requirements [40] states that:

> *"All CubeSats shall survive protoflight testing as outlined by the LV[1] provider. [...] Protoflight testing will be performed at developer facilities. [...] CubeSats SHALL NOT be disassembled or modified after protoflight testing. Disassembly of hardware after protoflight testing shall require the developer to submit a DAR[2] and adhere to the waiver process prior to disassembly. Additional testing shall be required if modifications or changes are made to the CubeSats after protoflight testing."*

For this reason, a protoflight test procedure for OUFTI-1 is discussed in this Chapter.

At first, a general description of the protoflight testing is provided. Then, the specific case of OUFTI-1 is argued.

5.1 Protoflight testing philosophy

According to the ECSS, the space validation of a spacecraft is performed by means of [20]:

Qualification tests, whose objective is [20] *"the formal demonstration that the design implementation and manufacturing methods have resulted in hardware and software conforming to the specification requirements."*

Acceptance tests, whose purpose is [20] *"to demonstrate conformance to specification and to act as quality control screens to detect manufacturing defects, workmanship errors, the start of failures and other performance anomalies, which are not readily detectable by normal inspection techniques."*

For these reasons, qualification tests exceed the maximum predicted levels (either thermal or mechanical) by a factor of safety which assures that, even with the worst combination

[1] Launch Vehicle (LV).
[2] Deviation Wavier Approval Request (DAR).

of test tolerances, the flight levels shall not exceed the qualification test levels, and, thus, these tests are performed on one or more Qualification Model (QM), which are not eligible for flight (prototype approach).

On the other hand, acceptance tests have to demonstrate the adequacy and readiness of an item for delivery and subsequent usage, so that they are directly performed on the Flight Model (FM), and, thus, they do not have to create conditions that exceed safety margins or cause unrealistic modes of failure.

However, the development of QMs is not always affordable by the budget of the project, so that the FM is often the only exemplar of the spacecraft (or of some of its subsystems). To overcome this issue, the **Protoflight testing** philosophy is exploited. In this way, the qualification of the spacecraft is directly performed by testing the FM.

Essentially, protoflight testing consists in a combination between qualification and acceptance testing, in the sense that [20]:

- *"protoflight test levels: as qualification margins [...],*
- *protoflight test durations: as acceptance durations."*

In the context of a qualification (and protoflight) testing procedure, the thermal test required are:

- thermal vacuum
- thermal cycling (at ambient pressure)

Nonetheless, they can also be performed together in a so called **thermal vacuum cycling** test. Since this procedure will be exploited for OUFTI-1, the next section is devoted to detailing it.

5.1.1 The thermal vacuum cycling test

The procedure of the thermal vacuum cycling test is shown in Figure 5.1, and the symbols are clarified in Table 5.1.

The sequence of the test is (freely adapted from [20]):

1. Initial functional and performance test are performed in the chamber at ambient temperature ($T_{AMBIENT}$).
2. The specimen is switched-off and the pressure decreased.
3. At a pressure of $10^{-4} hPa$, the temperature is increased up to the maximum non-operating level (T_{NO-max}).
4. After a dwell time t_E, the temperature is decreased to the maximum (hot) start-up level ($T_{SU-high}$) and then the temperature stabilized at the high operating temperature (T_{Q-max}).

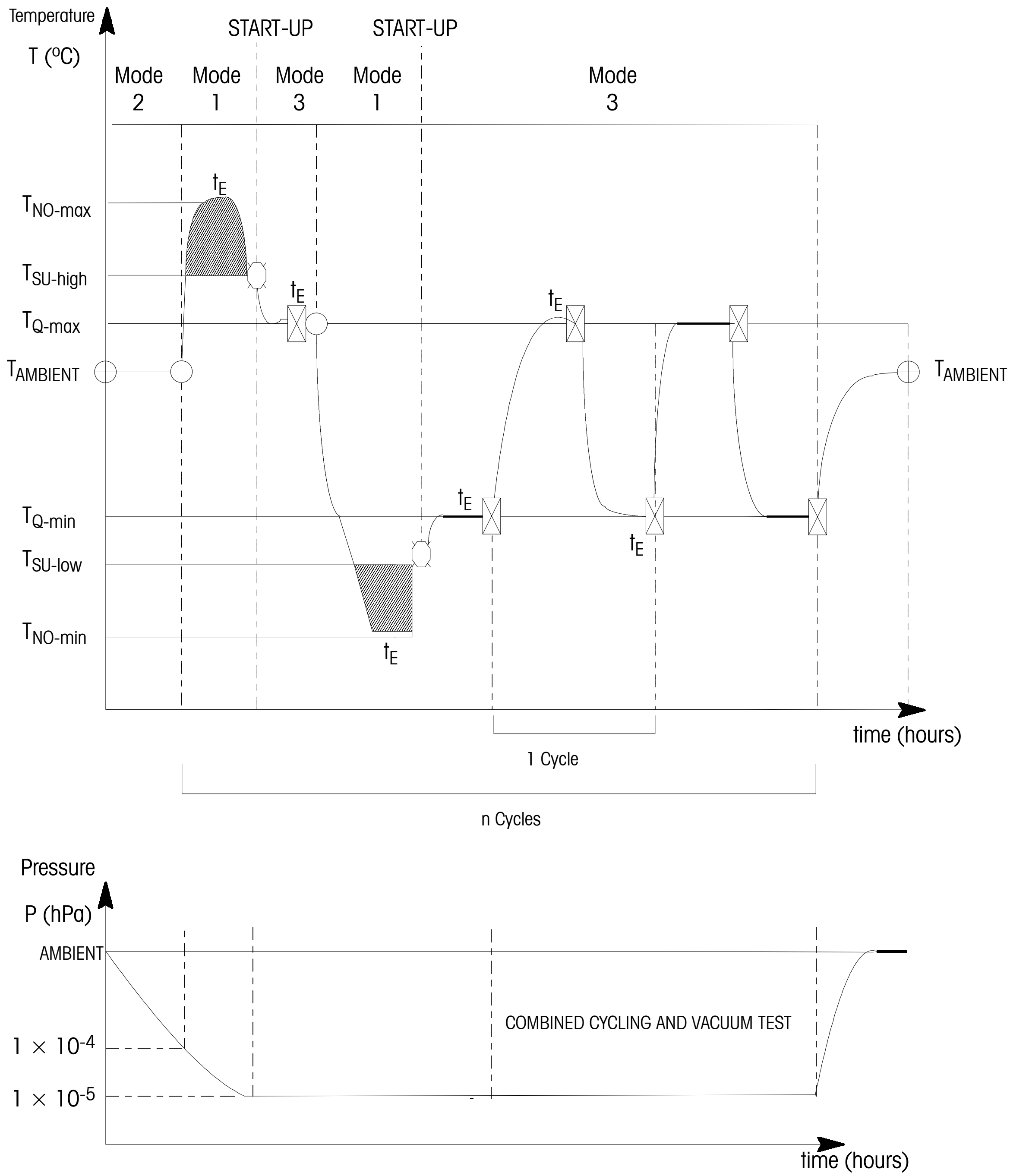

Figure 5.1: Thermal vacuum cycling test, from [20].

Symbol	Description
T	Test item temperature
$T_{AMBIENT}$	Ambient temperature
$T_{NO\text{-}max}$	Maximum non-operating temperature (highest design temperature for the equipment to survive not powered)
$T_{NO\text{-}min}$	Minimum non-operating temperature (lowest design temperature for the equipment to survive not powered)
$T_{SU\text{-}high}$	Maximum start-up temperature (highest design temperature of the equipment, at which the equipment can be switched on)
$T_{SU\text{-}low}$	Minimum start-up temperature (lowest design temperature of the equipment, at which the equipment can be switched on)
$T_{Q\text{-}max}$	Maximum qualification temperature (highest design temperature at which the equipment demonstrates full design ability)
$T_{Q\text{-}min}$	Minimum qualification temperature (the lowest design temperature at which the equipment demonstrates full design ability)
P	Pressure
MODE 1	Functionally inert (test item not energized). Normally applicable to the non-operating condition.
MODE 2	Partially functioning. Conditions as detailed in applicable design specifications, but normally applicable to conditions during launch.
MODE 3	Fully functioning (test item fully energized and fully stimulated). Normally applicable to conditions during orbit.
$\oplus$	Initial and final "functional and performance test"
$\boxtimes$	Intermediate reduced functional and performance test
t_E	Dwell time
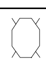	Switch-on (Start-up)
$\bigcirc$	Switch-off

Table 5.1: Legend and symbols for Figure 5.1, from [20].

5. After the time t_E, the functional and performance test are performed.
6. The specimen is switched off and the temperature decreased and maintained at the minimum non-operating temperature (T_{NO-min}) during a time t_E.
7. The temperature is increased to the minimum (cold) start-up temperature (T_{SU-low}) and the specimen switched on.
8. When stabilized at the low operating level (T_{Q-min}), and after the time t_E, the functional and performance test are performed.
9. The specimen is switched off.
10. The prescribed number of cycles is performed between T_{Q-max} and T_{Q-min}, during a time t_E (for each half-cycle).
11. Functional and performance test are performed during the last cycle.
12. The temperature and pressure are raised to ambient conditions ($T_{AMBIENT}$) and the final functional test performed.

Furthermore, functional tests have to be performed before and after the vacuum test.

The determination of the temperature levels is based upon the numerical simulations, and the margins to add are represented in Figure 5.2 (qualification limits). Then, at least 4 complete cycles have to be performed and the dwell time is $t_E = 2h$ (acceptance duration).

5.2 OUFTI-1 Protoflight test procedure

The objective of the qualification (and, consequently, protoflight) testing, and the thermal vacuum cycling sequence were discussed in Section 5.1. However, to complete the test procedure, it is still necessary to answer to the following questions:

- What is the test facility?
- Which functional and performance test shall be done?
- How is the spacecraft positioned and fastened? And how is the temperature imposed?
- What are the temperature limits?
- How long it takes the stabilisation of the temperature?
- How many thermocouples? And where?

So, for sake of clarity, a Subsection is devoted to each one of these points.

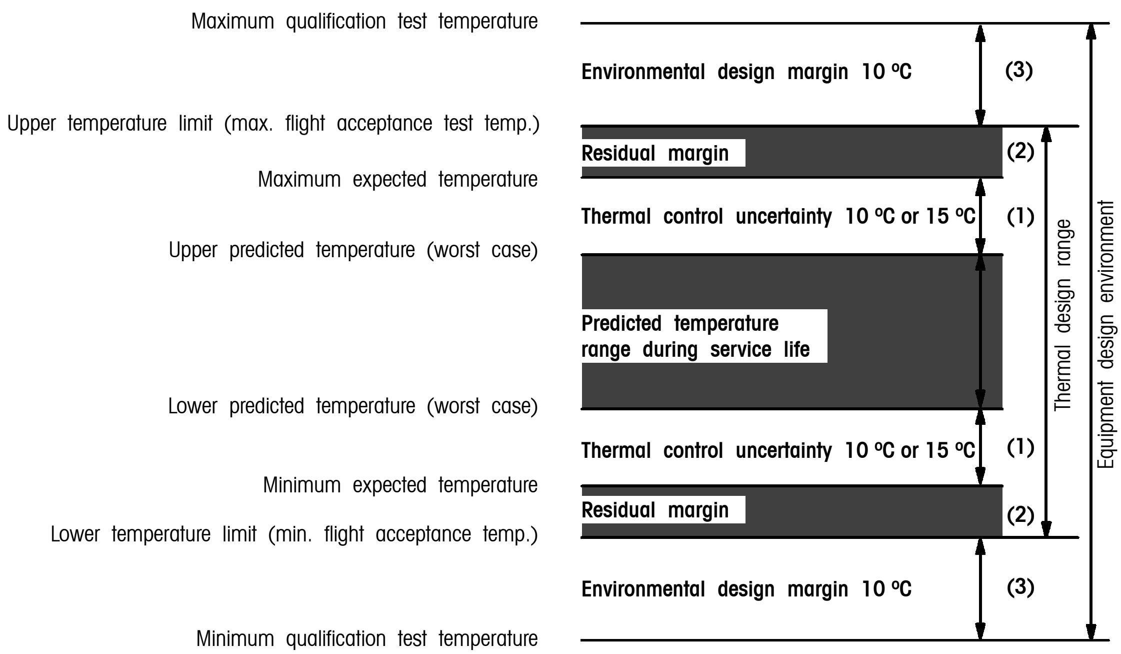

Figure 5.2: Temperature limits and margins definitions, according to the ECSS [20].

Test facility

As for the new vacuum test of the BAT subsystem, the test facility is the *Focal 0.25* of the CSL (see Figure 2.32).

Functional and performance test

The functional tests to perform are:

D-STAR transmitting and receiving mode. However, since the CubeSat is inside the vacuum vessel, communication through the antennas is not possible, and all the signal of the COM shall pass through the USB. Nevertheless, during transmission, the amplifier shall be used normally and its temperature shall be carefully monitored especially during the hot case.

Beacon transmission of housekeeping parameters.

AX.25 reception and transmission of tele-command and telemetry data.

BAT TCS in the cold case, the temperature of the batteries shall be kept in their operational range.

Unlucky, according to the EPS team, it is not possible to supply the dissipation system[3] by means of the USB once that OUFTI-1 is integrated, so that its proper functioning cannot

[3] i.e., transistor and patch resistors on the antenna panel.

be tested. For this reason, another development test devoted to this system is strongly advised.

Furthermore, the fact that the COM signals have to pass through the USB (and so just the binary signals) does not allow to test the amplification, the (de)modulation and the passage of the signals in the antennas, which are the most delicate aspects of the COM. So, another test devoted to this purpose has to be performed.

Finally, it is necessary to implement a mode "test" on the Pumpkin OBC which allows to switch on and off the satellites (see the test sequence of Section 5.1.1). Actually it is not possible, but, according to the EPS and OBC teams, it is feasible.

Temperature limits

The temperature limits are determined by considering Figure 5.2:

- the range of temperature determined by the thermal analysis is (see Section 4.2.5):

$$T_{SIM-min} = -25^oC \qquad T_{SIM-max} = +55^oC \tag{5.1}$$

- by adding the safety margin of 15^oC, the predicted temperature becomes:

$$T_{min} = -40^oC \qquad T_{max} = +70^oC \tag{5.2}$$

- by adding the qualification margin of 10^oC, the qualification operational temperature to impose is:

$$T_{Q-min} = -50^oC \qquad T_{Q-max} = +80^oC \tag{5.3}$$

- then, according to [20], the start-up hot and cold temperatures are normally equivalent to the corresponding non-operational temperatures, which are generally computed by adding a margin of 10^oC to the operational limits:

$$T_{SU-low} = T_{NO-min} = -60^oC \qquad T_{SU-high} = T_{max} = +90^oC \tag{5.4}$$

To check if the order of magnitude of these limits is correct, they are compared with the ones of other CubeSats in Table 5.2.

5.2.1 Positioning of OUFTI-1 in the vacuum vessel

The typical set-up of a vacuum test is shown in Figure 5.3. The temperature is imposed by the *temperature controlled mounting frame* and the heat is transferred to the structure by means of radiation and/or conduction through a mounting interface. An example of a thermally conductive and a thermally insulating (i.e., heat is essentially provided by radiation) interfaces is shown in Figure 5.4.

Conductive interface has the main advantage to reduce the stabilisation time and to improve the uniformity of the temperature of the satellite, so that it is advised. On the other hand, its drawback is that it requires the conception of a more complicated interface, which, actually, is not designed, yet.

CubeSat	$T_{SIM-min}$	$T_{SIM-max}$	T_{Q-min}	T_{Q-max}	**Reference**
OUFTI-1	-25	55	-50	80	
SwissCube	-	-	-50	70	[41]
AAU	-	-	-30	85	[42]
compass one	-45	65	-	-	[6]
CP3	-30	50	-	-	[43]
BillikenSat-II	-20	35	-	-	[44]

Table 5.2: Comparison between the temperature limits of OUFTI-1 and other CubeSats. All the temperatures are in $[^oC]$. For compass one, the temperature of the structure is considered.

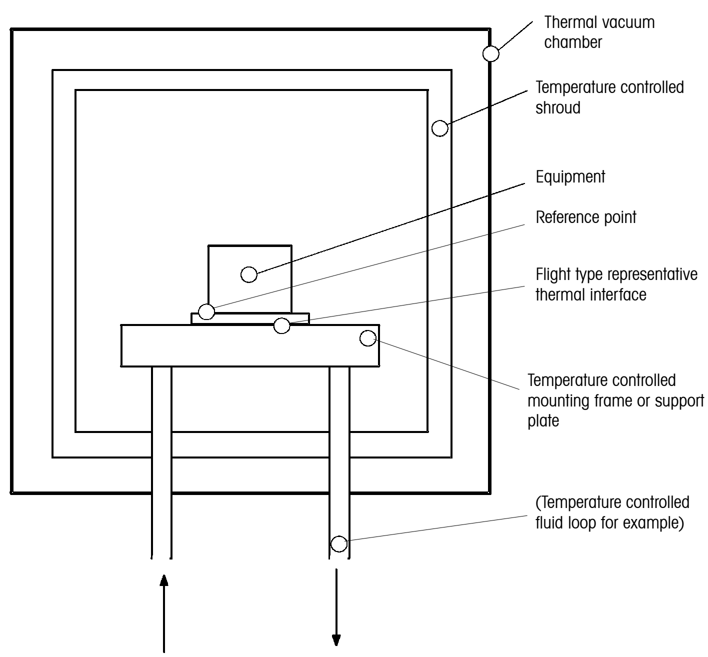

Figure 5.3: Thermal vacuum test set-up, from [20].

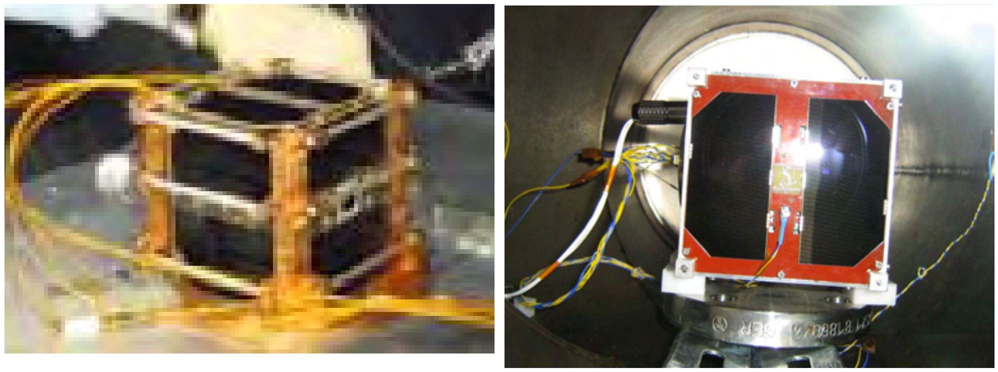

(a) SwissCube. Thermally conductive interface.

(b) compass one. Insulating interface.

Figure 5.4: Mounting interface of SwissCube (from [45]) and compass one (from [46])

5.2.2 Stabilisation of the temperature

Functional and performance test shall be started once that the temperature of the spacecraft is stabilised. To this purpose, the ECSS states [20]:

> *"During system level tests, performance verification testing may be started when the rate of change is below 1^oC within a time period equal or near the time constant of the spacecraft."*

For this reason, the time constant of OUFTi-1 has to be estimate. Indeed, it is mainly function of the fastener system, which is still not developed. So, in order to perform a pessimistic estimation, it is considered that the spacecraft is simply leaned on the temperature-regulated panel, and just the four feet of the $+z$ face (see Figure 4.1(a)) are in contact with it[4].

Because of the higher level of complexity of the OUFTI-1 model respect to the BAT model, the estimation of the time constant cannot be performed as described in Appendix B, so that, according to [42], the value of the stabilisation at 33% is considered[5] (i.e., the difference between the temperature of the satellite and the imposed one is less than the 33% of the initial value).

As shown in Figure 5.5, apart from the BAT[6], the temperature of all the other subsystem is stabilised in less than $1h$. However, the importance of a good contact between feet and regulated panel is extremely important. In fact, as shown in Figure 5.6, the temperature of the feet themselves strongly depends on this parameter (in Figure 5.5

[4]This face was considered since the feet of the $-z$ face have the deployment springs and the switch of the Cubesat, so that their contact with the temperature-regulated panel is not feasible.

[5]In a simple system, the convergence after $t = \tau$ is about the 36% (i.e., $e^{-1} \simeq 0.36$).

[6]Since the design of the BAT subsystem is aimed at insulating the support, it is not necessary to wait too long for its stabilisation at 33%, since the fact that its temperature does not drop quickly can be considered as a performance test of the BAT TCS design.

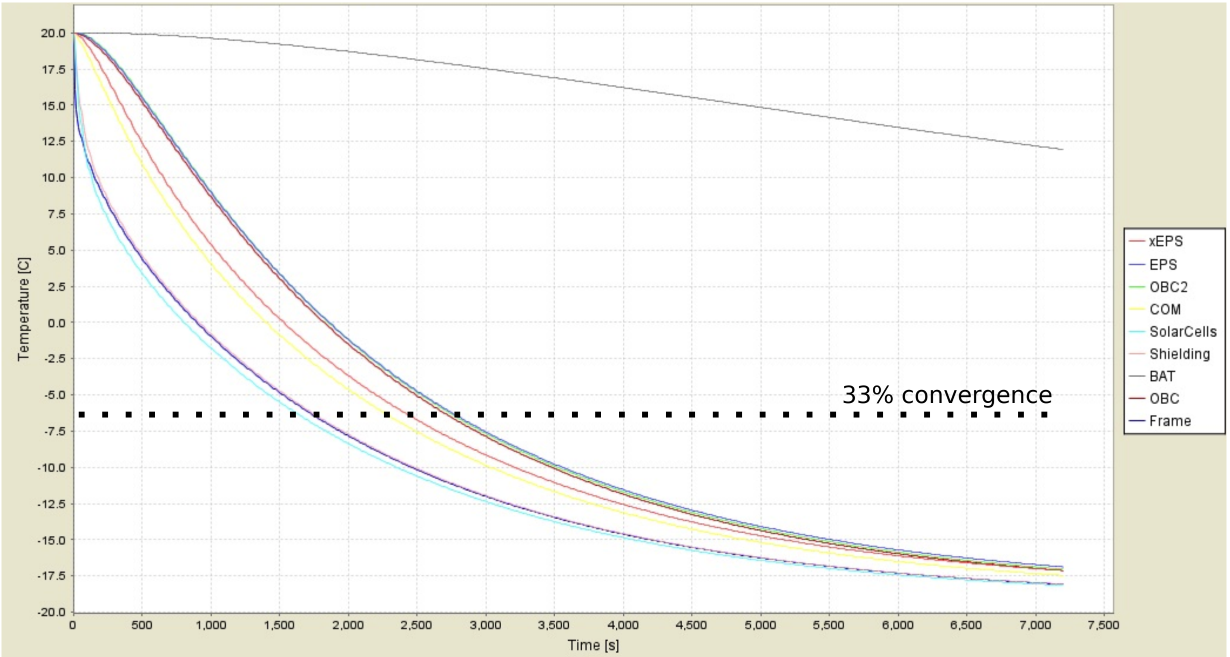

Figure 5.5: Estimation of the time constant of OUFTI-1. The temperature imposed is -20^oC, while the initial temperature is 20^oC, so that the convergence at 33% is reached when $T = -6.6^oC$.

$GL = 1\frac{W}{K} \simeq \frac{GL_{perfect\ contact}}{2}$). For this reason, the design of an adequate conductive interface is strongly advised.

5.2.3 Thermocouples

As stated in the introduction of the Chapter, the spacecraft cannot be disassembled after the test, so that it is not possible to place any thermocouple into OUFTI-1. So, one thermocouple will be placed at the center of the five faces provided with solar cells (but not on them) and one on the pumpkin frame on the antenna panel face[7]. Furthermore, when functional tests are performed, housekeeping data can be monitored and collected, too.

However, this test is not aimed at providing data for a detailed correlation, so that the lack of data about the interior temperature distribution is not critical.

Then, a thermocouple has to be placed on the reference point, which is defined as [20]:

> *"the physical point located on the equipment providing a simplified representation of the equipment thermal status"*

The best candidate location is on the Pumpkin frame, below the antenna panel, so that the thermocouple of its face is retained as reference point. During the test, the

[7] Apart from the anodized rails, it is the only part of the pumpkin frame which is not covered by the aluminium panels.

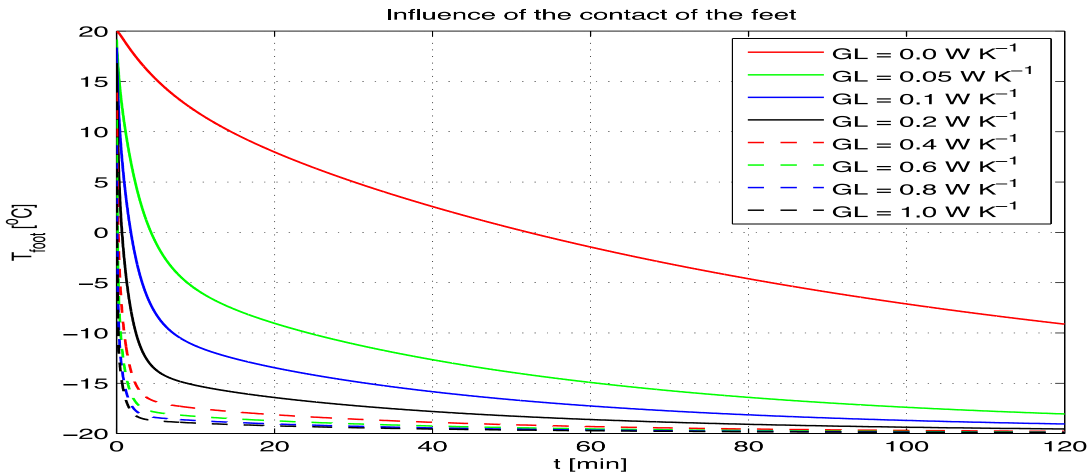

Figure 5.6: Temperature of a foot of OUFTI-1 in contact with the temperature regulated panel. Their good contact conductance is extremely important to reduce the time constant of the system.

shroud temperature is controlled by the operator in such a way that the reference point temperature follows the thermal cycling specification curve.

Summary

The protoflight testing is a general requirement for all the CubeSats. In this Chapter, the thermal vacuum cycling test was described, and all the parameters necessaries to its realisation were discussed.

Concerning the test equipement, an adequate copper interface has to be designed and manufactured.

However, before proceeding with this test, the BAT test has to be performed, and an eventual development test of the strap, too. Furthermore, the COM amplifier issue is still open. For these reasons this test is still far from being realised.

Chapter 6

Conclusions

Three main thermal issues were outlined in the works of L. Jacques [1] and J.P. Nöel [2]:

1. too cold temperature of the batteries during the cold case,
2. too high and detrimental power dissipation of the transistor,
3. hotspot due to the COM amplifier.

In this dissertation, the first two of them were discussed and design solution were proposed.

Concerning the BAT issue, the analysis of the vacuum test performed in 2010 revealed that the actual design was not able to keep the temperature of the batteries above the 0^oC. For this reason, new design solutions were envisaged, and they proved that the only insulation of the batteries was extremely inefficient. So, the most suitable solution appeared to be the insulation of the whole BAT subsystem by means of:

- POM spacers to reduce the conductive dissipation,
- aluminium tape on the external surface of the support to improve the radiative insulation.

Though the optimistic numerical simulations, the validation of this solution still requires the realisation of a vacuum-development test, which is scheduled for the 14 June 2011.

A feasibility study of a solution involving PCM was envisaged in Chapter 2, too. This solution proved to be extremely interesting under the power saving point of view, but not under the mass efficiency one. However, the advanced state of the OUFTI-1 project does not allow its implementation.

Then, the design of the thermal strap was performed in Chapter 3. The component was sized by considering the worst operational conditions of the transistor. Also in this case, numerical simulations provided optimistic results, but a development test (not discussed in the dissertation) is advised to validate the design.

Chapter 4 was devoted to the description of the new thermal numerical model of OUFTI-1 and of the results of its simulations. No new issues were identified, but, on the contrary, the new design of the BAT subsystem and of the thermal strap proved to be able to fulfil the requirements of Table 1.1.

Finally, in Chapter 5, a test procedure for the thermal vacuum cycling testing was proposed. Such procedure was developped according the protoflight testing philosophy of the ECSS [20].

According to me, the next tasks of the OUFTI-1 TCS are:

- to perform the BAT test described in Section 2.7.2, analyse and correlate its results,
- to manufacture the thermal strap, and realize its eventual development test,
- to update the design of the BAT subsystem and of the thermal strap against eventual issues that might be outlined by these tests,
- to solve the COM amplifier issue, as more detailed data are available,
- to perform the protoflight test described in Chapter 5.

Appendix A

Technical data of the batteries

Item		Specifications
Nominal Capacity (at 25^oC)		$1.5Ah$
Nominal Voltage		$3.7V$
Cut-off Voltage		$2.7V$
Charge Condition	Max. Current	$3.0A$
	Voltage	$4.2V$
Cycle life (80 % of the capacity)		> 500
Operating Temperature	Charge	$0 \sim 40^oC$
	Discharge	$-20 \sim 60^oC$
Dimensions		$6.5 \times 37.5 \times 69.5mm^3$
Weight		$32g$

Table A.1: Technical data of the batteries *Kokam SLB603870H* (from [4], [21]).

Appendix B

Computation of the time constant of the BAT subsystem

Consider an isothermal object with mass m, specific heat C_s and initial temperature $T(t = 0) = T_i$. At the time $t = 0^+$, this object starts to exchange conductively with a node at the constant temperature T_∞, through a thermal conductance GL.

The temperature of the object in function of time is dominated by the differential equation of the first order with constant coefficients:

$$m\ C_s \frac{d\ T}{dt} = GL\ \ (T_\infty - T) \tag{B.1}$$

whose solution is:

$$T(t) = T_\infty + (T_i - T_\infty)\, e^{-\ \frac{t}{\tau}} \tag{B.2}$$

where $\tau \doteqdot \frac{m\ C_s}{GL}$ is the time constant of the system.

However, this reasoning is no more valid if radiative exchange occurs, so that it is not rigorous for the BAT subsystem. Nevertheless, it allows to perform an approximated estimation.

So, to compute the τ of BAT, the following procedure is employed:

- the logarithm operator is applied to the Equation B.2:

$$\log{(T - T_\infty)} = \log{(T_i - T_\infty)} - \frac{t}{\tau} \tag{B.3}$$

- the constant $B = \log{(T_i - T_\infty)}$, and the variable $X = -\log{(T - T_\infty)}$ are defined, so that Equation B.3 becomes:

$$t = \tau\ X + B \tag{B.4}$$

- in the numerical model, a step function is imposed to the temperature-regulated panel, and the numerical solution $T^{(i)}$ (temperature of the batteries) is evaluated at the time steps $t^{(i)}$, $i = 1, ..., N$. Analogously to the previous step, the sampled $X^{(i)}$ are defined as $X^{(i)} = -\log\left(T^{(i)} - T_\infty\right)$, $i = 1, ..., N$,

- The time constant is evaluated as the slope of the regression curve [23]:

$$\tau = \frac{N \sum_i X^{(i)} t^{(i)} - \sum_i X^{(i)} \ \sum_i t^{(i)}}{N \sum_i X^{(i)\ 2} - \left(\sum_i X^{(i)}\right)^2} \tag{B.5}$$

Appendix C

List of PCM materials

Material	Melting Point (°C)	Heat of Fusion (kJ/kg)
n-Eicosane ($C_{20}H_{42}$)	37	246
Polyethylene glycol 600 [$HO(CH_2CH_2O)_nH$]	20–25	146
Nitrogen pentoxide (N_2O_5)	30	320
Phosphonium chloride (PH_4C1)	28	752
Dibasic sodium phosphate ($Na_2HPO_6 \bullet 12H_2O$)	37	279
Sodium sulfate ($Na_2O_4 \bullet 10H_2O$)	31	215
Glycerol [$C_3H_5(OH)_2$]	18	199
Calcium chloride ($CaC1_2 \bullet 6H_2O$)	29	170
p-Xylene [$C_6H_4(CH_3)_2$]	16	164
Sodium chromate ($Na_2CrO_4 \bullet H_2O$)	23	164
n-Undecane ($C_{11}H_{24}$)	–25	141
n-Dodecane ($C_{12}H_{26}$)	–12	211
n-Tridecane ($C_{13}H_{28}$)	–6	155
n-Tetradecane ($C_{14}H_{30}$)	6	228
n-Hexadecane ($C_{16}H_{34}$)	17	237
n-Heptadecane ($C_{17}H_{36}$)	22	213
n-Octadecane ($C_{18}H_{38}$)	28	244
n-Nonadecane ($C_{19}H_{40}$)	32	187
n-Octacosane ($C_{28}H_{58}$)	62	253
1-Tetradecanol [$CH_3(CH_2)_{12} \bullet (CH_2)OH$]	38	230
Acetic acid (CH_3COOH)	17	187
Water	0	333

Table C.1: Typical PCMs in the Range of -25 to $+62^oC$, from [12].

Appendix D

Geometrical data of the transistor

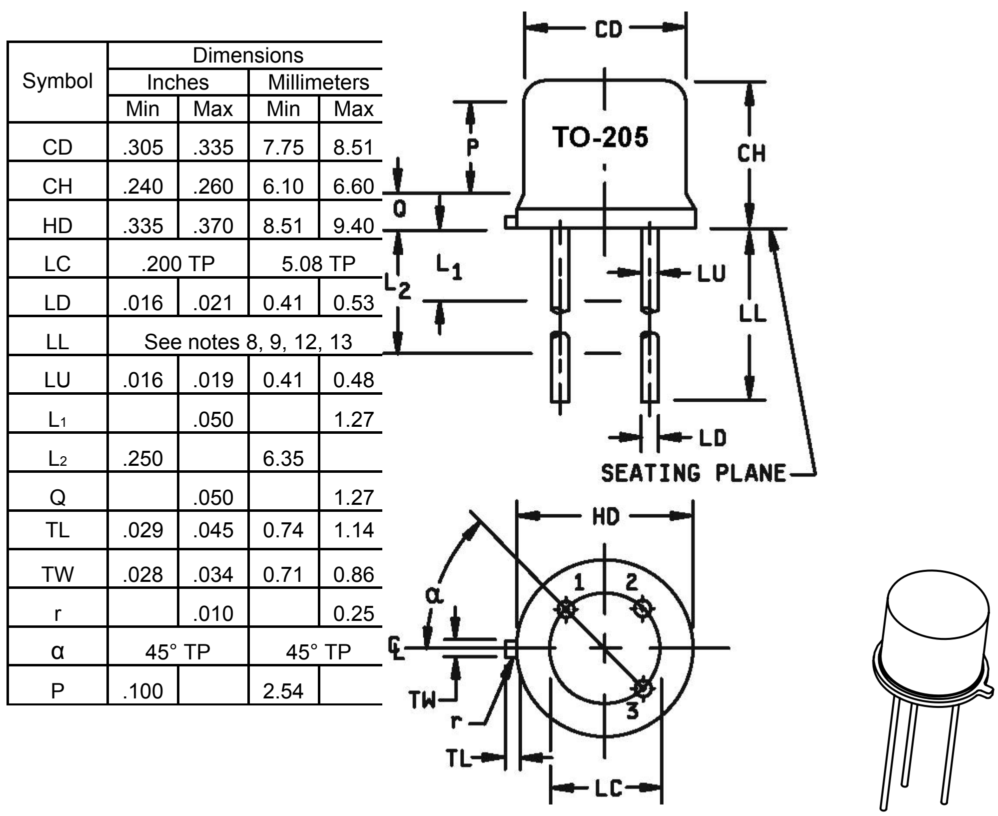

Symbol	Dimensions			
	Inches		Millimeters	
	Min	Max	Min	Max
CD	.305	.335	7.75	8.51
CH	.240	.260	6.10	6.60
HD	.335	.370	8.51	9.40
LC	.200 TP		5.08 TP	
LD	.016	.021	0.41	0.53
LL	See notes 8, 9, 12, 13			
LU	.016	.019	0.41	0.48
L_1		.050		1.27
L_2	.250		6.35	
Q		.050		1.27
TL	.029	.045	0.74	1.14
TW	.028	.034	0.71	0.86
r		.010		0.25
α	45° TP		45° TP	
P	.100		2.54	

(a) Geometrical data (b) 3D view

Figure D.1: Geometry of the transistor, from [30].

Bibliography

[1] L. Jacques. *Thermal Design of the Oufti-1 nanosatellite.* Master's thesis, Université de Liège, 2008-2009.

[2] J.P. Nöel. *Thermal issues settlement and test procedure investigation of OUFTI-1 nanosatellite.* Master's thesis, Université de Liège, 2009-2010.

[3] S. Galli. Mission design for the cubesat oufti-1. Master's thesis, Université de Liège, 2007-2008.

[4] Kokam Co., Ltd. *Cell Specification Data. SLB603870H.*

[5] Battery University. *Charging at High and Low Temperatures.* `http://batteryuniversity.com`.

[6] compass one. *Phase B documentation.* Technical report, FH Aachen.

[7] F. Molliet. *Phase C. SwissCube Thermal Analysis.* Technical report, École Polytechnique Fédérale de Lausanne, 2008.

[8] Delfi-c3. `http://www.delfic3.nl/`.

[9] Minco. *Flexible Heaters Design Guide.*

[10] Sheldahl. *Polyester Netting. Product Bulletin.*

[11] B. Sisterman. *Battery Protection Module.* Technical report, Université de Liège, 2010-2011.

[12] D.G. Gilmore. *Spacecraft Thermal Control Handbook. Volume I: Fundamental Technologies.* The Aerospace Press, 2002.

[13] *Aluminum 7075-T6; 7075-T651.* Technical report, Aerospace Specification Metals Inc.

[14] *Emissivity coefficients of some common materials.* `http://www.engineeringtoolbox.com`.

[15] *CES Edupack 2005.*

[16] *Aluminum 6061-T6; 6061-T651.* Technical report, Aerospace Specification Metals Inc.

[17] P. Martinelli. Budget de masse de oufti-1. Technical report, Université de Liège, 2010-2011.

[18] ASI. *Vega user's manual, issue 3, revision 0.*

[19] Minco. *SPI 00-0603 Use of Minco Acrylic Pressure-Sensitive Adhesives.*

[20] ESA Publications Division. *ECSS-E-10-03A : Space engineering - testing.* ESA, 2002.

[21] Kokam Co., Ltd. *Superior Lithium Polymer Battery SLB 603870H*, 2003.

[22] ESA Publications Division. *ECSS-E-ST-31C: Space engineering - Thermal control general requirements.* ESA, 2002.

[23] G. Ghiringhelli. Notes of the course "tecnica e sperimentazione aerospaziale".

[24] http://www.csl.ulg.ac.be.

[25] H. Chesser N. Navarathinam, R. Lee n. *Characterization of Lithium-Polymer batteries for CubeSat applications. Acta Astronautica*, 2011.

[26] Matweb. `www.matweb.com`.

[27] Wolframalpha. `http://www.wolframalpha.com`.

[28] M.A. Rosen I. Dinçer. *Thermal Energy Storage. Systems and application.* Wiley, 2001.

[29] R.W. Pryor. Modeling materials through a phase transition: Using comsol multiphysics and applying physics first principles techniques. In *COMSOL Conference*, 2007.

[30] Microsemi. *PNP Power Silicon Transistor. Technical Datasheet.*

[31] J. Aldeguer C. Drevon. *Conception de cartes pour équipements spatialisables. Techniques de l'Ingénieur.*

[32]

[33] CHOMERICS. *CHO-THERM 1678. Thermally Conductive Elastomer Insulators.*

[34] ITP Engines UK Ltd. *ESATAN-TMS Thermal Trainig Manual*, 2009.

[35] J.H. Lienhard V J.H. Lienhard IV. *A Heat Transfer Textbook.* Phlogiston Press, third edition, 2004.

[36] P. Rochus. Notes of the course "conception d'expériences spatiales".

[37] N. Francois. Dynamic analysis and launch qualification of oufti-1 nanosatellite. Master's thesis, Université de Liège, 2009-2010.

[38] PlastiService group. *Ertacetal H*.

[39] P. Thirion. Design and implementation of on-board electrical power supply of student nanosatellite oufti-1 of university of liège. Master's thesis, Université de Liège, 2008-2009.

[40] *CubeSat Design Specification*.

[41] M. Noca. *SwissCube status*. Technical report, École Polytechnique Fédérale de Lausanne, 2010.

[42] Thermal vacuum test report for aau-cubesat. Technical report, Aalborg University.

[43] Rick Doe Bryan Klofas, Karl van Dyk. Ctec: Cubesat thermal environment chamber. Technical report, SRI International, 2009.

[44] `http://cubesat.slu.edu/old_page/index.php?n=AE.Thermal`.

[45] G. Roethlisberger. *SwissCube Newsletter*. 2008.

[46] A. Scholz J. Gießelmann, M. Plischke. Compass-1 qualification review. Technical report, FH Aachen, 2006.